QUANTIFYING AND CONTROLING ELECTRON TRANSFER AT NANO-PARTICLE BASED SEMICONDUCTOR ELECTRODE/LIQUID INTERFACES FOR THE ADVANCEMENT OF DYE-SENSITIZED SOLAR CELLS

By

Jesse William Ondersma

A DISSERTATION

Submitted to
Michigan State University
in partial fulfillment of the requirements
for the degree of

DOCTOR OF PHILOSOPHY

Chemistry

2012

ABSTRACT

QUANTIFYING AND CONTROLING ELECTRON TRANSFER AT NANO-PARTICLE BASED SEMICONDUCTOR ELECTRODE/LIQUID INTERFACES FOR THE ADVANCEMENT OF DYE-SENSITIZED SOLAR CELLS

By

Jesse William Ondersma

Over the past two decades dye sensitized solar cells have evolved from fascinating science to a potentially viable source of renewable energy. This dissertation investigates barriers preventing dye-sensitized solar advancement: mainly interfacial electron-transfer reactions from nanoparticle TiO₂ films to redox shuttles (i.e. recombination). The focus is on the use of outersphere redox couples to perform systematic investigations of recombination reactions. A primary example is a system of cobalt(III/II) tris-bipyridyl complexes. The resulting detailed representation of electron transfer at the semiconductor/liquid interface in dye sensitized solar cells is presented. The result of these studies allowed for the development of a relatively simple model based in Marcus Theory to predict the efficiency of DSSCs as a function of redox couple potential and reorganization energy. Also presented is a novel variable temperature spectroelectrochemical method to measure the conduction band energy in mesoporous semiconductor electrodes that became necessary to develop during the course of this work. In addition, methods of controlling recombination and overcoming mass transport limitations which can lead to high-efficiency solar cells are discussed.

Copyright by JESSE WILLIAM ONDERSMA 2012

ACKNOWLEDGMENTS

There are many people to whom I owe thanks over my graduate career. Tom, you have been a fantastic mentor and an excellent example of a scientist. You have also been an advocate, giving me not only the opportunities but also the confidence to showcase my research that I would not otherwise have had. I greatly appreciate the freedom you have granted me in the lab, affording learning opportunities that only failure can provide and the resulting drive to hold myself and my work to a higher standard. There has never been a day that I have regretted working in your lab. Ben and Kelley, I can't imagine how dull the past four years would have been without you in the lab. Ben, though we may never agree whether we are in fact humans or dancers I appreciate you as a friend and colleague and will miss having you as a travel companion at conferences. Kelley not only have you kept the lab safe from danger but you have helped keep the lab light-hearted and for that I thank you. I sincerely wish both of you the best. Masha, Reena, and Suraj, as post-docs you have given me guidance and as friends you have brought joy to the lab and thus to my life. Yuling, it has been a pleasure having the chance to mentor you and work with you. I know you will go on to do great things in the Hamann lab. Brooke, I know I've asked a lot of you over the past few years and I appreciate the sacrifices you've made so that I could achieve my goals. I promise you that I will make them all worthwhile as we continue our life together. I could not have done this without you; I eagerly look forward to what is to come.

TABLE OF CONTENTS

LIST OF TA	BLES	vii
LIST OF FIG	URES	viii
Chapter 1	Motivation and Introduction	1
1.1	Motivation for Research of Alternative Energy	1
1.2	Historical Development of Dye Sensitized Solar Cells	
1.3	Modern DSSC Operation	
1.4	The I ₃ /I Electrolyte	
1.5	Use of OSRSs as Model Systems for Fundamental Studies	11
REFE	RENCES	13
Chapter 2	Considerations for Using Outer-Sphere Redox Couple in Dye-Sensitized So	
	Cells	
2.1.1	Introduction	
2.1.2	Experimental	
2.1.3	Results and Discussion.	
2.1.4	Conclusions of Blocking Layers to Passivate TCO Substrate	
2.2.1	Blocking Layers for Nanoparticle TiO ₂ Electrodes	
2.2.2	Experimental	
2.2.3	Results of Utilizing Alumina Blocking Layers.	
2.2.4	Conclusions to Utilizing Alumina Blocking Layers in DSSCs	
REFE	RENCES	54
Chapter 3	Recombination and Diffusion Length in Dye Sensitized Solar Cells with	
2.1	Sphere Redox Shuttles	
3.1	Introduction	
3.2	Experimental	
3.3	Results and Discussion.	
3.4 REFE	Conclusions	
Chapter 4	Modeling DSSC Performance to Predict a Route Towards Higher Efficienc	v 75
	RENCES	•
Chapter 5	Measurements and Modeling of Electron Transfer from Nanoparticle TiO ₂	
•	Electrodes to Outer-Sphere Redox Shuttles	83
5.1	Introduction	
5.2	Experimental	
5.3	Measurements	97
5 4	Modeling	91

	5.4.1	Electron Concentration.	91
	5.4.2	Recombination Rate.	96
	5.4.3	Reorganization Energy	100
	5.4.4	Calculated Lifetimes.	
5.5		Conclusions	
	RENCES		
Chapte	er 6	Conduction Band Energy Determination by Variable Temperature	
Chapter o	Spectroelectrochemistry	115	
	6.1	Introduction	
	6.2	Experimental Considerations for Spectroelectrochemistry	
	6.3	Variable Temperature Spectroelectrochemistry Results	
	6.4	Discussion.	
	6.5	Conclusion.	
	6.6	Experimental	
		RENCES	
Chapte	er 7	Diffusion Limitations in DSSCs Utilizing Outer-Sphere Redox Shuttles:	
Спари	<i>7</i> 1 /	Desirability of Methanol	13/
	7.1	Introduction to Diffusion Limitations in DSSCs Utilizing Outer-Sphere Re	
	7.1	Shuttles	
	7.2	DSSC Performance in Methanol.	
	7.2	Energetic and Kinetic Considerations for Methanol Based Dye Sensitized S	
	1.5	Cell	
	7.3.1	Effect of Methanol on TiO ₂ Energetics.	
	7.3.1	Effect of Methanol on TiO ₂ Energetics	
	7.3.2		
	7.3.3 7.4	Effect of Methanol on Dye Energetics	143
	7.4	Conclusions	
	7.6	Experimental Experimental	
	KEFE	RENCES	153
Chapte	er 8	Future Directions for DSSCs.	156
1	8.1	Ionic Liquids	
	8.2	Increased Voltage in DSSCs with Blocking Dyes and Highly Positive	
		Shuttles	158
	8.3	Alternative Semiconducting Materials.	
	8.4	Experimental	
	8.4.1	Ionic Liquids in DSSCs	
	8.4.2	High Voltage DSSCs.	
8	8.4.3	Spectroelectrochemistry of SrSnO ₃	
		RENCES	176

LIST OF TABLES

Table 5.1	Parameters used for full model of lifetimes given in equation 5.16	102
Table 6.1	Fit results of absorbance vs. temperature to equation 6.5	125

LIST OF FIGURES

Figure 1.1	Device schematic and b) Energy diagram of a DSSC showing relevant processes. For interpretation of the references to color in this and all other figures, the reader is referred to the electronic version of this dissertation
Figure 2.1	Dark J - V curve for a DSSC utilizing $[Ru(bpy)_2(MeIm)_2]^{3+/2+}$ as the redox shuttle.
Figure 2.2	Cyclic voltammograms of $[Ru(bpy)_2(MeIm)_2]^{3+/2+}$ using three different working electrodes: 1) blank FTO 2) nanoparticle TiO ₂ on FTO (black solid), 3) flat TiO ₂ (blue short dash), and 4) nanoparticle TiO ₂ film on flat TiO ₂ (red long dash). Also shown for reference is the capacitive CV of a nanoparticle electrode in contact with blocking electrolyte (green thin solid)
Figure 2.3	<i>J-E</i> curves for bare FTO (red) and FTO coated with films of either TiO ₂ (blue) or PPO (green)
Figure 2.4	a) <i>J-E</i> curves for three electrodes each containing a TiO ₂ nanoparticle film on 1) bare FTO (red), 2) FTO coated with a TiO ₂ blocking layer (blue) or 3) FTO coated with a PPO blocking layer (green). b) Cyclic voltammograms of TiO ₂ nanoparticle electrodes utilizing a TiO ₂ (blue, dashed) or PPO (green, solid) blocking layer.
Figure 2.5	Approximate energy diagram of FTO coated with a a) PPO or b) TiO_2 blocking layer in contact with a nanoparticle TiO_2 film showing Fermi-levels when the TiO_2 has high or low R_T
Figure 2.6	$log(J)$ vs. E plots of electrodes with blocking layers of TiO_2 both with nanoparticle films (dashed black) and without nanoparticle films (solid red) using a) $[Co(t-bu_2bpy)_3]^{3+/2+}$ and b) $[Ru(bpy)_2(MeIm)_2]^{3+/2+}$
Figure 2.7	a) Representative Nyquist plots displaying impedance data taken at three applied potentials. b) Equivalent circuit of DSSC used for fitting impedance data; the fit parameters are described in the text.
Figure 2.8	a) Overlay of J - V curve with diffusion resistance, R_d . b) Diffusion coefficient, D , of the electrolyte in the cell vs. cell voltage

Figure 2.9	Impedance spectra of a) sandwich DSSC and b-c) three-electrode DSSC at the potentials: -0.475 V (red diamonds), -0.500 V (blue circles), -0.525 V (green triangles), -0.550 V (cyan squares), and -0.575 V (yellow circles) vs. solution potential. The frequencies decrease from left to right as indicated in (a)43
Figure 2.10	(a) Nyquist plots of three-electrode DSSCs both with (filled blue symbols) and without (hollow red symbols) alumina at -0.70 V vs. Ag $^{+/0}$. Plots of (b) capacitance, C_{μ} , and (c) charge transport, R_T (circles), and transfer, R_{CT} (triangles), resistances extracted from EIS measurements for DSSCs with an alumina coating (filled blue symbols) and without alumina (hollow red symbols). (d) Lifetimes, τ_n , measured by EIS (triangles) and OCVD (lines) and transport times, τ_d , measured by EIS (diamonds) for DSSCs both with (blue) and without (red) an alumina coating. Cells used an identical electrolyte based on [Co(t -Bu ₂ bpy) ₃] as described in text
Figure 2.11.	a) Dark current density, b) natural log of the dark current density, and c) $\ln(R_{CT}^{-1})$ for electrodes with 0-4 layers of alumina coating 1000 ALD cycles of TiO ₂ on FTO. The β values provided by the slope of the lines in c) are 0.69 Å at 0.05 V, 0.74 Å at 0.10 V and 0.83 Å at 0.15 V vs. Ag/AgCl
Figure 3.1	a) Nyquist plots at -0.75 V vs. $\operatorname{Ag}^{+/0}$, b) capacitance, C_{μ} , c) charge transfer resistance, R_{CT} , (filled symbols) and transport resistance, R_{T} , (hollow symbols) d) electron lifetimes, τ_{n} , (filled symbols) and diffusion coefficient, d_{n} , (hollow symbols) of a single photoanode in contact with three separate redox shuttles: $[\operatorname{Co}(t-\operatorname{Bu}_{2}\operatorname{bpy})_{3}]^{3+/2+}$ (blue diamond), $[\operatorname{Co}(\operatorname{Me}_{2}\operatorname{bpy})_{3}]^{3+/2+}$ (Red circle), and $[\operatorname{Co}(\operatorname{bpy})_{3}]^{3+/2+}$ (green triangle).
Figure 3.2	a) Plots of calculated diffusion lengths, L_n , of a single photoanode in contact with three separate redox shuttles: $[\text{Co}(t\text{-Bu}_2\text{bpy})_3]^{3+/2+}$ (blue diamond), $[\text{Co}(\text{Me}_2\text{bpy})_3]^{3+/2+}$ (Red circle), and $[\text{Co}(\text{bpy})_3]^{3+/2+}$ (green triangle). b) Current density vs. applied potential plots from DSSCs in contact with $[\text{Co}(t\text{-Bu}_2\text{bpy})_3]^{3+/2+}$ (blue solid), $[\text{Co}(\text{Me}_2\text{bpy})_3]^{3+/2+}$ (Red long dash), and $[\text{Co}(\text{bpy})_3]^{3+/2+}$ (green short dash) in response to 10 mW cm ⁻² illumination69
Figure 4.1	Calculated η as a function of E_{redox} and λ of the mediator in recombination limited DSSCs

Figure 5.1	a) Current density vs. applied potential curves and b) lifetimes vs. potential plots for DSSCs utilizing [Co(Me ₂ bpy) ₃] (blue, dash line/diamonds) and [Ru(bpy) ₂ (MeIm) ₂] (red, solid line/circles) redox shuttles
Figure 5.2	a) Cyclic voltammogram and b) plot of $\ln(C_{\mu})$ vs potential for a TiO ₂ electrode in a blocking electrolyte composed of 0.1 M LiClO ₄ in acetonitrile. c) The difference between the measured total capacitance and the fitted exponential capacitance (circles). Also shown is the result of fitting the capacitance difference to a Gaussian (red line).
Figure 5.3	Energy diagram displaying the distribution of localized states and recombination from the conduction band (green solid), from an exponential distribution of surface states (blue dot-dash), and from a mono-energetic distribution of states (red dash). $qE_{f,0}$ is the quasi-Fermi level in the dark equilibrated with the redox potential of the redox shuttle, E_{redox} , \mathbf{E}_{cb} is the conduction band energy and \mathbf{E}_{F} is the Fermi energy
Figure 5.4	Experimental and modeled lifetimes for both a) $[Ru(bpy)_2(MeIm)_2]^{3+/2+}$ experimental (circles), full model (red line), model without $U_{s,me}$ (green, dot-dot-dash), model without $U_{s,exp}$ (blue, dash), and b) $[Co(Me_2bpy)_3]^{3+/2+}$ experimental (diamonds), full model (red line), without surface state recombination (blue, dash), and without conduction band recombination (green line, dot-dot-dash)
Figure 5.5	Experimental and modeled lifetimes demonstrating coupling length dependence on recombination for both a) $[Ru(bpy)_2(MeIm)_2]^{3+/2+}$ and by $[Co(Me_2bpy)_3]^{3+/2+}$ experimental (hollow symbols), full model with 1 nm coupling length (red line, solid), and full model with 0.3 nm coupling length without surface state recombination (blue line, dashed)
Figure 6.1	Change in absorbance from -0.70, -0.80, -0.90, -1.00, -1.10, and -1.15 V vs Ag/AgCl to 0.5 V vs. Ag/AgCl. Potentials move from more negative to more positive from top to bottom in the figure as indicated
Figure 6.2	Monitoring %T at 800 nm of a nanoparticle based TiO ₂ electrode while performing 25 cycles of cyclic voltammetry a) from 0.5 to −2 V vs. Ag/AgCl at 0.05 V/s and b) from 0.5 to −1 V vs. Ag/AgCl at 0.1 V/s
Figure 6.3	Absorbance at 950 nm for a nanoparticle TiO ₂ film during cyclic voltammetry with several scan rates from 20 mV/s to 1.25 mV/s121

Figure 6.4	Change in absorbance of a TiO ₂ electrode when potential is stepped from +0.5 to -0.8 V vs. Ag/AgCl
Figure 6.5	Plot of %T at 950 nm while stepping the potential from 0.50 to -0.45, -0.50 -0.55, -0.60, -0.65, -0.70, and back to +0.50 V vs. Ag/AgCl. Each trace represents a different temperature: 15.0, 21.1, 27.5, 34.5, 40.9, 47.3 and 53.8°C with increasing temperatures resulting in decreasing %T
Figure 6.6	Plot of ln(A) vs. T ⁻¹ each line represents a different potential from -0.70 to -0.45 V vs. Ag/AgCl in 50 mV increments from top to bottom. The temperatures correspond to 288, 294, 301, 308, 314, 320 and 327 K. Error bars represent one standard deviation. The solid lines depict a global fit result to equation 6.5 as described in the text
Figure 7.1	Experimental results for an N3 sensitized TiO ₂ nanoparticle based DSSC utilizing $[\text{Co}(t\text{-Bu}_2\text{bpy})_3]^{3+/2+}$ as a redox shuttle. a) EIS spectrum taken at -0.425 V vs $E(R^+/R)$ showing each resistive element. b) Extracted R_d values taken between P_{max} and V_{oc} . c) Experimental (blue solid) $J\text{-V}$ curve and a $J\text{-V}_{corr}$ curve correcting for R_d and R_{Pt} (135 Ω total correction, black dashed line), with the resulting improvement in ff indicated.
Figure 7.2	Current density vs. potential curves for an acetonitrile based (blue) and a methanol based (red) DSSCs, both using the same dye and redox shuttle as described in text
Figure 7.3	a) Comparison of chemical capacitance, C_{μ} , and b) transport resistance, R_T , in acetonitrile (blue) and methanol (red) based DSSCs. Open symbols represent individual cell data while solid symbols represent averages
Figure 7.4	Comparison of charge transfer resistance, R_{CT} , a) vs. potential and b) vs. C_{μ} in acetonitrile (blue) and methanol (red) based DSSCs. Open symbols represent individual data while solid symbols represent averages
Figure 7.5	Normalized absorbance (solid) and emission (dashed) spectra of Z907 in acetonitrile (blue) and methanol (red)
Figure 7.6	Energy diagram showing changes in energetics in a dye-sensitized solar cell where the solvent is changed from acetonitrile to methanol
Figure 7.7	Mass transport limiting current density, J_{lim} , in methanol by varying concentration of $[Co(t-Bu_2bpy)_3]^{3+}$ and light intensity. Light intensities used

	were 0.1, 0.25, 0.5, 0.75, 1.0, 2.0, 5.0, 10 suns, with 1 sun representing 100
	were 0.1, 0.25, 0.5, 0.75, 1.0, 2.0, 5.0, 10 suns, with 1 sun representing 100 mWcm ⁻² illumination with the AM1.5G spectrum
Figure 8.1	a) IPCE and b) current transient of a DSSC utilizing [Co(bpy) ₃] ^{3+/2+} as part of an ionic liquid system
Figure 8.2	J-V curve of DSSC using the redox shuttle $[Ru(bpy)_2(MeIm)_2]^{2+/3+}$ is conjunction with the dye $Ru(bpy)_2(dcbpy)$
Figure 8.3	a) ΔA of SrSnO ₃ between the potential indicated and 0.5 V vs. Ag/AgCl. b Absorbance of FTO determined by subtracting the absorbance of the electrochemical cell and acetonitrile

Chapter 1: Motivation and Introduction

1.1 Motivation for Research of Alternative Energy

The twenty-first century has begun with a mandate for the scientific community to develop economical renewable energy technologies. (1-4) The accumulation of climate research gathered during the final decades of the twentieth century indicated that most of the 0.6 °C increase in average global temperature during that time resulted from increases in anthropogenic greenhouse gas concentrations, mainly carbon dioxide.(5) Indeed, levels of CO2 and average atmospheric temperatures have shown a strong correlation in data going back over 400,000 years.(5) This alteration of Earth's atmosphere results from the enormous scale of the current burn rate of carbon based fossil fuels to satisfy the world's societies' growing energy demand. During 2010 approximately 30 gigatonnes of CO₂ were released into the atmosphere through the burning of oil, coal, and natural gas, representing an increase in atmospheric CO2 of approximately 0.5%.(6) The cumulative releases of anthropogenic CO₂ resulting from global industrialization over the past 150 years has resulted in a greater than 40% increase in atmospheric concentrations from 280 ppm to 397 ppm, the peak level for 2012.(7) The demand for energy is projected to double by 2050 as the population increases and societies industrialize and increase their standard of living.(8) Renewable energy, that which results in no net greenhouse gas emissions, must be utilized if further impact to the global environment is to be avoided. The primary sources for carbon neutral energy are hydroelectric, geothermal, tidal, wind, biomass, nuclear, and solar. Of these energy sources only one is scalable to fully meet the predicted needs of our planet: solar.(1) The sun irradiates Earth with 120,000 terawatts, TW, of power, approximately 7,400 times the 16.2 TW global energy consumption in 2009.(6) The

estimated power that could feasibly be collected using 10% efficient photovoltaic cells, assuming they become a widely adopted technology and cover 0.16% of land is 20 TW, which is more than enough to satisfy total current demand.(9)

The widespread adaptation of solar energy is primarily prohibited by cost. Current commercial photovoltaics made from silicon that are 10-20% efficient produce electricity for approximately \$0.25-\$0.65 per kWhr, several times higher than electricity from fossil fuel sources.(10) The cost is unlikely to be lowered significantly by further increases in device performance, as they have already been optimized over the previous decades, or by decreasing construction costs, due to remarkably high energy requirements to produce 99.9999% pure Si required for crystalline photovoltaic cells.(11, 12) The path for economically competitive photovoltaics must them come from an alternative strategy to single crystalline semiconductors, which consist of earth-abundant materials that can be produced by simple processing methods. One such strategy using inexpensive material is represented by dye-sensitized solar cells, DSSCs.(13)

In traditional semiconductor based photovoltaic devices, a single material must absorb incident light, separate the resulting exciton, and transport the charge carriers to their respective contacts to be collected. In dye-sensitized solar cells, these processes are separated. Absorption of light is achieved by a molecular dye covalently attached to a semiconductor surface. The exciton is split by electron injection into the semiconductor conduction band. DSSCs utilize transparent wide band gap semiconductors where the band gap energy, \mathbf{E}_g , is sufficiently large to prevent direct excitation by visible light ($\mathbf{E}_g > 3$ eV). This represents a significant advantage for DSSCs since there are essentially no holes to recombine with electrons in the electron transporting material. Thus, virtually no recombination mechanism which hampers traditional

photovoltaics are possible in DSSCs, allowing for the use of inexpensive, lower quality materials without loss in efficiency. Anatase TiO₂ nanoparticles have been the semiconductor material of choice as the electron transport medium. Typical TiO₂ anodes used in DSSCs are mesoporous, resulting in a surface area increased over 1000 fold compared to the geometric area. Hole transport to the counter electrode is performed by a molecular redox shuttle in an electrolyte solution which fills the pores in the anode and spans the gap to the cathode. Separation of the light absorption, electron transport, and hole transport processes allows for a modular approach to independently characterize and optimize each component independently.

1.2 Historical Development of Dye Sensitized Solar Cells

The field of dye-sensitized solar cells grew out of silver halide chemistry that was pursued for the photography industry well over a century ago. The first report of spectral sensitization of a semiconductor to sub-band gap irradiation was made by James Moser in 1887 while working with silver halides coated in erythrosine.(14) The mechanism of such dye-sensitization of a semiconductor crystal was later proposed to involve electron transfer from a dye excited state into the semiconductor conduction band in 1938 by Gurney and Mott.(15) This electron transfer mechanism, and the competing energy transfer mechanism, would remain under debate for the next three decades. This debate was ultimately settled by Gerischer and Tributsch's work in 1968 when they used electrochemical methods to measure current produced under illumination while previous reports measured an increase in conductance.(16, 17)

Most of the work in the sensitization field in the early 20th century was focused on the sensitization of low band gap semiconductors to extend their visible absorption through the red wavelengths for the photography industry. The first account of sensitization of a wide band-gap semiconductor, one which cannot absorb visible light, came in 1949 when Putzeiko and Trenin

reported photoconductivity of pressed ZnO powder with a variety of organic dyes such as rhodamine B and eosin when exposed to visible light.(18) In 1968 Gerischer *et al.* reported the current voltage characteristics of one of the earliest versions of a DSSC (although this term would not be coined for many years) where an electrochemical cell was constructed with single crystal ZnO in contact with a solution containing an organic dye: fluorescein, rose bengale, or pseudoisocyanine chloride.(16) Gerischer and Tributsch later found that the sensitized photocurrent could be increased upon addition of a reducing agent such as hydroquinone, terming this phenomena "supersensitization."(17)

In these early photoelectrochemical cells, incident light was absorbed by free dye in solution; the majority of the photoexcited dyes decayed back to ground state prior to injecting into the semiconductor. To overcome this energy loss mechanism, in 1976 Osa *et al.* covalently bound rhodamine B to both TiO₂ and SnO₂ semiconductor surfaces using a silyl ether linkage to produce a monolayer of dye.(19) Using hydroquinone in the contacting electrolyte Osa *et al.* were able to obtain photocurrent of the same magnitude as cells with dye dissolved in solution, but using a much lower total concentration of dye.(19) Thus, the quantum yield of charge injection was greatly enhanced.

An important step towards the development in DSSCs was the use of transition metal complexes as sensitizers; indeed all of the record efficiency DSSCs created between 1991 and 2011 used ruthenium bipyridyl based complexes. The first ruthenium (II) bipyridyl complexes used to sensitize wide band gap electrodes was $[Ru(bpy)_3]^{2+}$, where bpy is 2,2'-bipyridine, due to it being the transition metal complex with the most widely reported photo-excited electron transfer properties. In 1975 Gleria and Memming used $[Ru(bpy)_3]^{2+}$ in solution to sensitize SnO₂ in order to study the excited-state electron transfer process, in which they observed

wavelength dependent anodic photocurrent matching the absorbance spectrum of $[Ru(bpy)_3]^{2+}$.(20) In 1980, with a goal of photo-electrolysis of water, Goodenough *et al.* used carboxylic acid groups to covalently bind $Ru(bpy)_2(dcbpy)$, where dcbpy is 2,2'-bipyridine-4,4'-dicarboxylic acid, to the surface of TiO_2 , $SrTiO_3$, and SnO_2 .(20, 21) These cells achieved internal quantum yields (absorbed photon to current efficiency, APCE) of only 0.25%, and the energy conversion efficiency was orders of magnitude smaller yet. The primary causes of the low efficiency were the slow reduction of the oxidized dye by water and insufficient light absorption.

In fact, low light absorption plagued all dye-sensitized devices created for energy conversion until 1985 since they contained only a mono-layer of dye on a nominally flat electrode surface. In order to increase light absorption of the film the light absorption path length needed to be increased. In 1985 Gratzel et al. accomplished this by using a rough polycrystalline TiO2 electrode with roughness factor (the real surface area divided by the geometric area) of 100 to produce an exciting 44% incident photon to current efficiency, IPCE, under monochromatic light.(22) This report was followed in 1988 by Gratzel et al. who employed an electrode that had an increased roughness factor of 200, combined with the sensitizer Ru(dcbpy)3, and an aqueous I3 /I regenerative electrolyte, to achieve a monochromatic IPCE surpassing 70%.(23) The overall energy conversion efficiencies of the DSSCs produced to this point were still only ~1%. This is partially attributed to the large HOMO-LUMO gap of the sensitizer Ru(dcbpy)3 which results in an absorbance maximum near 460 nm; higher photocurrents and efficiencies would require significantly red-shifting the absorbance spectrum of the sensitizer. To facilitate broader light absorption, Scandola et al. introduced a trinuclear Ru complex which pushed the light absorbance past 600 nm.(24) Gratzel et al. later used this dye in 1991 in the seminal report in Nature where, using a nanoparticle TiO₂ based electrode providing a surface area enhancement of approximately 2000, energy conversion efficiencies surpassing 7% under AM1.5 illumination were achieved.(13)

The breakthrough of utilizing high surface area nanoparticle semiconductor electrodes established the viability of the field and since 1991 all of the record high efficiency DSSCs have employed mesoporous TiO₂ nanoparticle electrodes. Also, between 1991 and 2011 all efficiency improvements were gained primarily through dye design. Gratzel et al. quickly followed their seminal report with the development of the sensitizer Ru(dcbpy)₂(NCS)₂, now commonly known as N3, reported in 1993.(25) By combining N3 with the porous TiO₂ electrode optimized with a 4-tert-butylpyridine treatment and an acetonitrile based LiI/I2 electrolyte, the first DSSC to surpass 10% efficiency was produced.(25) A modest improvement in efficiency was gained through the double deprotonation of N3, forming the dye known as N719, which surpassed 11% efficiency in an optimized cell. (26, 27) The search for panchromic sensitizers followed seeking to push absorption farther to the red and near-IR resulting in the development of the high performance "black dye" Ru(tcterpy)(NCS)₃, where tcterpy is 4,4',4"-tricarboxy-2,2':6',2"terpyridine.(28) This black dye absorbs wavelengths past 900 nm producing currents greater than 20 mAcm⁻² and efficiencies surpassing 11%.(28-30) Gratzel's reports in 1991 and 1993 lead to what has been the state of the art DSSC for the following two decades: a mesoporous TiO₂ electrode, a ruthenium-based sensitizer, and the I₃/I redox shuttle in a nonaqueous solvent. The operational details of such DSSCs are described below.

1.3 Modern DSSC Operation

A schematic of a typical modern DSSC construction is depicted in figure 1.1a along with a potential diagram showing the major electron pathways demonstrated in figure 1.1b. The

process begins with photoexcitation of the sensitizing dye, 1, which then injects the excited electron into the conduction band of the semiconductor, 2, a process termed injection. The electron is transported via diffusion through the mesoporous nanoparticle film to be collected by a transparent conductive oxide, TCO, contact electrode. The oxidized dye molecule is reduced by the redox shuttle in the electrolyte, 3, a process commonly referred to as regeneration. The circuit is completed when the oxidized form of the mediator diffuses to the counter electrode, CE, and is reduced, 4. Additionally, there are detrimental electron transfer pathways which are depicted in figure 1.1(b) by red arrows. The excited state dye can decay back to its ground state, either radiatively or nonradiatively, without injecting an electron -1. Once the electron has been injected into the TiO_2 it can recombine with either the oxidized dye, 5, or the oxidized form of the mediator, 6. Pathway 6 will hereby be referred to as recombination.

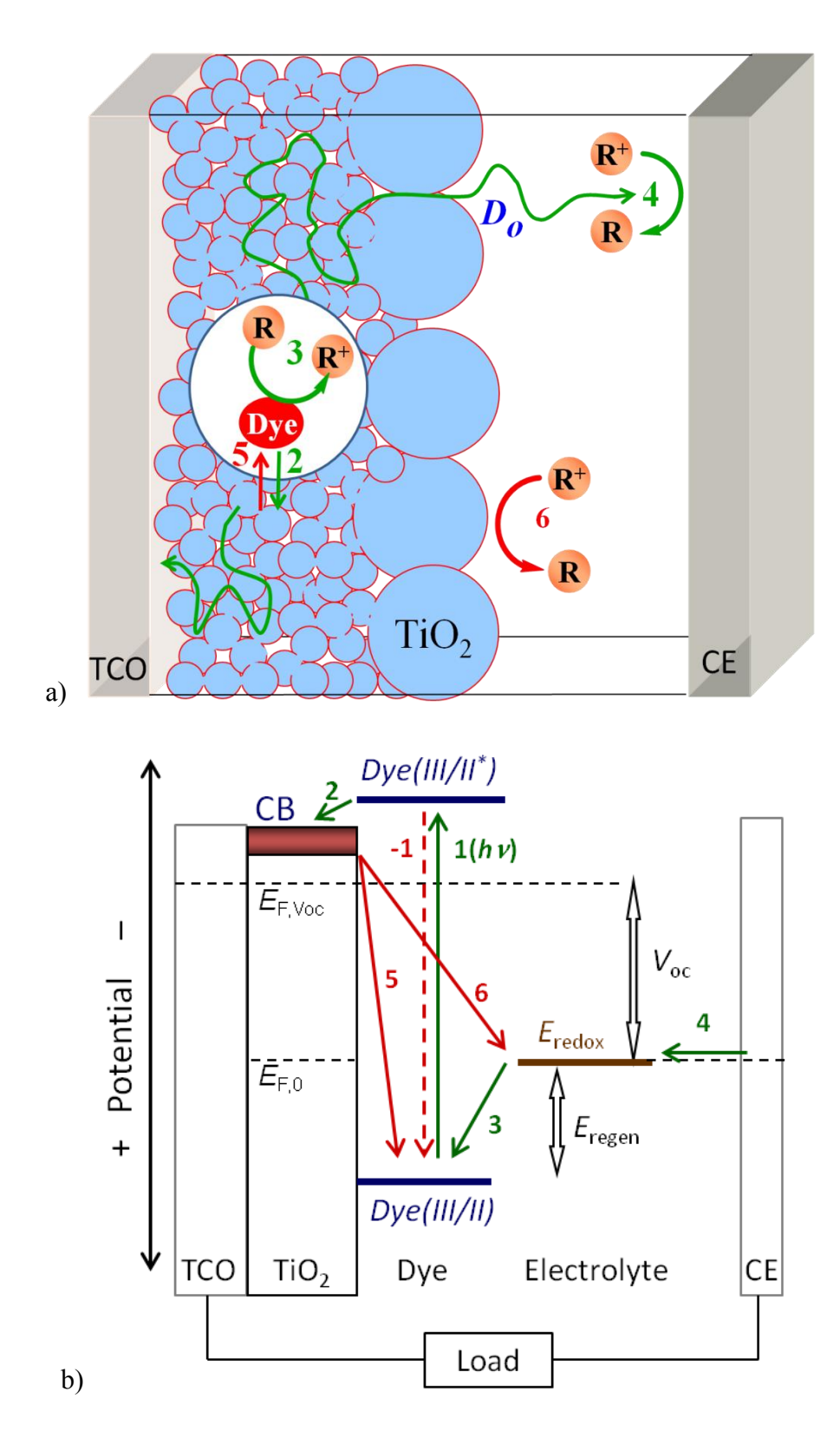


Figure 1.1. Device schematic and b) Energy diagram of a DSSC showing relevant processes. For interpretation of the references to color in this and all other figures, the reader is referred to the electronic version of this dissertation.

1.4 The I₃/I Electrolyte

The tri-iodide/iodide electrolyte has enjoyed over two decades as the electrolyte of choice for DSSC research. I_3^-/I^- possesses several remarkable characteristics which have resulted in this reliance. First, dyes such as N3 and N719 are regenerated with near unity efficiency by $I^ I_3$. Second, back electron transfer from I_3 is remarkably slow, largely due to a complicated multi-electron transfer mechanism. I_3 is remarkably slow back electron transfer (recombination) results in long electron diffusion lengths, I_3 , through the I_3 allowing for near unity charge collection efficiencies. I_3 Third, I_3 is highly soluble in an array of solvents and has a high diffusion coefficient due to its small size allowing for optimized concentrations of each species without concern for reaching the solubility limits or diffusion limits. Fourth, I_3 is a relatively low light absorbance reducing competitive absorbance with the dye. In addition, the I_3 is remarkably slow, largely due to a composition under operation conditions.

Despite all of the favorable characteristics of I_3^-/I^- , strict reliance on the I_3^-/I^- electrolyte is largely responsible for the limited increase in DSSC efficiency observed over the past 20 years of research. The most notable deleterious effect of using the I_3^-/I^- redox shuttle is a limited cell voltage. For the I_3^-/I^- redox couple redox shuttle the $E_{redox} \approx 0.05$ V vs. Ag/AgCl,(32, 35-37) The ground state potential, E° , of most dyes identified to work well with I_3^-/I^- however, lie much more positive, for example for N3, $E^\circ = 0.85$ V vs. Ag/AgCl.(35, 38) The large required driving force for regeneration (E_{regen} in figure 1.1b) with I_3^-/I^- directly limits the attainable V_{oc} with a TiO₂ photoanode to ≈ 0.8 V.

The large driving force required for regeneration with iodide results from a complicated electron transfer mechanism, and the ~430 mV potential loss due to the difference of the

reduction potential between I_3^-/I^- , which governs the counter electrode potential and I_2^-/I^- , which limits the dye's E° . (39) The iodide regeneration mechanism has been shown to proceed though intermediates containing an oxidized dye/iodide complex and the formation of the $I_2^$ radical.(31, 32, 40) The formation of a dye iodide complex during the initial step in regeneration limits I to only efficiently regenerating selectively few dyes since it requires a group to bind to for efficient regeneration, most notably NCS for inorganic dyes, resulting in the dominance of N3, N719, and black dye.(31) Iodide has also been found to regenerate a number of organic dyes efficiently, however the mechanism is still not first order in [I] indicating the formation of intermediate dye/iodide complexes.(41) This complicated electron transfer mechanism which prevents fast recombination also prevents systematic studies of recombination and dye regeneration; thus preventing detailed understanding of the electron transfer mechanisms in DSSCs.(34, 42) Over the past two decades thousands of dyes with desirable properties when compared to N3, (e.g. increased light absorption, increased stability, decreased cost, ease of synthesis) have been produced and tested with an I₃-/I- electrolyte in labs across the world and were determined to work worse than N3.(43, 44) The resulting inefficiency of DSSCs based on these dyes is not necessarily inherent but rather from the fact that some novel dyes bind I₃, increasing recombination and quenching the dye excited state. (45, 46) The unpredictability of the I₃/I redox shuttle renders it a poor choice when evaluating novel dyes for DSSCs.

1.5 Use of OSRSs as Model Systems for Fundamental Studies

Utilization of outer-sphere redox shuttle can overcome the possibility of the redox shuttle binding to the dye. Furthermore, using single electron outer-sphere redox shuttles offers simplified measurements, predictable electron transfer properties and extrapolation of the results to further predict desirable redox shuttle properties for DSSC design. The first example of this

strategy was reported by Gregg *et al.* who employed ferrocene as a model redox shuttle to examine recombination pathways in DSSCs.(47) Gregg used ferrocene to monitor the recombination processes between the transparent conductive oxide, TCO, substrate and the oxidized redox shuttle as well as the recombination between excited electrons in the TiO_2 and the oxidized shuttle. Their results demonstrated that replacing the kinetically slow redox couple I_3^-/I^- redox shuttle with the fast ferrocene/ferrocenium shuttle in DSSCs the photovoltaic effect nearly disappears due to dramatically increased recombination rates.(47) They also demonstrated that careful surface treatments, specifically the deposition of siloxane on the TiO_2 surface, could alleviate the restrictions of fast recombination and significantly enhance the efficiency. While never intended to be a practical choice for a redox shuttle, use of ferrocene did improve our understanding of the operation of DSSCs and allowed testing new strategies for future gains in efficiency.

This dissertation discusses in detail the main challenges facing the use of outer-sphere redox shuttles in DSSCs: recombination and mass transport limitations. Chapter 2 details the most important consideration when using outer-sphere redox shuttles in DSSCs, separated into two sections each focusing on prevention of recombination from 1) the conductive substrate and 2) the nanoparticle TiO₂. Chapter 3 investigates the fundamental processes responsible for widely varying DSSC device performance when redox shuttles which vary only slightly are used. Considering the results provided in chapter 3, a model is developed in chapter 4 to predict the performance of DSSCs based on key characteristics of the redox shuttles: the redox potential and the reorganization energy. Chapter 4 predicts much higher DSSC efficiencies may be obtainable using outer-sphere redox shuttles which have Marcus inverted electron transfer kinetics from the conduction band of TiO₂. Chapter 5 examines if such Marcus inverted kinetics are observable

using mesoporous TiO₂ electrodes and develops a detailed description of electron transfer at the semiconductor/liquid interface. This electron transfer model requires accurate determination of the energetic location of the semiconductor conduction band edge, something that has eluded scientists in the field using porous, nano-particle based semiconductor electrodes. Chapter 6 introduces a novel technique to measure the band edge in such electrodes using a variable temperature spectroelectrochemistry technique. The other main limitation for the use of outersphere redox shuttles in DSSCs is mass transport limitations brought on by low diffusion coefficients and limited solubility in acetonitrile, the most common solvent by far in DSSCs. One way to overcome mass transport limitations is then to use a solvent in which the shuttles are much more soluble in, such as methanol. Chapter 7 focuses on the energetic and resulting kinetic changes which occur in a DSSC when the solvent is changed. These changes must be understood before an efficient DSSC can be designed for use in methanol. Chapter 8 outlines an outlook for the future directions of the field of dye-sensitized solar cells

REFERENCES

REFERENCES

- 1. N. S. Lewis, MRS Bulletin **32**, 808 (Oct, 2007).
- 2. R. E. Smalley, MRS Bulletin 30, 412 (2005).
- 3. D. J. Eaglesham, MRS Bulletin **30**, 923 (2005).
- 4. "Renewable Energy Sources and Climate Change Mitigation" (Intergovernmental Panel on Climate Change, 2012).
- 5. R. K. a. R. Pachauri, A., "IPCC 2007: Climate Change 2007: Synthesis Report. Contribution of Working Groups I, II, and III to the Fourth Assessment Report to the Intergovernmental Panel on Climate Change" (Geneva, Switzerland, 2008).
- 6. IEA, Key World Energy Statistics. (International Energy Agency, Paris, 2011).
- 7. P. Tans, R. Keeling. (NOAA/ESRL (www.esrl.noaa.gov/gmd/ccgg/trents) Scripps Institution of Oceanography (scrippsco2.ucsd.edu/), 2012).
- 8. "Basic Research Needs for Solar Energy Utilization" (U.S. Department of Energy, 2005).
- 9. "Basic Energy Sciences Workshop Technical Reports" (DOE, 2005).
- 10. A. Slaoui, R. T. Collins, *MRS Bulletin* **32**, (2007).
- 11. M. Tao, *The Electrochemical Society Interface*, 30 (2008).
- 12. D. Sarti, R. Einhaus, Solar Energy Mater. Solar Cells 72, 27 (2002).
- 13. B. O'Regan, M. Gratzel, *Nature* **353**, 737 (Oct, 1991).
- 14. J. Moser, *Monatsh. Chem.* **8**, 373 (1887).
- 15. R. W. Gurney, N. F. Mott, *Proc. Roy. Soc. London* **A164**, 151 (1938).
- 16. H. Gerischer, M. E. Michel-Beyerle, F. Rebentrost, H. Tributsch, *Electrochim. Acta* 13, 1509 (1968).
- 17. H. Gerischer, H. Tributsch, Ber. Bunsenges. Phys. Chem. 72, 437 (1968).
- 18. E. K. Putseiko, A. N. Terenin, *Zhur. Fiz. Khim.* **23**, 676 (1949).

- 19. T. Osa, M. Fujihira, *Nature* **264**, 349 (1976).
- 20. M. Gleria, R. Memming, Z. Phys. Chem. 98, 303 (1975).
- 21. M. P. Dare-Edwards, J. B. Goodenough, A. Hamnett, K. R. Seddon, R. D. Wright, *Faraday Discussions* **70**, 285 (1980).
- 22. J. Desilvestro, M. Gratzel, L. Kavan, J. Moser, J. Augustynski, *J. Am. Chem. Soc.* **107**, 2988 (1985).
- 23. N. Vlachopoulos, P. Liska, J. Augustynski, M. Gratzel, *J. Am. Chem. Soc.* **110**, 1216 (1988).
- 24. R. Amadelli, R. Aragazzi, C. A. Bignozzi, F. Scandola, *J. Am. Chem. Soc.* **112**, 7099 (1990).
- 25. M. K. Nazeeruddin et al., J. Am. Chem. Soc. 115, 6382 (Jul 14, 1993).
- 26. M. K. Nazeeruddin et al., Inorg. Chem. 38, 6298 (Dec, 1999).
- 27. M. K. Nazeeruddin et al., J. Am. Chem. Soc. 127, 16835 (2005).
- 28. M. K. Nazeeruddin, P. Pechy, M. Gratzel, *Chem Com*, 1705 (1997).
- 29. M. K. Nazeeruddin et al., J. Am. Chem. Soc. 123, 1613 (2001).
- 30. Y. Chiba et al., Jpn. J. Appl. Phys. Part 2 Lett. Express Lett. 45, L638 (Jul, 2006).
- 31. J. N. Clifford, E. Palomares, M. K. Nazeeruddin, M. Gratzel, J. R. Durrant, *J. Phys. Chem. C* **111**, 6561 (May, 2007).
- 32. G. Boschloo, A. Hagfeldt, Acc. Chem. Res. 42, 1819 (2009).
- 33. J. Rowley, G. J. Meyer, J. Phys. Chem. C 113, 18444 (Oct, 2009).
- 34. L. M. Peter, J. Phys. Chem. C 111, 6601 (May, 2007).
- 35. B. A. Kamino, T. P. Bender, R. A. Klenkler, J. Phys. Chem. Lett. 3, 1002 (2012).
- 36. J. Datta, A. Bhattacharya, K. K. Kundu, *Bull. Chem. Soc. Jpn.* **61**, 1735 (1988).
- 37. A. Hagfeldt, G. Boschloo, L. C. Sun, L. Kloo, H. Pettersson, *Chem. Rev.* **110**, 6595 (Nov, 2010).
- 38. G. Sauve et al., J. Phys. Chem. B **104**, 6821 (Jul 27, 2000).

- 39. G. Boschloo, E. A. Gibson, A. Hagfeldt, J. Phys. Chem. Lett. 2, 3016 (2011).
- 40. A. Y. Anderson, P. R. F. Barnes, J. R. Durrant, B. C. O'Regan, *J. Phys. Chem. C* **114**, 1953 (Feb, 2010).
- 41. S. Martiniani, A. Y. Anderson, C. Law, B. C. O'Regan, C. Barolo, *Chem. Comm.* **48**, 2406 (2012).
- 42. Y. A. Yaraliev, *Uspekhi Khimii* **51**, 990 (1982).
- 43. M. Alebbi, C. A. Bignozzi, T. A. Heimer, G. M. Hasselmann, G. J. Meyer, *J. Phys. Chem. B* **102**, 7577 (Sep, 1998).
- 44. D. Kuciauskas, M. S. Freund, H. B. Gray, J. R. Winkler, N. S. Lewis, *J. Phys. Chem. B* **105**, 392 (Jan, 2001).
- 45. B. C. O'Regan et al., J. Am. Chem. Soc. 130, 2906 (Mar, 2008).
- 46. K. E. Splan, A. M. Massari, J. T. Hupp, *J. Phys. Chem. B* **108**, 4111 (Apr, 2004).
- 47. B. A. Gregg, F. Pichot, S. Ferrere, C. L. Fields, *J. Phys. Chem. B* **105**, 1422 (Feb, 2001).

Chapter 2: Considerations for Using Outer-Sphere Redox Couple in Dye-Sensitized Solar Cells

2.1.1 Introduction

In the time since O'Regan and Grätzel published their seminal paper on dye-sensitized solar cells, DSSCs, based on nanocrystalline TiO_2 , there has been a lot of interest in device characterization and improvement.(I-3) A key feature of these devices is the ability to transport photoinjected electrons through the nanoparticle semiconductor film to the transparent conductive metal-oxide substrate, TCO, with minimal losses. Electrons may be lost by transfer to the oxidized form of redox shuttle which permeates the mesoporous photoanode, however, for the I_3 -/ Γ redox shuttle this reaction is particularly slow.(2, 4) A similar additional form of back electron transfer may occur from the TCO to the redox shuttle.(5-8) Although this electron transfer may be negligible when using I_3 -/ Γ under certain conditions (short circuit or high light intensities), Cameron and Peter have shown it to be an important consideration under other conditions (open-circuit or low light intensities).(9) The complicated mechanism of the multielectron inner-sphere I_3 -/ Γ redox shuttle complicates detailed kinetic understanding of the operational parameters of the DSSC.(I0)

The I_3^-/I^- redox shuttle has been shown to limit DSSC performance by requiring an overpotential of > 500 mV to efficiently regenerate most sensitizers.(11) One proposed way to increase the voltage, and thus efficiency, of DSSCs is to reduce this overpotential through the use of redox shuttles with more positive potentials.(12) A few redox shuttles with potentials more positive than I_3^-/I^- ($E(I_3^-/I^-) = 0.23$ V vs. SCE)(11) have been utilized in DSSCs with some success. One such shuttle, a close analogue of I_3^-/I^- , is Br_3^-/Br^- with a redox potential of

0.86 vs. SCE. DSSCs utilizing Br₃⁻/Br⁻ have achieved open circuit potentials of over 1 V but Br₃⁻/Br⁻ suffers from a similarly complicated electron transfer mechanism as I_3 ⁻/I⁻ and is even more corrosive leading to the bromination of the dye used in the study.(13) The solid state hole collector spiro-OMeTAD also has a potential more positive than I_3 ⁻/I⁻, but has multiple electron acceptor states near 0.6 V and 0.7 V vs. SCE adding complication to interpreting electron transfer kinetics between it and TiO_2 .(14) Before advanced DSSCs can be designed to take advantage of these positive redox shuttles, the complete dynamics of TiO_2 under relevant conditions must be understood.

Outer-sphere redox shuttles offer near limitless variation of the formal potential while simplifying the electron-transfer kinetics.(10) Use of these shuttles should therefore facilitate elucidation of the electron-transfer kinetics from TiO₂ at a given potential.(15) Unfortunately, back electron transfer from both the substrate and the semiconductor becomes much more problematic when using outer-sphere redox shuttles.(5-8) One measurement in particular has been shown to be affected greatly by electron transfer from the TCO is the open-circuit voltage decay to measure the electron lifetime.(8) Without restricting recombination from the TCO substrate non-linear electron lifetimes have been observed leading to incorrect analysis of the recombination mechanism. The most commonly used method to block recombination from the TCO is to form a thin "blocking layer" of TiO₂ over the TCO, preventing direct contact between the TCO and the electrolyte, which can be accomplished by spray pyrolysis, sol-gel deposition, or atomic layer deposition.(6, 16-18) Similar to recombination from the TCO, however, recombination from the blocking layer can interfere with the ability to accurately characterize the electron-transfer kinetics at the nanoparticle film/electrolyte interface.

Here, redox shuttles with very different potentials and reorganization energies are used to probe the differences in electron activity of a TiO₂ blocking layer and an insulating polymer blocking layer. Dark current, cyclic voltammetry, and electrochemical impedance measurements were performed to determine the spatially-resolved sources of recombination. These combined results allow for a complete picture of the behavior of the photoelectrodes in DSSCs under varying potential regimes.

In this work current-potential curves are found to display multiple features of current. This phenomena has been observed before in quantum dot sensitized solar cells utilizing an aqueous polysulfide electrolyte.(19, 20) These previous reports have found the cause of this additional feature to be localized surface states in the TiO₂. Outlined here is a different cause for the second feature of dark current observed due to the large difference in redox shuttles between previous reports and those herein.

2.1.2 Experimental

A blocking layer of TiO₂ was deposited on cleaned fluorine doped tin oxide, FTO, coated glass (Hartford glass) via ALD using 500 cycles of titanium isopropoxide (Sigma-Aldrich) and water as precursors at 225 °C with a Savannah 100 instrument (Cambridge Nanotech Inc.). The thickness of the blocking layer was determined to be 7 nm by ellipsometry measurements on Si wafer samples coated using the same ALD conditions, in agreement with literature reports.(5, 6, 21) A transparent TiO₂ nanoparticle layer was prepared by doctor blading a paste of TiO₂ nanoparticles (DSL 18NR-T, Dyesol) one scotch tape thickness on the FTO substrate. The resulting electrodes were annealed by heating in air to 325 °C for 5 minutes, 375 °C for 5 minutes, 450 °C for 5 minutes, and 500 °C for 15 minutes. The porous nanoparticle TiO₂ film thickness, d, was measured using a Dektak3 Surface Profiler to be 8 μm.

For electrodes utilizing a poly-phenol oxide (PPO) blocking layer, the PPO was selectively polymerized onto the exposed FTO after the nanoparticle TiO₂ film was deposited onto FTO and annealed as described above. Electropolymerization was carried out following the reported procedure of Gregg et al.(7) Briefly, electrodes with nanoparticle TiO₂ films deposited on FTO were submerged in a solution of 60 mM phenol, 90 mM 2-allylphenol, 100 mM LiClO₄ in 10/10/1 water/ethanol/2-butoxyethanol adjusted to pH 9 by addition of 10 mM tetrabutylammonium hydroxide in methanol. The potential of the electrodes was then scanned at a rate of 100 mV/s from 0 to 1.5 V vs. SCE for 60-80 cycles until the current stopped changing between cycles. The electrodes where then soaked in 10 mM tetrabutylammonium hydroxide in methanol to remove unreacted monomers and oligomers, rinsed with ethanol, and cured in air at 150 °C for 30 min. The thickness of the PPO layer was determined to be 15-16 nm by ellipsometry measurements (Alpha-SE ellipsometer, J.A. Woolam Co.) of a gold coated silicon wafer subjected to the same polymerization treatment as described above.

Sandwich DSSCs used for impedance and the current density-voltage, *J-V*, curve in figure 2.1 were fabricated by sandwiching a ~25µm thick Surlyn frame (Solaronix) between the photoanode and a platinized FTO electrode with light pressure applied at 140 °C to seal the cell. Electrical contact was achieved using copper wire and silver epoxy after scratching through the TiO₂ or PPO blocking layer with sand paper. Electrolyte was loaded through a hole in the counter electrode.

All other electrochemical measurements were three-electrode measurements made in a custom glass electrochemical cell. The photoanode was clamped in contact with the electrolyte over an opening in the cell and sealed with an o-ring. A commercial Ag/AgCl reference

electrode (ESA 66-EE009) was used for all three-electrode measurements. The counter electrode consisted of high surface area platinum mesh.

Ruthenium(II) bis(2,2'-bipyridyl)-bis(N-methylimidozole) hexafluorophosphate, [Ru(bpy)₂(MeIm)₂](PF₆)₂, was prepared following literature procedures.(22) In short, 5 mmol Ru(bpy)₂Cl₂ were dissolved in 100 mL of a 1:1 mixture of methanol and water. To this, 5 molar equivalents of N-methylimidizole were added. The reaction mixture was brought to reflux under N₂ for 4.5 hours before being allowed to cool to room temperature. Once cooled, four equivalents of NH₄PF₆ were dissolved in a minimal amount of a 1:1 mixture of methanol and water and added to the reaction mixture, which was then placed in the refrigerator overnight. The bright red precipitant was collected the following morning by vacuum filtration and washed with water and diethyl ether. The resulting product was purified on an activated neutral alumina column using acetonitrile as an eluent and characterized by NMR. 1H NMR (500 MHz, CD3CN): 3.40 (6H, s); 6.48 (2H, s); 6.82 (2H, s); 7.11 (2H, t); 7.21 (2H, s); 7.52 (2H, t); 7.68 (2H, t); 7.72 (2H, d); 7.92 (2H, t); 8.11 (2H, d); 8.20 (2H, d); 8.76 (2H, d).

All electrolytes contained 0.1 M LiClO₄, and 40 mM of [Ru(bpy)₂(MeIm)₂](PF₆)₂ in acetonitrile. Sufficient NOBF₄ was added from a stock solution to each electrolyte to oxidize 20 mM of the redox shuttle. Photoanodes were aged before use by placing in a solution of 0.1 M LiClO₄ in acetonitrile overnight. Aging the electrodes allows for stable measurements free from time dependent effects observed in the first 12-18 hours after the electrode is placed in contact with the electrolyte.(17)

Steady state current density, J, vs. applied potential, E, curves in the three electrode cell were performed using rapid stirring while cyclic voltammogram, CV, measurements were taken without stirring; both measurements used a scan rate of 10 mV/s. Electrochemical impedance

spectroscopy, EIS, was performed with a potential perturbation frequency range of $10^5 - 5 \times 10^{-2}$ Hz; no additional information was gained when probing lower frequencies. All electrochemical measurements were performed in the dark with an Autolab PGSTAT 126N. The distinction is followed throughout this work between voltage, V, (measured as the voltage across the cell) and potential, E (measured against a reference electrode in three electrode measurements).

2.1.3 Results and Discussion

Figure 2.1 displays a plot of the steady-state dark current density, J, vs. voltage, V, curve of a sandwich DSSC employing $[Ru(bpy)_2(MeIm)_2]^{3+/2+}$ as the redox shuttle. The J-V curve clearly displays two distinct features. It should be noted that $[Ru(bpy)_2(MeIm)_2]^{3+/2+}$ has a much more positive formal potential, 1.17 V vs. SCE, than typical redox shuttles used in DSSCs.(11) As a consequence the J-V curve was measured over a more positive potential range than has been previously reported.

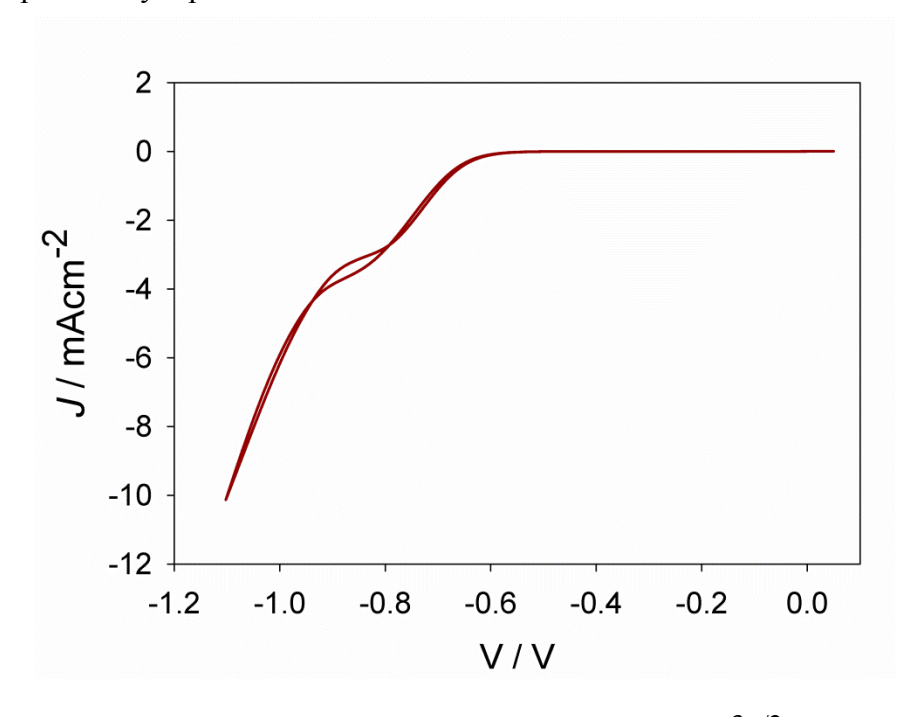


Figure 2.1. Dark *J-V* curve for a DSSC utilizing $[Ru(bpy)_2(MeIm)_2]^{3+/2+}$ as the redox shuttle.

In order to isolate the contribution to the dark current from each component of the electrode – the FTO substrate, the dense TiO₂ blocking layer, and the TiO₂ nanoparticle film – CV measurements were performed using electrodes of varying composition. Four electrodes where constructed as follows: 1) a bare FTO electrode (annealed with other electrodes since annealing has been shown to affect the electron transfer kinetics)(9) 2) nanoparticles deposited on bare FTO, 3) a flat TiO₂ blocking layer without nanoparticles, and 4) a complete electrode of nanoparticles deposited on a TiO₂ blocking layer. The results of the cyclic voltammetry measurements performed for electrodes 1-4 are displayed in figure 2.2; for reference the potential at short circuit was measured to be 0.89 V vs. Ag/AgCl. For clarity, in each cyclic voltammetry curve shown here there are one or more charge transfer events which become limited by diffusion of the redox shuttle resulting in the peaks observed (near 0.8 V, 0.05 V, and 0 V vs. Ag/AgCl).(23, 24) The focus herein is on these charge-transfer events which are responsible for the steady-state dark current in DSSCs. The data from electrodes 1 and 2 were largely overlapping; both are dominated by an immediate onset of current with a diffusion limited peak near 0.8 V vs. Ag/AgCl. The immediate current feature with a peak at 0.8 V was the only feature detected for electrode 1 and can therefore be assigned as electron transfer from the exposed FTO. Electrode 2 also has exposed FTO and the current feature peaking near 0.8 V is thus also attributed to electron transfer from the exposed FTO. Electrode 2, however, has a second feature with peak near 0 V, not observed in electrode 1, which then must correspond to electron transfer from the nanoparticle film. As expected, electrode 3 does not produce significant dark current at potentials around 0.8 V which demonstrates that electron transfer from the FTO substrate is effectively blocked. There is only a single current feature around 0.05 V which we attribute to electron transfer from the flat TiO₂ blocking layer. Electrode 4 exhibits

two dark current features. The initial feature overlaps very well with the single feature of electrode 3, thus it is also attributed to electron transfer from the TiO₂ blocking layer. Likewise, the second feature from both electrode 2 and 4 occur at the same potential, with nearly identical increases in current densities, and is therefore assigned to electron transfer from the nanoparticle TiO₂.

Similar features have been reported for CV measurements of bare TiO₂ electrodes in blocking electrolytes, which is attributed to the chemical capacitance of the nanoparticles.(25) In order to verify that the current features present in the CV measurements are due to faradaic charge transfer, and not capacitive charging, we also measured the CV's of identically treated TiO₂ electrodes in contact with a blocking electrolyte of 0.1 M LiClO₄ in acetonitrile.(26) The capacitive current, which is shown in figure 2.2 (green flat line), were found to be negligible (roughly three orders of magnitude lower) in the potential range observed here. Therefore, we attribute the current features to interfacial charge-transfer reactions as described above.

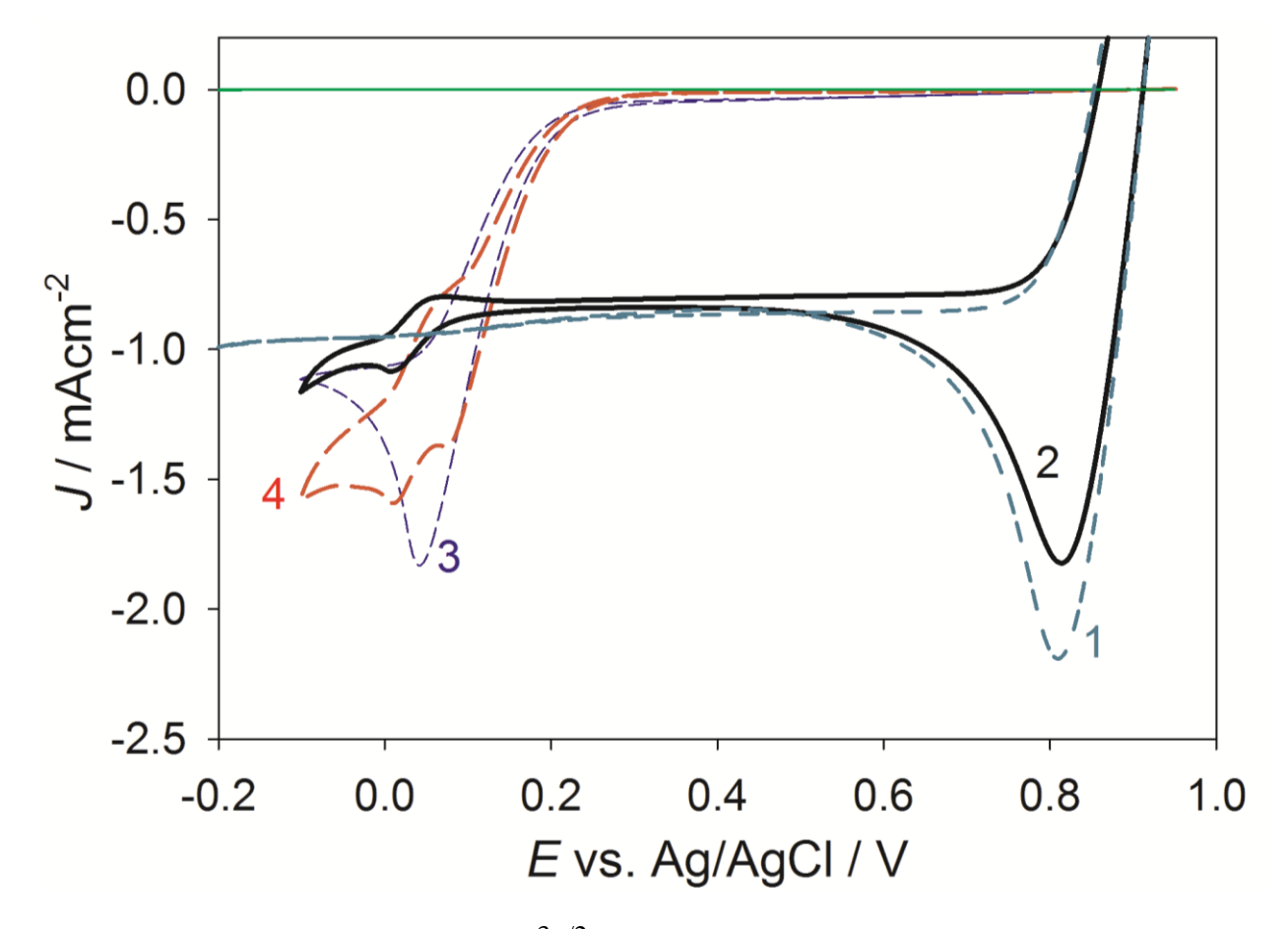


Figure 2.2. CV of $[Ru(bpy)_2(MeIm)_2]^{3+/2+}$ using three different working electrodes: 1) blank FTO 2) nanoparticle TiO_2 on FTO (black solid), 3) flat TiO_2 (blue short dash), and 4) nanoparticle TiO_2 film on flat TiO_2 (red long dash). Also shown for reference is the capacitive CV of a nanoparticle electrode in contact with blocking electrolyte (green thin solid).

Focusing on electrodes 2 and 4, there is a relatively small current contribution from the nanoparticle film as compared to the current from the flat electrode, despite the increase in surface area of over two orders of magnitude; this can be explained by a reduced concentration of [Ru(bpy)₂(MeIm)₂]³⁺ in the bulk of the nanoparticle film. Since the flat substrate reduces all of the [Ru(bpy)₂(MeIm)₂]³⁺ at the electrode surface, a condition necessary to obtain mass transport limiting current, a significantly lower concentration is present in the nanoparticle film once it becomes electrochemically active. From these combined results, the initial onset of dark

current in figure 2.1 is assigned to electron transfer from the TiO_2 blocking layer and the second feature to electron transfer from the nanoparticle film.

In an attempt to avoid the problem of electron transfer from the TiO₂ blocking layer, an insulating polymer film of PPO was employed as a blocking layer. Figure 2.3 displays steady state *J-E* curves comparing a bare FTO electrode, FTO covered with a TiO₂ blocking layer, and FTO covered with a PPO film. The resulting *J-E* curves are consistent with a conductor, semi-conductor, and insulator, respectively. While TiO₂ does effectively block electron transfer from the conductive FTO, it is only truly blocking at low applied potentials, as expected for a semiconductor. The PPO film on the other hand forms an insulating blocking layer, effectively eliminating all electron transfer over a very large potential range.

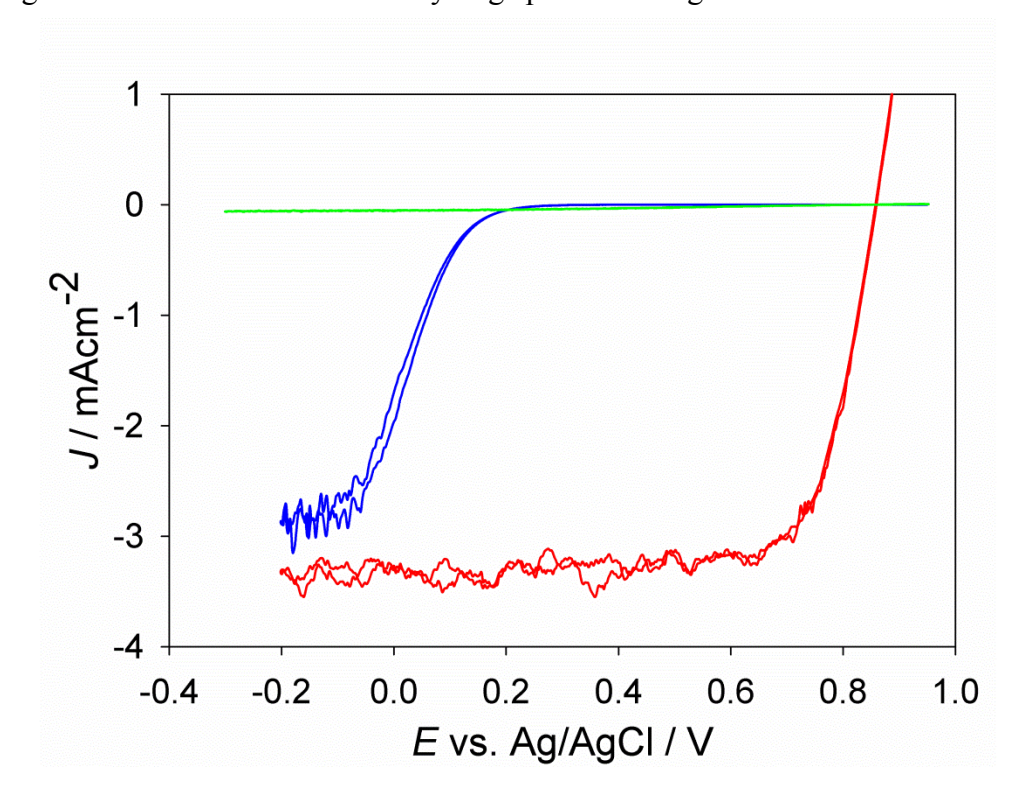


Figure 2.3. *J-E* curves for bare FTO (red) and FTO coated with films of either TiO₂ (blue) or PPO (green).

The insulating PPO film selectively deposits on the FTO substrate, leaving the nanoparticle TiO₂ exposed, which results in an ideal blocking layer for nanoparticle electrodes.(7) Therefore, a series of electrodes were fabricated using either a PPO blocking layer, a TiO2 blocking layer, or no blocking layer in combination with nanoparticle films. The J-E curves using these electrodes taken in a three electrode cell with rapid stirring are displayed in figure 2.4a. As expected, the electrode with nanoparticles on blank FTO shows immediate onset of current when it's potential scanned negative of the solution potential, quickly becoming limited by mass transport with a small addition to the current once the nanoparticle film becomes conductive. Surprisingly, however, the electrodes with the TiO₂ and PPO blocking layers behaved very similarly; both successfully passivated the FTO with an onset of dark current at nearly the same potential. This similarity was somewhat unexpected as the TiO₂ blocking layer was shown in figure 2.3 to be very active and is expected to contribute to dark current, whereas PPO is not. Also unexpectedly, the J-V curve in figure 2.1 and its analogue in figure 2.4a display significantly different shapes. These curves differ in the way the measurement was taken, figure 2.1 was a sandwich cell and figure 2.4a was taken with a three electrode cell with rapid stirring to minimize electrolyte diffusion effects. The differences in the curves in figure 2.1 and figure 2.4a were reproduced with several electrodes, clarifying that the change seen here was not due to differences in surface state densities of the electrodes but to the change in experimental conditions. In addition to the steady state J-E curves, cyclic voltammetry measurements were also performed. Figure 2.4b shows the CVs for the nanoparticle TiO₂ electrodes with either a TiO₂ or PPO blocking layer. The electrodes utilizing either the TiO₂ or the PPO blocking layer resulted in a CV with two distinct features at similar potentials. This result is also surprising

since we earlier attributed the first feature to the TiO₂ blocking layer and demonstrated that the PPO was insulating at these potentials.

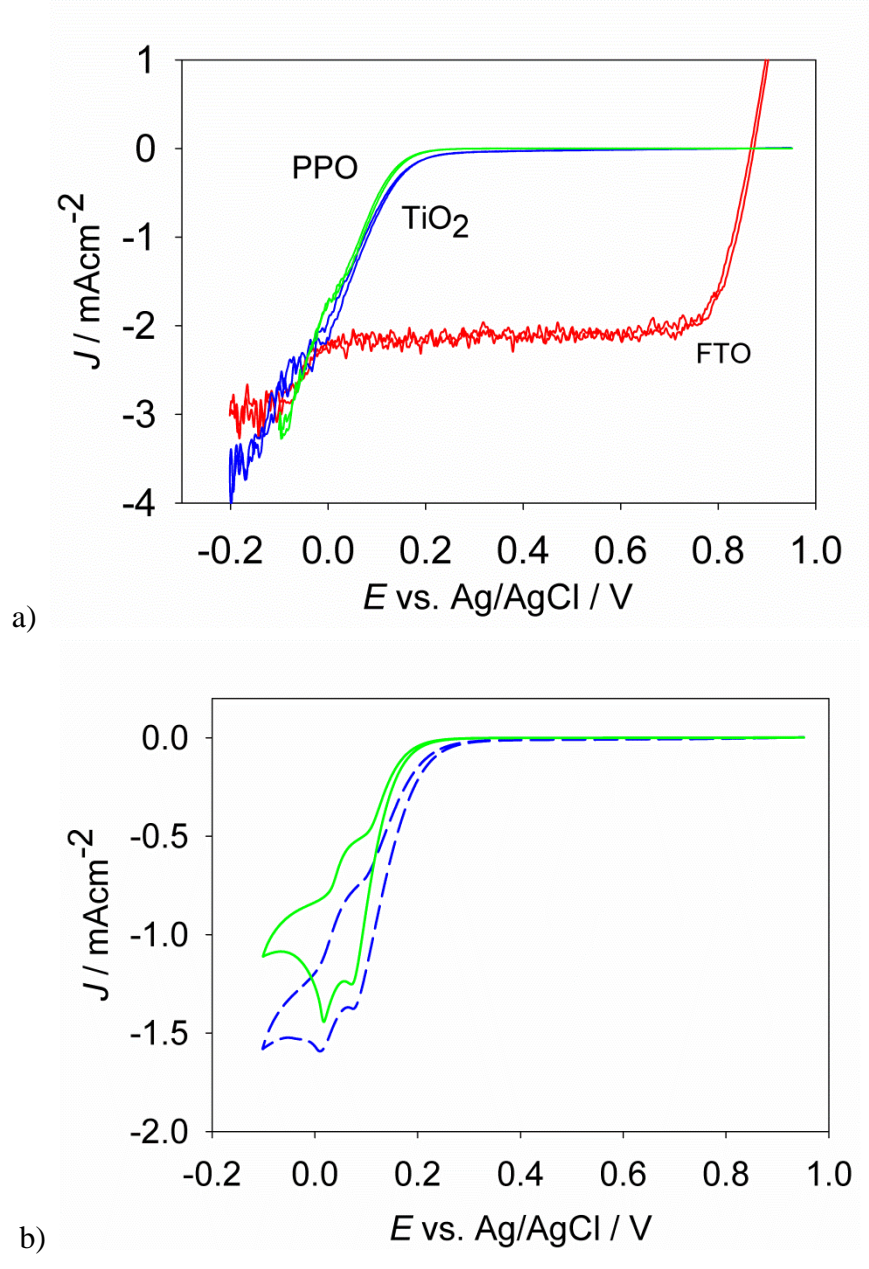


Figure 2.4. a) *J-E* curves for three electrodes each containing a TiO₂ nanoparticle film on 1) bare FTO (red), 2) FTO coated with a TiO₂ blocking layer (blue) or 3) FTO coated with a PPO blocking layer (green). b) Cyclic voltammograms of TiO₂ nanoparticle electrodes utilizing a TiO₂ (blue, dashed) or PPO (green, solid) blocking layer scanning from $0.95 \rightarrow -0.1 \rightarrow 0.95$ V vs. Ag/AgCl.

Since electrodes with either the TiO₂ or the PPO blocking layer show the same two current features, the previous interpretation that the first current feature resulted from electron transfer from the TiO₂ blocking layer must be altered or expanded. Figure 2.2 demonstrates that in electrodes with a TiO₂ blocking layer, the first feature of current could originate primarily from that blocking layer. However, we propose in the electrode using PPO as a blocking layer the first current source is the layer (or layers) of TiO2 nanoparticles which are in direct contact with the FTO. This can be explained by the Fermi level dropping off rapidly farther from the FTO as expected when there is a large charge transport resistance, R_T , in the TiO₂ film, as depicted in figure 2.5. Therefore, recombination from the TiO₂ blocking layer is indistinguishable from recombination from this first layer(s) of nanoparticles. It is the Fermi level of the TiO2 - whether blocking layer or nanoparticle - that affects the electron transfer rates. As the potential of the electrode is increased however, the resistance in the TiO₂ nanoparticle film decreases and the Fermi-level begins to flatten as shown in the diagram in figure 2.5. At these more negative potentials, recombination is dominated by the nanoparticle film due to the much higher surface area and is expected to be independent of the blocking layer, which is consistent with our observations.

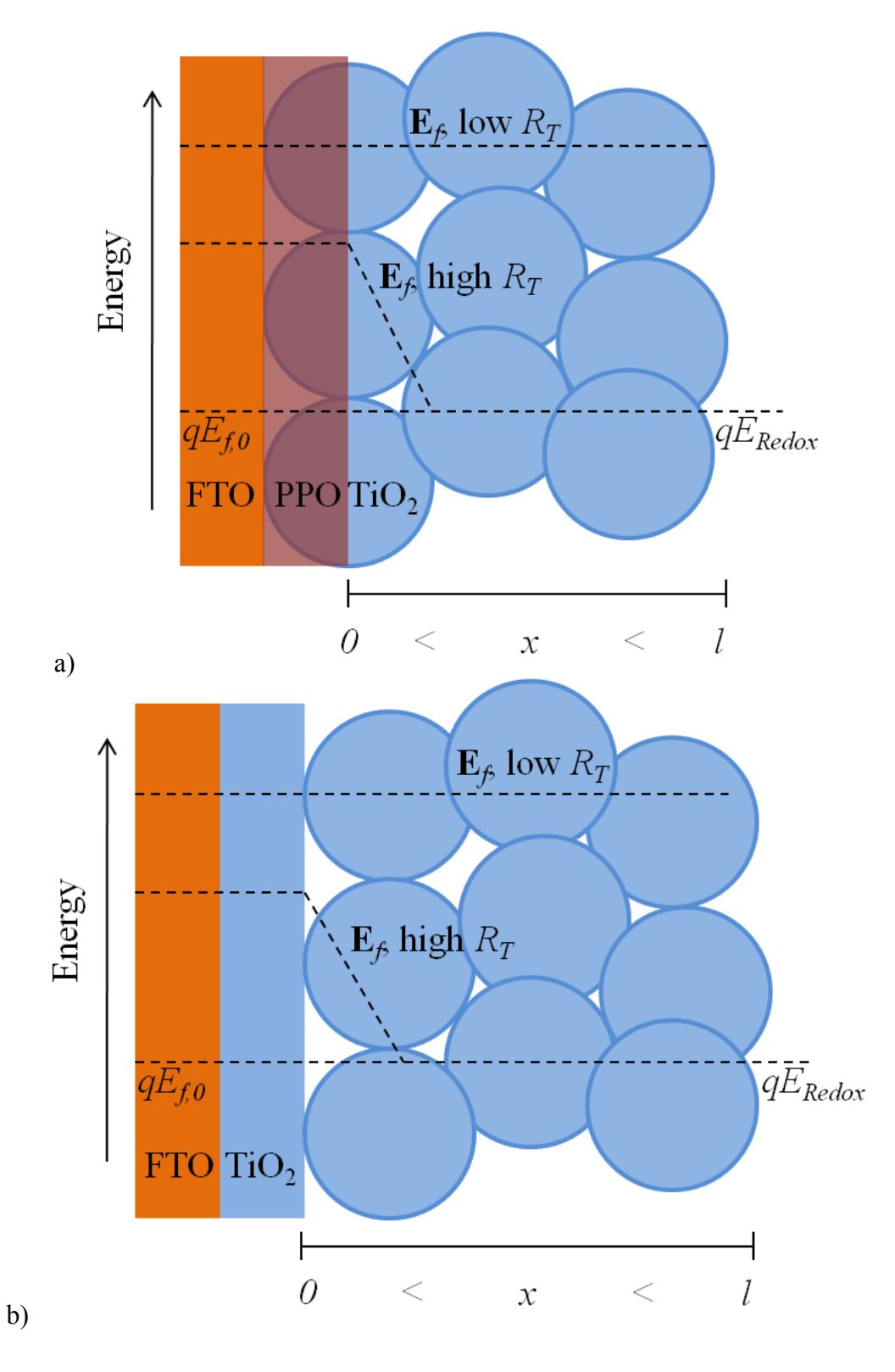


Figure 2.5. Approximate energy diagram of FTO coated with a a) PPO or b) TiO_2 blocking layer in contact with a nanoparticle TiO_2 film showing Fermi-levels when the TiO_2 has high or low R_T .

Our interpretation of the dark current originating from a small thickness of the TiO₂ nanoparticles with PPO blocking layer agrees well with the fact that flat electrodes and nanoparticle electrodes produce the same magnitude of dark current as seen when comparing figures 2.3 and 2.4a. To demonstrate the scaling of dark current more effectively the log(–*J*) of cells with blocking layers of TiO₂ both with and without nanoparticle films using [Co(*t*-Bu₂bpy)₃]^{3+/2+} and [Ru(bpy)₂(MeIm)₂]^{3+/2+} are displayed in figure 2.6. When [Co(*t*-Bu₂bpy)₃]^{3+/2+} is employed as the redox couple the dark current density increases by 2-3 orders of magnitude along with the surface area, as expected. This discrepancy highlights the issue that when alternative redox systems are employed, careful attention to indirect effects on DSSC operational principles, such as the potential dependence of the photoanode's conductivity, must be considered.

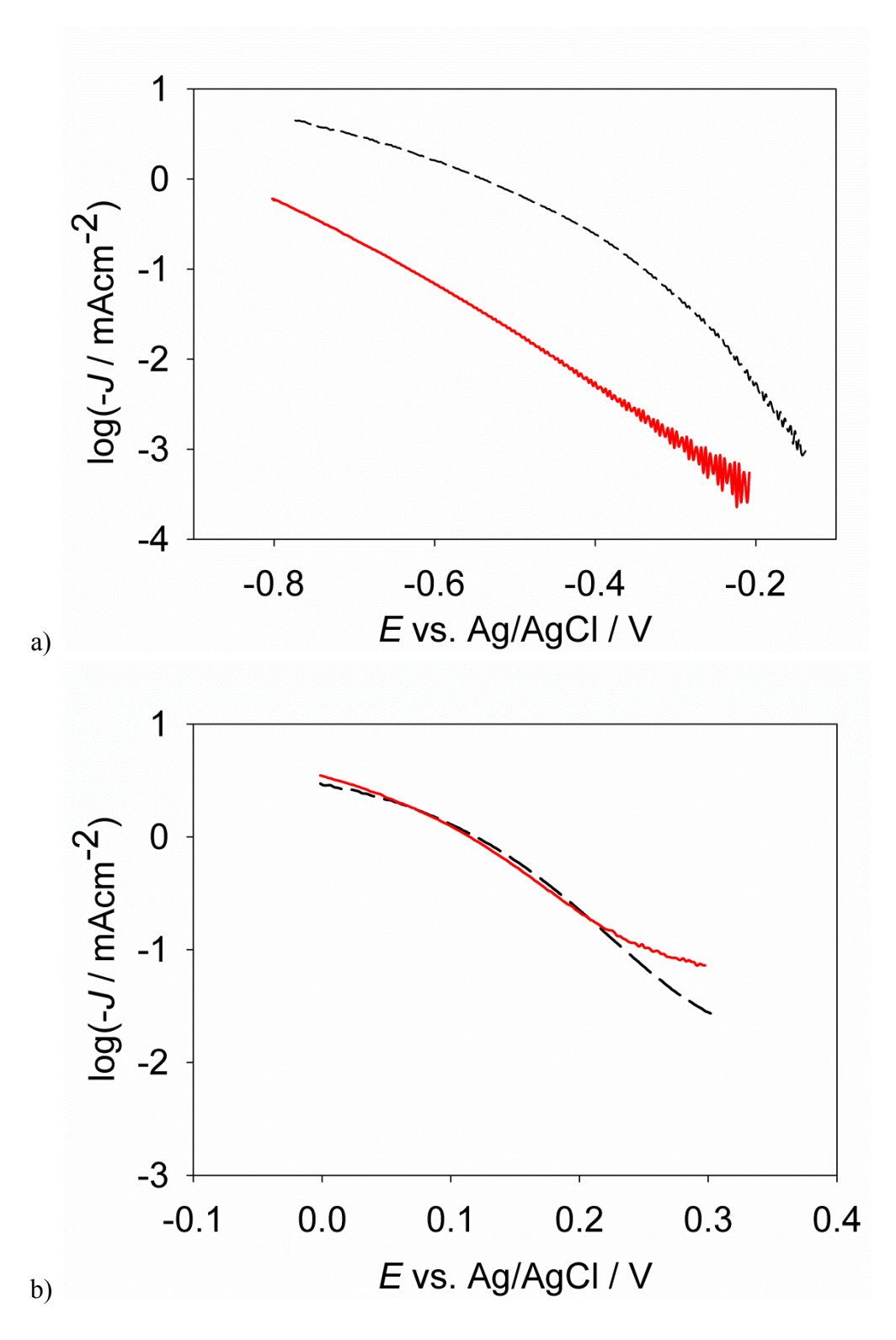


Figure 2.6. $\log(J)$ vs. *E* plots of electrodes with blocking layers of TiO_2 both with nanoparticle films (dashed black) and without nanoparticle films (solid red) using a) $\left[\mathrm{Co}(t\text{-bu}_2\mathrm{bpy})_3\right]^{3+/2+}$ and b) $\left[\mathrm{Ru}(\mathrm{bpy})_2(\mathrm{MeIm})_2\right]^{3+/2+}$.

Electrochemical impedance spectroscopy was used to test our interpretation of the initial current feature arising from electron transfer from only the first layer(s) of nanoparticles when the PPO blocking layer is employed. EIS consists of the measurement of the ac current response when a small (5 mV) ac potential perturbation is applied over top of the steady state potential, providing insight into electron transfer, transport, and capacitive processes inside the DSSC at the given steady state potential. While it is difficult to directly distinguish electron transfer from different layers of nanoparticles, measurements of the electrolyte diffusion impedance can be used as an indirect method. Representative EIS data taken of a sandwich cell under three applied potentials is displayed in figure 2.7a. The equivalent circuit used to analyze the EIS results, which has been shown to accurately describe the impedance spectra of DSSCs, is shown in figure 2.7b.(17, 27, 28) In this circuit R_S is the series resistance resulting from the FTO and contact resistance of the cell, RCT is the charge transfer resistance of charge recombination between electrons in the ${\rm TiO_2}$ and the oxidized form of the redox shuttle in solution, C_μ is the chemical capacitance of the TiO_2 film, Z_d is a Warburg diffusion element representing the impedance due to the diffusion of the redox shuttle through the electrolyte, R_{Pt} and C_{Pt} are the charge transfer resistance and double layer capacitance at the platinized counter electrode. A constant phase element, CPE, was used to better fit the impedance spectra for C_{μ} as commonly used for porous electrodes.(28)

In order to associate each feature in the EIS spectra in figure 2.7a with the correct physical process a symmetric sandwich cell with two platinized electrodes was constructed. Performing EIS with this symmetric cell allowed for the determination of R_{Pt} , C_{Pt} , and Z_d .(29) Contribution to the impedance spectra from R_{Pt} and C_{Pt} were found to be negligible ($R_{Pt} \approx 2 \Omega$) due to very rapid electron transfer between the Pt/FTO electrode and $[Ru(bpy)_2(MeIm)_2]^{3+/2+}$.

The contribution to the impedance from Z_d was found to be quite large as diffusion has been shown to be slow for bulky metal tris-bipyridyl redox shuttles and is discussed in more detail below.(10) Determination of the impedance contributions to the Nyquist plot of the DSSC sandwich cell are as follows: the first semi-circle on the left-hand (high frequency) side is attributed to impedance of the transmission line elements (R_T , R_{CT} and C_μ), while the second semi-circle (at low frequency) results from the diffusion of $[Ru(bpy)_2(MeIm)_2]^{3+}$, Z_d , through the mesoporous TiO_2 film and electrolyte. The EIS results in figure 2.7a demonstrate that as the bias potential is increased, in the range shown, R_T and R_{CT} decrease, while Z_d increases, as expected.

The Warburg element can be used to easily monitor mass transport limitations in the DSSC through the observation of both the resistance from diffusion, R_d , and the characteristic frequency of diffusion, ω_d , as

$$Z_d = R_d \frac{\tanh\left[\left(i\omega/\omega_d\right)^{1/2}\right]}{\left(i\omega/\omega_d\right)^{1/2}}$$
2.1

where $i = \sqrt{-1}$ and ω is frequency of the potential perturbation.(30) The diffusion resistance extracted from the impedance measurements is plotted in figure 2.8a, superimposed on the portion of the J-V curve measured for that cell over the same potential range. The large spike in

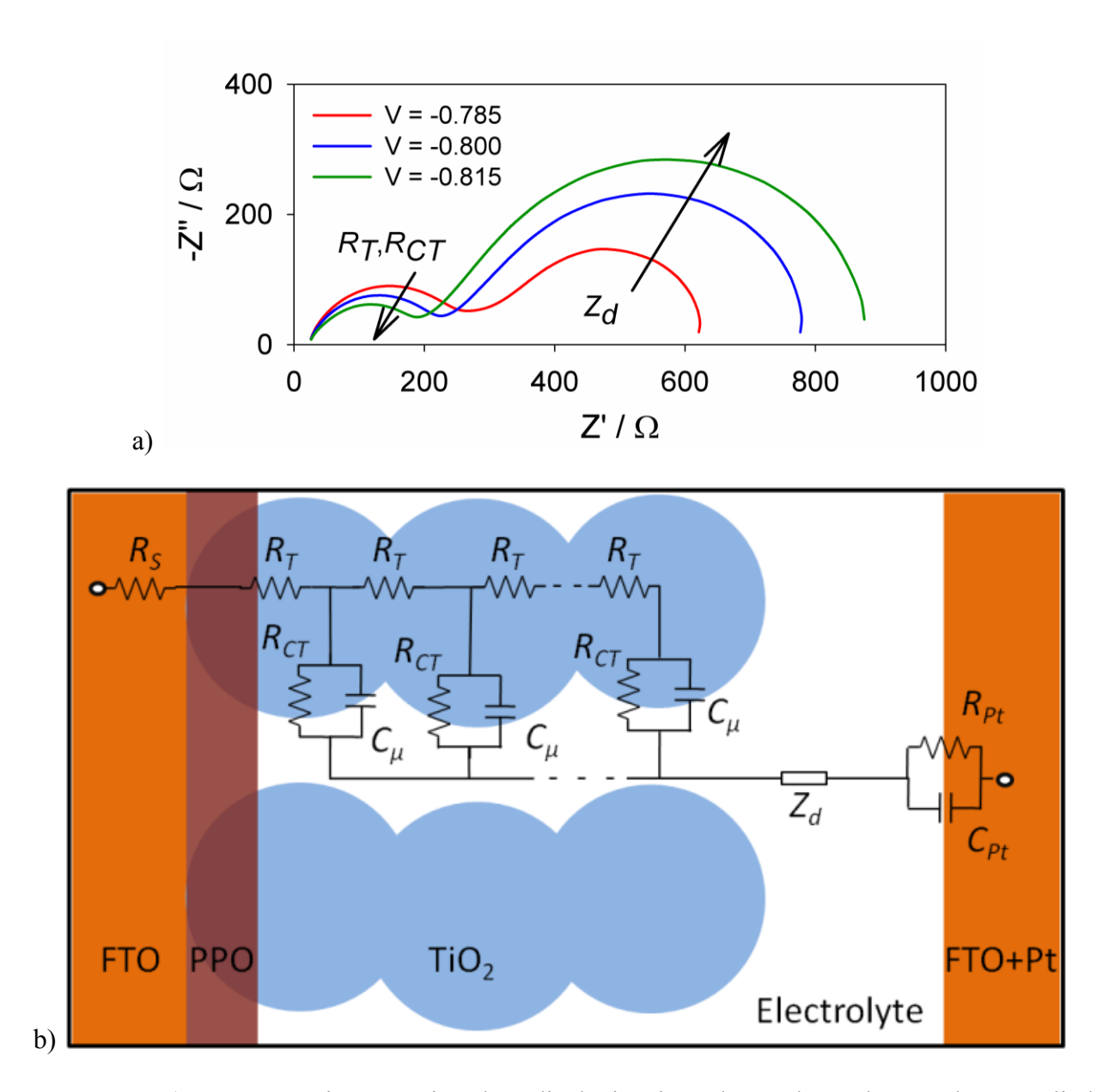


Figure 2.7. a) Representative Nyquist plots displaying impedance data taken at three applied potentials. b) Equivalent circuit of DSSC used for fitting impedance data; the fit parameters are described in the text.

 R_d as the current plateaus near -0.82 V shows the current becomes mass transport limited before the second onset of current starting at -0.85 V takes over.(10) This is in excellent agreement with the prediction that the first current onset comes from only the first few layers of nanoparticles in the film while the TiO_2 is very resistive, since the oxidized species has to

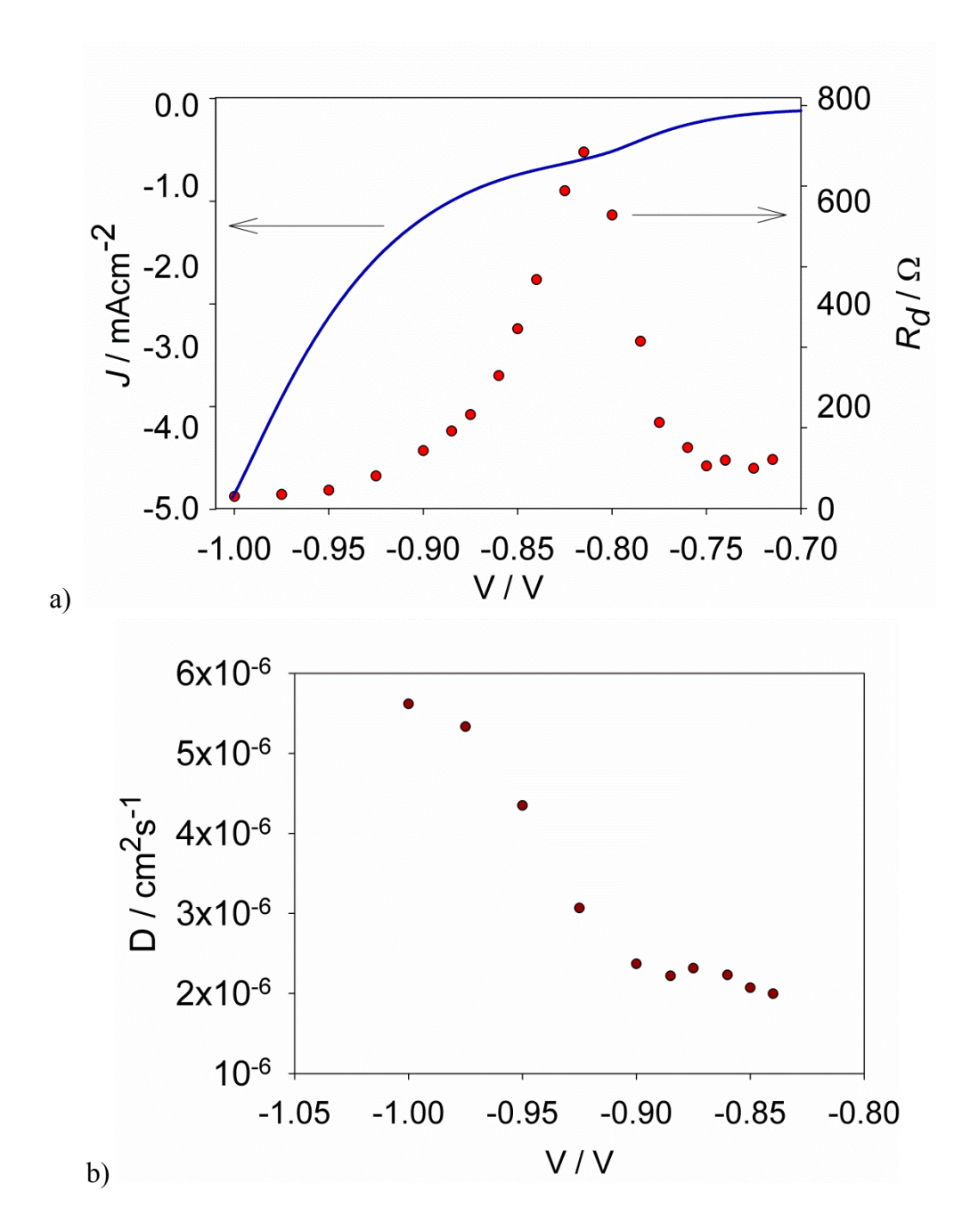


Figure 2.8. a) Overlay of J-V curve with diffusion resistance, R_d . b) Diffusion coefficient, D, of the electrolyte in the cell vs. cell voltage.

diffuse through the entire mesoporous film to be reduced. When the potential is scanned more negative, however, the TiO₂ resistance decreases, and thus electron transfer can occur throughout the film. In this situation the oxidized species can be reduced anywhere with equal

probability in the mesoporous film, which reduces the diffusion demands on the current. As a consequence, the mass transport resistance rapidly decreases and current increases.

The diffusion coefficient D of $[Ru(bpy)_2(MeIm)_2]^{3+}$ was also obtained through the Warburg diffusion element, shown in figure 2.8b, calculated through the relationship $\omega_d = l^2 D$, where l is the diffusion length of the redox shuttle. (31) This diffusion coefficient can be compared to the diffusion coefficient of $[Ru(bpy)_2(MeIm)_2]^{3+}$ through bulk acetonitrile, D_{AN} , to determine the effect of the nanoparticle film on diffusion. Therefore D_{AN} was determined for [Ru(bpy)₂(MeIm)₂]³⁺ using a sandwich cell made with two platinized FTO electrodes in acetonitrile (without a nanoparticle TiO_2 film) to be 1.0×10^{-5} cm² s⁻¹, in good agreement with other metal polypyridyl redox shuttles in acetonitrile. (29, 32) Comparing this D_{AN} value with the values of D (with a nanoparticle TiO_2 film) displayed in figure 2.7b, demonstrates that D_{AN} > D. This is in agreement with literature results that show nanoparticle TiO₂ films lower D values by a factor or five when compared to diffusion through solvent only.(32) As the potential of the cell becomes more negative, however, D increases to within a factor of two of D_{AN} . This increase in D indicates that the $[Ru(bpy)_2(MeIm)_2]^{3+}$ is diffusing through a shorter length of the TiO₂ film, consistent with electron transfer occurring farther into the TiO₂ film (farther away from the FTO).

2.1.4 Conclusions of Blocking Layers to Passivate TCO Substrate

While $[Ru(bpy)_2(MeIm)_2]^{2+/3+}$ is not an attractive redox shuttle for working DSSCs due to its high cost and light absorption, it is an excellent redox shuttle to probe electron transfer dynamics. When screening new redox shuttles in DSSCs with more positive formal potentials, blocking the conductive transparent electrode becomes much more important, as does the material used in making the blocking layer. Using the same material for both the blocking layer

and the film, results in a highly active blocking layer, limiting the ability to properly characterize the nanoparticle films electron-transfer kinetics. Use of an insulating film such as PPO allows for proper characterization of the nanoparticle electrode without necessitating the consideration of electron transfer from the blocking layer. However, use of TiO_2 blocking layers is acceptable when measuring electron transfer kinetics with the more traditional $\left[Co(t-bu_2bpy)_3\right]^{3+/2+}$ electrolyte since electron transfer rates from the blocking layer are ≤ 1 % of the rates from the nanoparticle TiO_2 film as shown in figure 2.6a.

Two current features were found in the dark J-E plots. The initial onset of dark current was demonstrated to result from electron transfer from the TiO₂ blocking layer and/or the immediate TiO₂ nanoparticles in contact with the FTO. EIS measurements established that this initial dark current plateaus due to diffusion limitations of the oxidized form of the redox shuttle through the mesoporous nanoparticle film to the first layers of TiO₂ near the FTO. This plateau is followed by an additional onset of dark current attributed to electron transfer from farther into the TiO₂ film, as the electron transport resistance decreased. At highly positive potentials TiO₂ is quite resistive, which limits its ability to maintain a constant quasi-Fermi level throughout the film. This consideration can be very important when designing new systems that are capable of achieving higher efficiencies compared to the typical N719 / TiO₂ / I₃ /I configuration, since they may operate over a very different potential range. It is important to note for future chapters that since the lifetime is the average time an electron survives in the TiO2 film before recombining, the fraction of the electrode which is active should not affect the measurement or interpretation of lifetimes, however correct interpretation of the dark current density, which is also a measure of recombination, requires knowledge of the Fermi level throughout the film as demonstrated herein.

2.2.1 Blocking Layers for Nanoparticle TiO₂ Electrodes

As discussed previously attempts at identifying one-electron, outer-sphere redox couples to replace I_3^-/I^- have thus far been largely unsuccessful. The primary shortcoming generally attributed to alternate redox shuttles is faster recombination kinetics compared to I_3^-/I^- , which results in diminished charge collection efficiencies.(6, 7, 12, 33) A good charge collection efficiency requires the electron diffusion length, L_n , to be greater than the film thickness, d.(34). The electron diffusion length is determined by competition between the charge transport time, τ_d , and the charge lifetime, τ_n , according to: $L_n = d(\tau_n/\tau_d)^{1/2}.(3, 35-37)$. The problem of poor charge collection with alternate redox systems has stimulated an intense recent effort to develop new photoanodes with improved charge transport characteristics compared to TiO_2 nanoparticles.(38-42) As an alternate approach, modification of the photoanode surface has been explored to control recombination losses.(7, 43-46) For example, it was recently demonstrated that use of atomic layer deposition, ALD, to coat TiO_2 nanoparticle electrodes with an ultra thin layer (1 ALD cycle) of alumina was able to dramatically improve the external quantum efficiencies of DSSCs employing outer-sphere redox shuttles.(6, 47)

In this section, electrochemical impedance spectroscopy, EIS, is employed to investigate the physical basis for the improved performance of DSSCs with an ultra thin alumina shell, taking care to eliminate shunting through utilization of a TiO₂ blocking layer covering the conductive glass substrate. In addition, EIS was used to investigate the charge dynamics in DSSCs employing outer-sphere redox shuttles. The equivalent circuit pioneered by Bisquert which has been shown to accurately describe the behavior of DSSCs in the dark is shown in figure 2.7b, which is employed in this work to fit impedance data.(28, 48)

2.2.2 Experimental

Photoanodes were made following the procedure in section 2.1.2. A single layer of Al₂O₃ was additionally deposited using one cycle of trimethylaluminum (Aldrich) and water as precursors at 250 °C on some electrodes (as noted in the text) immediately after removing from the furnace and cooling to 100 °C. Pulse times of 0.015 s and exposure times of 10 s were used for both precursors. All electrodes were then annealed at 500 °C in air for 30 minutes. The resulting electrodes were allowed to cool to 100 °C before being added to a solution of 0.5 mM N3, [Ru(4,4'-dicarboxy-2,2'-bipyridine)₂(NCS)₂] (Dyesol, B4 dye) in ethanol. After 20-24 hours they were removed and rinsed briefly with acetonitrile.

Sandwich DSSCs were fabricated by sandwiching a ~25µm thick Surlyn frame (Solaronix) between the photoanode and a platinized FTO electrode with light pressure applied at 140 °C to seal the cell. Electrical contact was achieved using copper wire and silver epoxy after scratching through the TiO₂ blocking layer with sand paper. Electrolyte was loaded through a hole in the counter electrode. Three-electrode measurements were made in a custom electrochemical cell. The photoanode was clamped over an opening in the cell and sealed with a viton o-ring. A Ag/AgNO₃ reference electrode containing 0.1 M [(n-butyl)₄N](PF₆) supporting electrolyte in acetonitrile was prepared fresh each day, and was found to be +0.34 V vs. SCE, similar to accepted literature values.(49) The counter electrode consisted of high surface area platinum mesh.

The cobalt outer-sphere redox couple employed in this study, cobalt(III/II) tris(4,4'-ditert-butyl-2,2'-bipyridyl) hexafluorophosphate, [Co(t-Bu₂bpy)₃](PF₆)₂, was prepared as follows. To a solution of 6•H₂O CoCl₂ in methanol, 3.1 equivalents of 4,4'-di-tert-butyl-2,2'-bipyridyl in methanol were added and the solution turned from violet to brown. After the reaction mixture was allowed to stir for two hours, four equivalents of NH₄PF₆ dissolved in methanol were added. A yellow precipitant formed and was collected via vacuum filtration, washed with methanol, water, and diethyl ether. The product was purified by dissolving in acetone and precipitating by slow addition of diethyl ether. Elemental analysis calculated for [Co(*t*-Bu₂bpy)₃](PF₆)₂: C, 56.18; H, 6.29; N, 7.28. Found: C, 56.05; H, 6.25; N, 7.17.

All electrolytes contained 0.1 M LiClO₄, 0.2 M 4-*tert*-butylpyridine, tbp, and 0.22 M of [Co(*t*-Bu₂bpy)₃](PF₆)₂. Sufficient NOBF₄ was added from a stock solution to each electrolyte to oxidize 20 mM of the cobalt unless otherwise stated. Photoanodes were aged before use by placing in a solution of 0.2 M tbp and 0.1 M LiClO₄ in acetonitrile overnight.

Photoelectrochemical measurements were performed with a Gamry Reference 600 potentiostat interfaced with a Xe Arc Lamp. An AM 1.5 solar filter and neutral density filters were used to simulate sunlight at 100 mW cm⁻². EIS was performed in the dark with an Autolab PGSTAT 126N. A constant phase element, CPE, was used to better fit the impedance spectra for C_{μ} as commonly used in literature.(50) A CPE is equivalent to a capacitor when the CPE exponent, γ , is one; for this study γ was kept close to the ideal value: $0.9 < \gamma < 1$. The charge lifetime and charge transport time are derived from equivalent circuit analysis of the impedance spectra according to $\tau_n = R_{CT}C_{\mu}$ and $\tau_d = R_TC_{\mu}$.

2.2.3 Results of Utilizing Alumina Blocking Layers

Impedance spectroscopy was used to investigate the electron dynamics in DSSCs with and without a single cycle of alumina employing cobalt bipyridyl redox shuttles. A typical Nyquist plot of a DSSC sandwich cell containing $[Co(t-Bu_2bpy)_3]^{3+/2+}$ is shown in figure 2.9a. There are two main features apparent in this impedance spectrum. The first arc seen in the high frequency region, which is essentially constant with respect to applied potential, results from the charge transfer resistance, R_{Pt} , and double layer capacitance, C_{Pt} , at the platinized counter

electrode.(28, 51) The second arc observed at lower frequencies, which depends strongly on applied potential, results from the charge transfer resistance of the recombination process, R_{CT} , and the chemical capacitance, C_{μ} , of the TiO₂ film.(28, 51) The electron transport resistance is manifested as a linear feature in the high frequency region, and can thus be obscured by the impedance of charge transfer at the platinum electrode.(28) Cyclic voltammetry measurements performed by us and others indicate that cobalt bypyridyl compounds, particularly [Co(t-Bu₂bpy)₃]^{3+/2+}, exhibit slow electron-transfer kinetics at platinum electrodes, consistent with the high electron transfer resistance observed in the impedance spectrum.(52) Attempts to minimize R_{Pt} by employing gold sputtered counter electrodes as well as various platinum deposition conditions did strictly affect the high frequency arc, thus confirming the identity of the high frequency arc, however all attempts were unsuccessful at eliminating this impedance feature.

A three-electrode cell with a high surface area platinum mesh counter electrode and Ag^+/Ag reference electrode was used in order to eliminate the R_{Pt} feature, thus isolating the impedance of the photoanode and allowing measurement of charge transport. An impedance spectrum of the three-electrode cell is shown in figure 2.9b. The arc in the high frequency region due to R_{Pt} is gone, and a straight line feature due to R_T is now apparent in the same frequency region. The arc resulting from R_{CT} and C_μ remains essentially unaffected as expected, since they should only depend on the photoanode and electrolyte which are identical in both setups. Another difference between the sandwich and three-electrode impedance spectra is the high frequency Z' intercept which is equal to the total series resistance of the cell. The increased series resistance observed in our three-electrode setup is attributed to the additional solution resistance expected for the large increase in distance between working and reference electrodes,

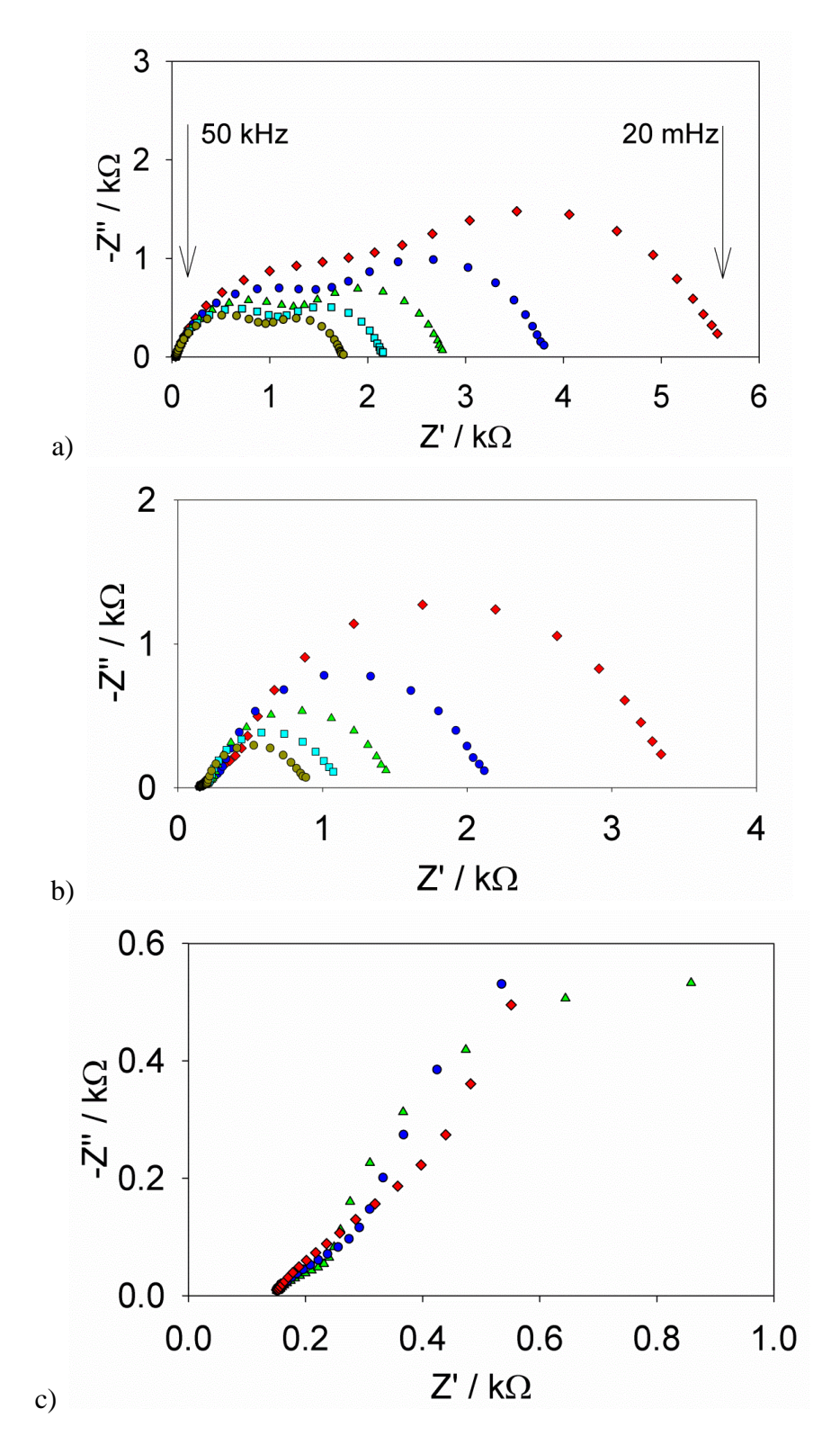


Figure 2.9. Impedance spectra of a) sandwich DSSC and b-c) three-electrode DSSC at varying potentials: -0.475 V (red diamonds), -0.500 V (blue circles), -0.525 V (green triangles), -0.550 V (cyan squares), and -0.575 V (yellow circles) vs. solution potential. The frequencies decrease from left to right as indicated in a).

which does not affect the analysis described below. Impedance spectra can now be fit to a simplified version of the equivalent circuit in figure 2.7b, removing R_{Pt} and C_{Pt} , to accurately obtain the electron transport time and lifetime and calculate the effective diffusion length, described below.

Impedance measurements using a three-electrode cell also allow the isolation of the physical effect of the alumina coating since the relevant impedance features are simultaneously determined with respect to a fixed external Ag/AgNO₃ reference electrode. Use of a reference electrode allows multiple photoanodes, with and without surface treatment, to be directly compared at a constant applied potential. Previous reports regarding the effect of alumina coatings did not utilize a reference electrode and thus complicated the analysis by comparing photoanodes at constant illumination rather than at constant potential. (53) A Nyquist plot comparing photoanodes using our three-electrode cell, at the same applied potential, both with and without an alumina coating are shown in figure 2.10(a). The obvious effect of the alumina layer is a substantial increase in R_{CT} , which can be estimated by the diameter of the semi-circle in each plot. In contrast, both C_{μ} and R_T were found to be quite similar with and without alumina at a given potential shown in figure 2.10b and 2.10c. Since $\tau_n = R_{CT}C_{\mu}$ and $\tau_d = R_TC_{\mu}$, our results indicate that the alumina increases the electron lifetime (slows recombination) but does not affect the transport time. Figure 2.10d) shows τ_n and τ_d determined from EIS for photoanodes both with and without an alumina coating. The smaller range of τ_n and τ_d values reported for DSSCs without an alumina coating results from the greatly decreased values of R_{CT} which leads to more difficulty fitting the impedance spectra at the potentials not shown. Error bars for the data shown were found to be smaller than the data markers and thus omitted.

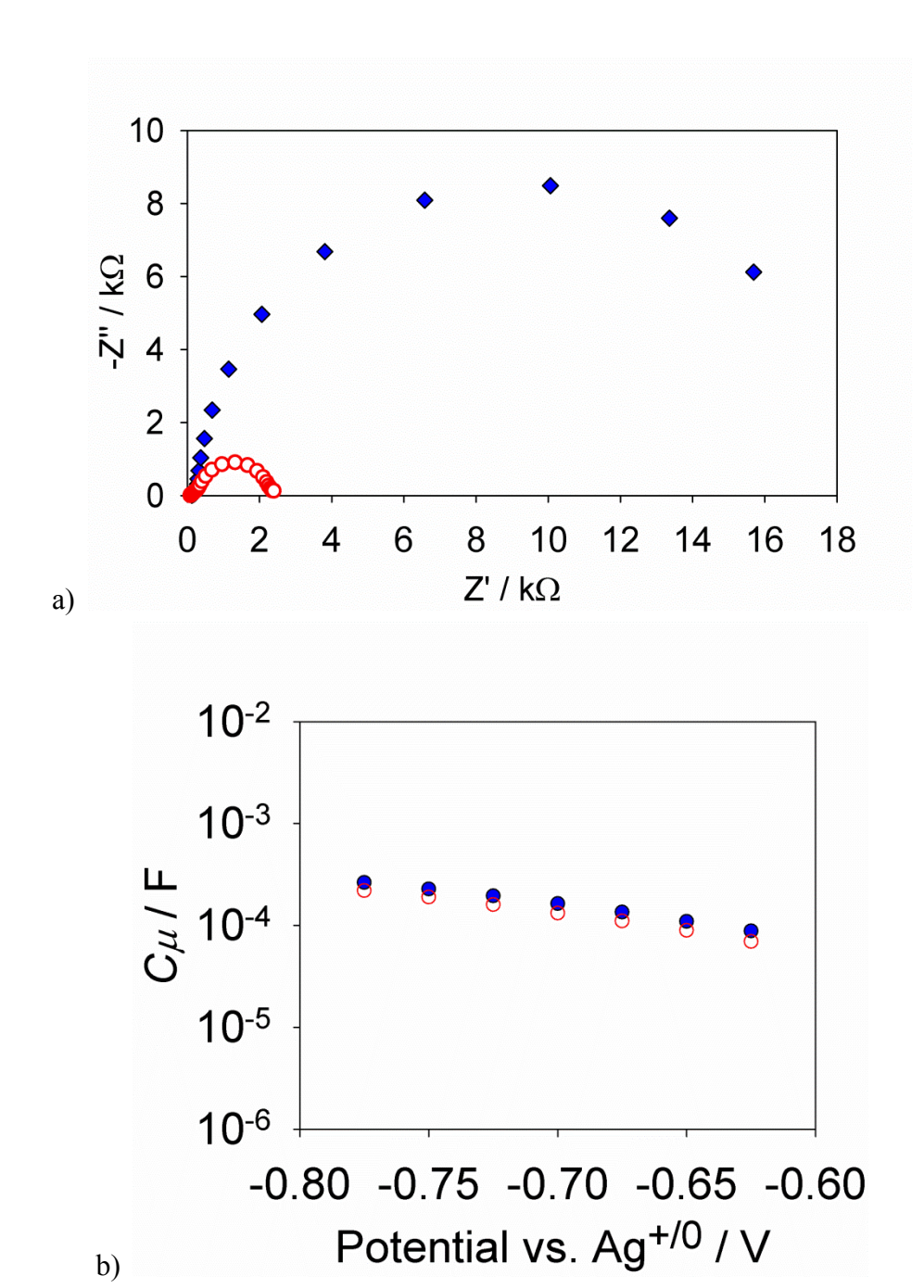
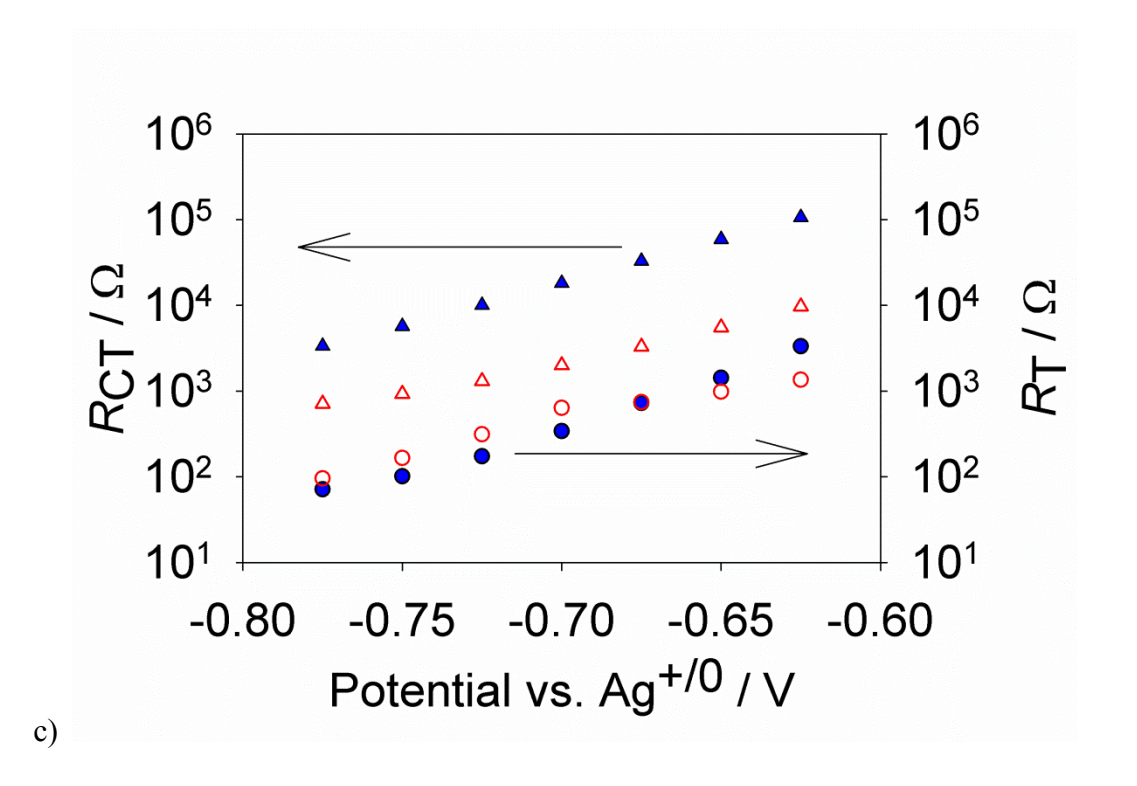
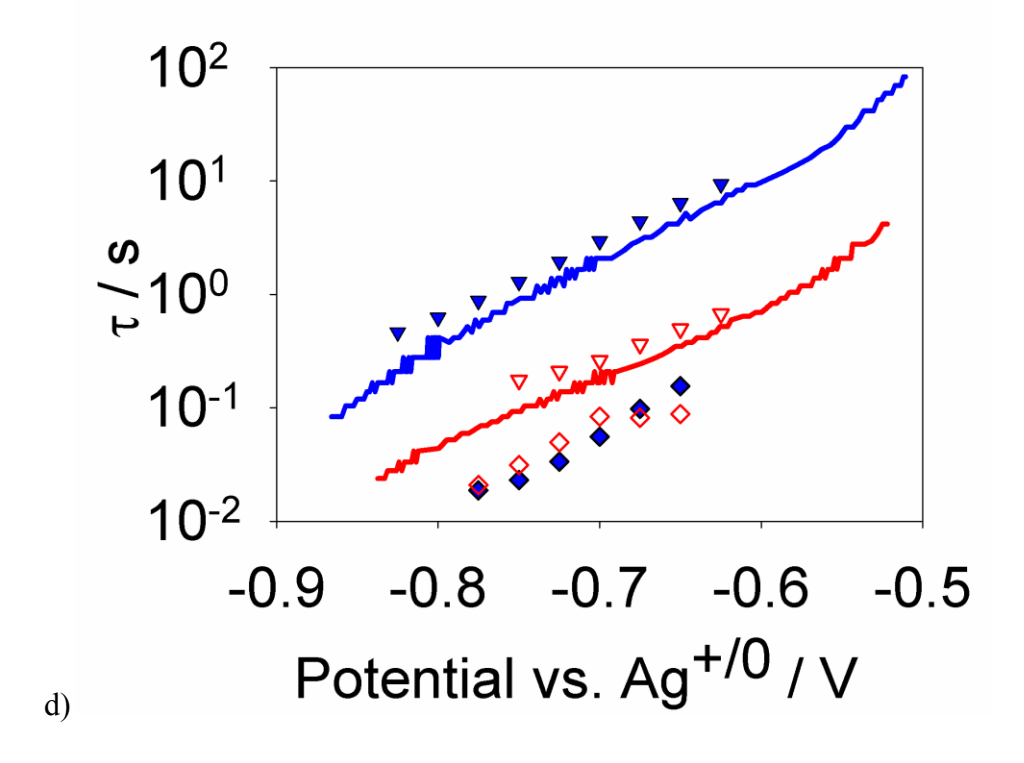


Figure 2.10. (a) Nyquist plots of three-electrode DSSCs both with (filled blue symbols) and without (hollow red symbols) alumina at -0.70 V vs. Ag $^{+/0}$. Plots of (b) capacitance, C_{μ} , and (c) charge transport, R_T (circles), and transfer, R_{CT} (triangles), resistances extracted from EIS measurements for DSSCs with an alumina coating (filled blue symbols) and without alumina (hollow red symbols). (d) Lifetimes, τ_n , measured by EIS (triangles) and OCVD (lines) and transport times, τ_d , measured by EIS (diamonds) for DSSCs both with (blue) and without (red) an alumina coating. Cells used an identical electrolyte based on $[Co(t-Bu_2bpy)_3]^{3+/2+}$ as described in text.

Figure 2.10. (Cont'd)





In principle, the increased lifetime with an alumina shell can be attributed to 1) shifting the conduction band edge which will change the driving force of the reaction 2) passivation of reactive surface states and/or 3) reduction of the electronic coupling between the photoanode and oxidized redox shuttle (i.e. acting as a tunneling barrier layer). The chemical capacitance is proportional to the density of states, and thus a shift in the conduction band would be visible by a change in C_{μ} , as has been reported for the potential determining electrolyte additives Li^{+} and tbp.(54, 55) Further, charge transport depends strongly on the occupancy of trap states in the TiO_2 bulk (determined by the difference in energy between the quasi-fermi level and the conduction band edge), which manifests as an exponential potential dependence of transport time (with a constant conduction band). Since a consistent potential with respect to the reference was applied on the electrodes with and without an alumina layer, a shift in the conduction band would produce a concomitant shift in the charge transport time, which we do not observe. Due to the invariance of C_{μ} and R_{T} (and thus τ_{d}) we can conclude that the alumina layer does not shift the conduction band of the TiO_2 electrodes or change the electron transport properties.

If passivation of surface states significantly contributes to the increased lifetime, it should be apparent in the capacitance measurements; either the magnitude (which is related to the density of states) or a frequency dispersion (attributable to inhomogeneous reaction rates). As stated above, however, the capacitance results were found to be invariant with the alumina coating. The values for the CPE exponent, γ , were also very similar (difference of ~ 0.02) indicating a similarity in ideality of capacitance behavior between the two electrodes. This result is surprising since surface state passivation was suggested by us and others to explain the effect of the alumina coating (at least in part).(6, 27, 47, 56) In a previous report where an alumina shell was introduced by a dip coating method, it was suggested that a non-exponential

dependence of lifetime with potential indicated recombination from surface states, and the lifetime must be probed while the quasi-Fermi level moves more positive than I was able to measure with EIS in order to observe a change in the surface trap density. (27, 56) Open-circuit voltage decay, OCVD, measurements were therefore performed by applying a negative potential (-0.9 V vs. Ag/AgNO₃) to the photoanode and observed the resulting voltage decay in the dark when the cell is switched to open-circuit conditions. The voltage decays were transformed into lifetimes according to: $\tau_n = (k_B T / q)(dV_{oc} / dt)^{-1}$.(57) Care was taken to avoid applying too negative a potential to the photoanode which results in the oxidized form of the redox couple (acceptor species) being depleted at the electrode surface thereby producing a misleadingly high measurement of τ_n at early times (i.e. hysteresis effects). Lifetimes for electrodes with and without alumina measured by OCVD are displayed in figure 2.10d. The lifetimes are nominally identical to those measured with EIS, continuing to show an exponential dependence at very positive potentials and are remarkably parallel across the entire potential range. This result contrasts results reported by others; the discrepancy can partially be attributed to the fact that a TiO₂ blocking layer on the FTO substrate was not utilized in other work.(8, 27, 53, 56) In the absence of a blocking layer, the OCVD measurements include electron transfer from the FTO (shunting) which can complicate the interpretation, including the reported deviation from the exponential dependence for the lifetime. (8) Previous comparisons of lifetimes of electrodes with and without alumina coatings not only includes the desired decrease in recombination from the TiO₂ but also a decrease in recombination from the conductive glass substrate.(8, 27, 56) addition, in previous reports, there was no pretreatment of the electrodes reported which, as we described above, is necessary to remove aging effects from complicating the results. Thus, contrary to our expectations and reports by others, we found when aging and shunting effects

were eliminated, there is no physical evidence that indicates the alumina layer affected the mechanism of recombination, i.e. elimination of recombination via surface states.

The alumina shell can also act as an electron tunneling barrier layer which will decrease the rate constant of recombination, corresponding to an increase in electron lifetime. Since ALD is a self-limiting process, one cycle will result in at most (but generally less than) a single monolayer of alumina, which is unlikely to be pinhole free. The necessary condition for an effective barrier layer is for it to be pinhole free to the reactive species – in this case the oxidized redox shuttle. The alumina precursors (trimethylaluminum and H_2O) are both substantially smaller than $[Co(t-Bu_2-bpy)_3]^{3+}$, therefore any open sites on the TiO_2 surface that would have been accessible to $[Co(t-Bu_2-bpy)_3]^{3+}$ should have been filled by alumina (i.e. any pinhole that is too small to be filled with alumina is also too small for $Co(t-Bu_2-bpy)_3]^{3+}$). Due to nonnegligible differences between electrodes, it is difficult to quantify the actual attenuation of recombination, however the lifetimes were found to increase by a factor of 4-8 with an alumina layer, which is fairly large but certainly feasible. Therefore it is proposed that the dominant effect of even a single ALD cycle of alumina is to present a tunneling barrier layer.

To further investigate that electron tunneling barrier was the main effect of alumina blocking layers, flat TiO₂ electrodes where prepared to measure electron transfer kinetics under simplified conditions. Approximately 15 nm of TiO₂ were deposited on clean FTO by 1000 cycles of ALD. These electrodes were fabricated into a series of electrodes with 0-4 cycles of Al₂O₃ deposited by ALD. Dark current measurements and EIS were performed to probe the electron transfer kinetics with this series of electrodes in contact with a [Ru(bpy)₂(MeIm)₂]^{2+/3+} electrolyte, shown in figure 2.11. As expected the dark current density decreases at a given potential with each additional cycle of alumina. The dark current originating from the TiO₂

conduction band will theoretically follow an exponential dependence with potential as recombination is controlled by conduction band electron concentration. In order to clarify the portion of the plot which follows this dependency, a plot of $\ln(-J)$ is included in figure 2.11 where a clear linear dependency is followed roughly between 0 and 0.2 V vs. Ag/AgCl. The deviation of the exponential dependence at more negative regions is brought on by mass transport limitations and consequently this potential range was ignored from this analysis as the current is not limited by recombination any longer. There is also a deviation of current from exponential dependence at more positive potentials where the current flattens to nearly no dependency on potential. This range is thought to be controlled by electron transfer at very small scratches or defects in the film which allow the FTO to directly transfer electrons to the solution. This assessment is based on experiments which compared different thicknesses of TiO₂ deposited by ALD in which the flat portion of the current at positive potentials decreased with more ALD cycles while the linear increase in current was unaffected by varying the number of cycles of TiO₂.

It has been proposed that if Al_2O_3 deposition passivated surface states then the first cycle of deposition would have a disproportionately large influence in decreasing the recombination than additional cycles. (58) This concept can be examined more readily by observing the change in recombination resistance, and thus the electron transfer rate, across the interface. EIS was performed in the potential range where the dark current of each of the electrodes is exponentially dependent on potential and thus controlled by the rate of electron transfer from TiO_2 . The resulting resistance, R_{CT} , values of electron transfer across the interface are displayed as $ln(R_{CT}^{-1})$ in figure 7.11c. This plot clearly demonstrates that the first cycle of alumina does not provide a disproportionately large dampening of electron transfer when compared to the next

three cycles. The linearity of the plot of $\ln(R_{CT}^{-1})$ is strong evidence that the first cycle of alumina does not passivate surface states but acts as an electron tunneling barrier. The slope of the line, (taking into account the average deposition rate of Al_2O_3 is ~ 1.1 Å per cycle) provides the dampening constant, $\beta \approx 0.69$ Å⁻¹ at 0.05 V, 0.74 Å⁻¹ at 0.10 V and 0.83 Å⁻¹ at 0.15 V vs. Ag/AgCl. The ideal value for β of an electron tunneling barrier layer is 1 Å⁻¹.(58) The discrepancy between the observed value and the ideal value should not be over analyzed. The deposition growth rate of ~ 1.1 Å per cycle of alumina is a measure of the average growth rate of 50 and 100 ALD cycles; the first few ALD cycles cannot be guaranteed to follow the same rate, introducing uncertainty in the effective thickness of the alumina layers. Taking this into consideration the value obtained for β may underestimate the actual value.

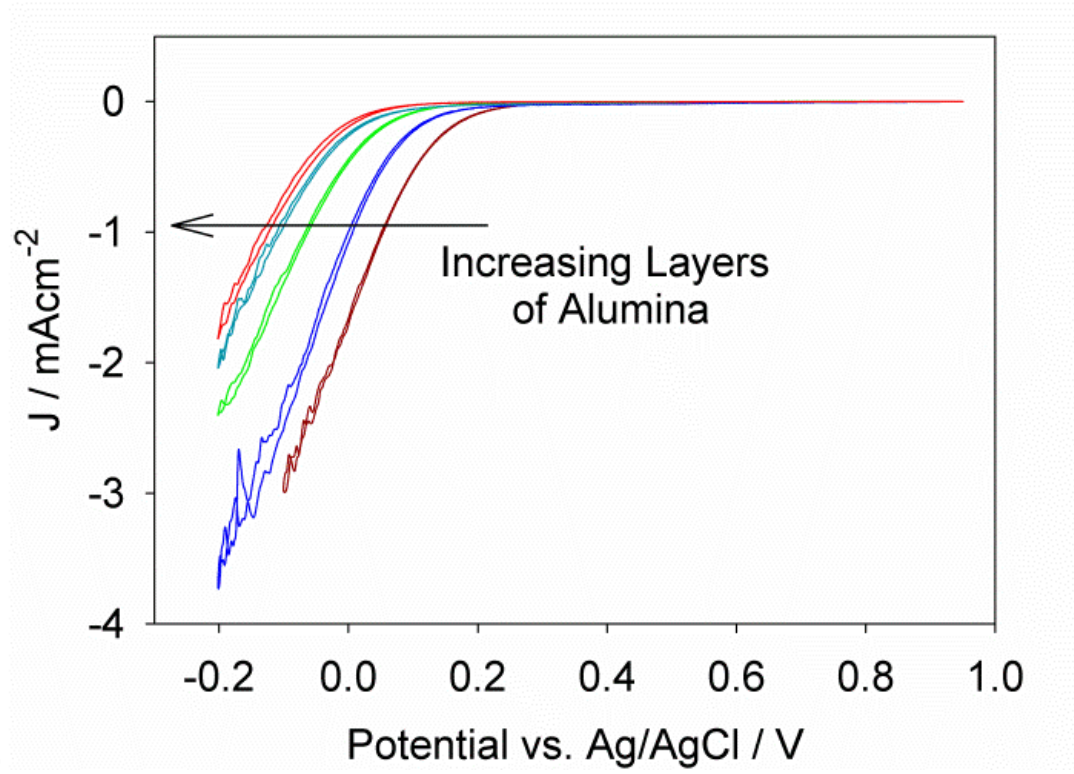
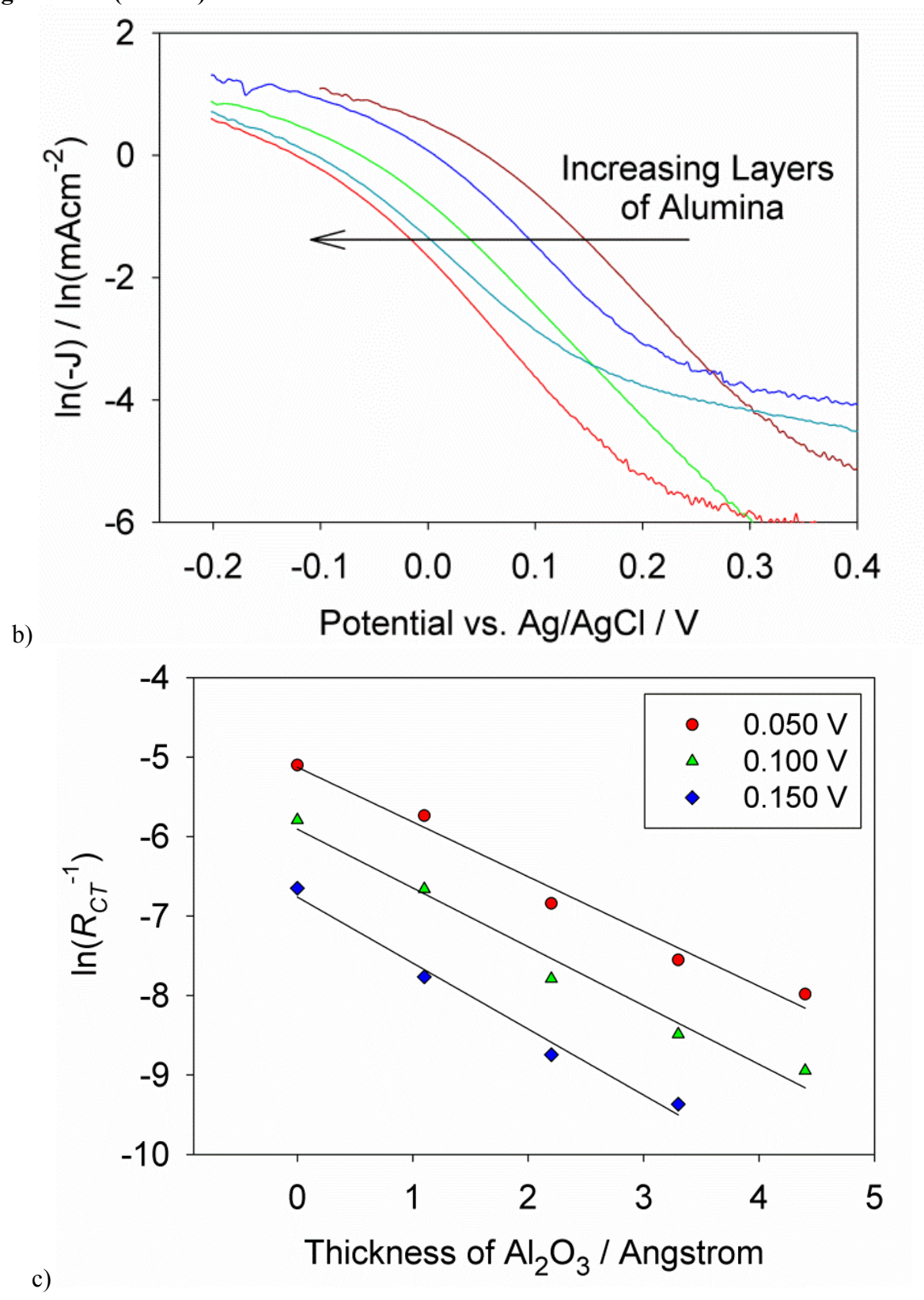


Figure 2.11. a) Dark current density, b) natural log of the dark current density, and c) $\ln(R_{CT}^{-1})$ for electrodes with 0-4 layers of alumina coating 1000 ALD cycles of TiO₂ on FTO. The β values provided by the slope of the lines in c) are 0.69 Å at 0.05 V, 0.74 Å at 0.10 V and 0.83 Å at 0.15 V vs. Ag/AgCl.

Figure 2.11. (Cont'd)



2.2.4 Conclusions to Utilizing Alumina Blocking Layers in DSSCs

Electrochemical impedance spectroscopy is an excellent technique to probe relevant physical processes in DSSCs. Use of a three-electrode cell was found to be an ideal way to overcome the large charge-transfer resistance at the counter electrode thereby enabling EIS to measure charge transport and lifetimes of DSSCs containing outer-sphere redox shuttles. When the FTO substrate was coated and aging effects considered, no evidence of surface state recombination was found at any potential studied either with or without an Al₂O₃ layer. Additionally, no evidence was found that an Al₂O₃ layer has any effect on the conduction band energy. One ALD layer of Al₂O₃ was determined to act similarly as additional layers as a tunneling barrier layer, only affecting the interfacial charge transfer resistance, thus increasing the electron lifetime.

REFERENCES

REFERENCES

- 1. B. Oregan, M. Gratzel, *Nature* **353**, 737 (Oct 24, 1991).
- 2. L. Peter, Acc. Chem. Res. 42, 1839 (Nov. 2009).
- 3. L. M. Peter, J. Phys. Chem. C 111, 6601 (May, 2007).
- 4. G. Boschloo, A. Hagfeldt, Acc. Chem. Res. 42, 1819 (2009).
- 5. B. M. Klahr, T. W. Hamann, J. Phys. Chem. C 113, 14040 (2009).
- 6. T. W. Hamann, O. K. Farha, J. T. Hupp, *J. Phys. Chem. C* **112**, 19756 (Dec, 2008).
- 7. B. A. Gregg, F. Pichot, S. Ferrere, C. L. Fields, *J. Phys. Chem. B* **105**, 1422 (Feb, 2001).
- 8. P. J. Cameron, L. M. Peter, *J. Phys. Chem. B* **109**, 7392 (Apr., 2005).
- 9. P. J. Cameron, L. M. Peter, S. Hore, *J. Phys. Chem. B* **109**, 930 (2005).
- 10. T. W. Hamann, J. W. Ondersma, *Energy Environ. Sci.* **4**, 370 (2011).
- 11. A. B. F. Martinson, T. W. Hamann, M. J. Pellin, J. T. Hupp, *Chem. Eur. J.* **14**, 4458 (2008).
- 12. T. W. Hamann, R. A. Jensen, A. B. F. Martinson, H. Van Ryswyk, J. T. Hupp, *Energy Environ. Sci.* 1, 66 (2008).
- 13. C. Teng et al., Org. Lett. 11, 5542 (Dec, 2009).
- 14. J. Garcia-Canadas et al., Synthetic Met. 156, 944 (2006).
- 15. J. W. Ondersma, T. W. Hamann, J. Am. Chem. Soc. 133, 8264 (2011).
- 16. P. J. Cameron, L. M. Peter, *J. Phys. Chem. B* **107**, 14394 (2003).
- 17. J. W. Ondersma, T. W. Hamann, J. Phys. Chem. C 114, 638 (2010).
- 18. G. P. Smestad et al., Solar Energy Mater. Solar Cells 76, 85 (2003).
- 19. I. Mora-Sero et al., Acc. Chem. Res. 42, 1848 (2009).
- 20. J. Bisquert, F. Fabregat-Santiago, I. Mora-Sero, G. Garcia-Belmonte, S. Gimenez, J. *Phys. Chem. C* **113**, 17278 (2009).

- 21. T. W. Hamann, A. B. F. Martinson, J. W. Elam, M. J. Pellin, J. T. Hupp, *J. Phys. Chem. C* **112**, 10303 (2008).
- 22. T. W. Hamann, F. Gstrein, B. S. Brunschwig, N. S. Lewis, *Chem. Phys* **326**, 15 (2006).
- 23. A. J. Bard, L. R. Faulkner, *Electrochemical Methods: Fundamentals and Applications*. (John Wiley & Sons, New York, 1980).
- 24. R. S. Nicholson, I. Shain, *Anal. Chem.* **36**, 706 (1964).
- 25. J. Bisquert et al., Inorg. Chem. Acta **361**, 684 (2008).
- 26. F. Fabregat-Santiago, I. Mora-Sero, G. Garcia-Belmonte, J. Bisquert, *J. Phys. Chem. B* **107**, 758 (2003).
- 27. J. Bisquert, A. Zaban, M. Greenshtein, I. Mora-Sero, *J. Am. Chem. Soc.* **126**, 13550 (Oct, 2004).
- 28. F. Fabregat-Santiago, J. Bisquert, G. Garcia-Belmonte, G. Boschloo, A. Hagfeldt, *Sol. Energy Mat. Sol. Cells* **87**, 117 (2005).
- 29. M. Liberatore *et al.*, *Electrochim. Acta* **55**, 4025 (2010).
- 30. M. E. Orazem, B. Tribollet, *Electrochemical Impedace Spectroscopy*. (John Wiley & Sons, Hoboken, 2008).
- 31. A. Hauch, A. Georg, *Electrochim. Acta* **46**, 3457 (2001).
- 32. J. J. Nelson, T. J. Amick, C. M. Elliott, J. Phys. Chem. C 112, 18255 (Nov, 2008).
- 33. G. Oskam, B. V. Bergeron, G. J. Meyer, P. C. Searson, *J. Phys. Chem. B* **105**, 6867 (Jul, 2001).
- 34. J. Halme, G. Boschloo, A. Hagfeldt, P. Lund, J. Phys. Chem. C 112, 5623 (2008).
- 35. A. J. Frank, N. Kopidakis, J. van de Lagemaat, *Coordination Chemistry Reviews* **248**, 1165 (Jul, 2004).
- 36. A. B. F. Martinson, T. W. Hamann, M. J. Pellin, J. T. Hupp, *Chem. Eur. J.* **14**, 4458 (2008).
- 37. A. N. M. Green, E. Palomares, S. A. Haque, J. M. Kroon, J. R. Durrant, *Journal of Physical Chemistry B* **109**, 12525 (Jun, 2005).
- 38. K. Zhu, N. R. Neale, A. Miedaner, A. J. Frank, *Nano Letters* 7, 69 (Jan, 2007).

- 39. J. R. G. Jennings, A.; Peter, L.M.; Schmucki, P.; Walker, A.B., *J. Am. Chem. Soc.* **130**, 13364 (2008).
- 40. A. B. F. Martinson et al., J. Phys. Chem. A 113, 4015 (Apr, 2009).
- 41. A. B. F. Martinson, J. E. McGarrah, M. O. K. Parpia, J. T. Hupp, *Phys. Chem. Chem. Phys.* **8**, 4655 (2006).
- 42. M. Law, L. E. Greene, J. C. Johnson, R. Saykally, P. D. Yang, *Nat. Mater.* **4**, 455 (Jun, 2005).
- 43. J. C. Guo, C. X. She, T. Q. Lian, J. Phys. Chem. C 111, 8979 (Jun, 2007).
- 44. E. Palomares, J. N. Clifford, S. A. Haque, T. Lutz, J. R. Durrant, *J. Am. Chem. Soc.* **125**, 475 (Jan, 2003).
- 45. E. Palomares, J. N. Clifford, S. A. Haque, T. Lutz, J. R. Durrant, *Chem. Commun.*, 1464 (2002).
- 46. M. Law et al., J. Phys. Chem. B 110, 22652 (Nov, 2006).
- 47. B. M. Klahr, T. W. Hamann, J. Phys. Chem. C 113, 14040 (Aug. 2009).
- 48. J. Bisquert, *Phys. Chem. Chem. Phys* **2**, 4185 (2000).
- 49. C. K. Mann, K. K. Barnes, *Electrochemical reactions in nonaqueous systems*. (Marcel Dekker Inc., New York, 1970).
- 50. Q. Wang et al., J. Phys. Chem. B 110, 25210 (2006).
- 51. L. Han, N. Koide, Y. Chiba, A. Islam, T. Mitate, *Chimie*, 645 (2006).
- 52. S. A. Sapp, C. M. Elliott, C. Contado, S. Caramori, C. A. Bignozzi, *J. Am. Chem. Soc.* **124**, 11215 (Sep, 2002).
- 53. M. Liberatore *et al.*, *Appl. Phys. Lett* **94**, 173113 (2009).
- 54. F. Fabregat-Santiago et al., J. Am. Chem. Soc. 131, 558 (Jan, 2009).
- 55. S. A. Hague *et al.*, *J. Phys. Chem. B* **104**, 538 (Jan, 2000).
- 56. F. Fabregat-Santiago *et al.*, *J. Appl. Phys.* **96**, 6903 (Dec, 2004).
- 57. A. Zaban, M. Greenshtein, J. Bisquert, *ChemPhysChem* 4, 859 (2003).
- 58. C. Prasittichai, J. T. Hupp, *J. Phys. Chem. Lett.* **1**, 1611 (2010).

Chapter 3: Recombination and Diffusion Length in Dye Sensitized Solar Cells with Outer-Sphere Redox Shuttles

3.1 Introduction

The incident photon to current efficiencies, IPCEs, with DSSCs utilizing $[Co(4,4'-R_2bpy)_3]^{3+/2+}$ have been shown to increase as R goes from H to Me to *t*-butyl; in some reports $[Co(t-Bu_2bpy)_3]^{3+/2+}$ demonstrated similar IPCEs as I_3^{-}/I^{-} .(6, 11) The question remained as to what fundamental process limits performance between the cobalt redox shuttles. The main processes that the redox shuttle is involved in are regeneration and recombination. Slow

regeneration results in the oxidized dye being reduced by excited electrons in TiO₂; this, combined with fast recombination of electrons to the oxidized redox shuttle, prevent efficient charge collection leading to poor performance. The observed increase in IPCE between substituted R groups coincides with an increase in the bulk, and thus the insulating nature, of R as well as an increasingly positive E_{redox} ; $[Co(Me_2bpy)_3]^{3+/2+}$ and $[Co(t-Bu_2bpy)_3]^{3+/2+}$ are 130 and 160 mV more negative than $[Co(bpy)_3]^{3+/2+}$ respectively. As E_{redox} moves more positive, the driving force for regeneration decreases and the driving force for recombination increases. The question remained whether fast recombination, slow regeneration or both limit device performance with these cobalt based shuttles.

Recently, to determine if the difference in DSSC performance between this series of cobalt shuttles was due to regeneration limitations, Klahr and Hamann compared DSSC IPCEs with the series of shuttles: $[Co(R_2bpy)_3]^{3+/2+}$ (where R = H, Me, or *t*-butyl) with two dyes a) N3 and b) $[Ru(bpy)_2(4,4'\text{-dicarboxy-bpy})](PF_6)_2.(11)$ The ground state potential for $[Ru(bpy)_2(4,4'\text{-dicarboxy-bpy})](PF_6)_2$ is 500 mV more positive than that of N3; consequently, all shuttles will have an increased driving force for regeneration with $[Ru(bpy)_2(4,4'\text{-dicarboxy-bpy})](PF_6)_2$. Since $[Co(t\text{-Bu}_2bpy)_3]^{3+/2+}$ displays excellent performance with N3, it would not be expected to improve with an increased regeneration driving force, however the other two cobalt shuttles would be expected to improve relative to $[Co(t\text{-Bu}_2bpy)_3]^{3+/2+}$ if regeneration is limiting performance. The IPCEs for $[Co(bpy)_3]^{3+/2+}$ and $[Co(Me_2bpy)_3]^{3+/2+}$, relative to $[Co(t\text{-Bu}_2bpy)_3]^{3+/2+}$, were found to remain relatively constant when the dye is changed to increase the regeneration driving force indicating that they are not regeneration limited. Significantly, however, $[Co(Me_2bpy)_3]^{3+/2+}$ and $[Co(t\text{-Bu}_2bpy)_3]^{3+/2+}$ displayed superior IPCEs compared to $I_3^{-1/2-}$ with $[Ru(bpy)_2(4,4'\text{-dicarboxy-bpy})](PF_6)_2$, which highlights the

drawbacks of the iodide electrolyte. A further test for regeneration limitations can be deduced from concentration dependencies studies. Increasing the concentration of the reduced form of the redox shuttle will increase the rate of regeneration. (12) Increasing the concentration of $[Co(bpy)_3]^{2+}$ two or even three fold did not affect the device performance, again indicating that regeneration is not a limiting step. (11)

Since regeneration was determined not to be a limiting step in the series of $[\text{Co}(R_2\text{bpy})_3]^{3+/2+}$ based DSSCs, we set out to quantify the role of recombination and to determine if the differences in performance could be attributed to recombination in DSSCs utilizing $[\text{Co}(R_2\text{bpy})_3]^{3+/2+}$ based electrolytes.(11, 13) DSSCs suffering from fast recombination will have a short electron diffusion length, L_n ; the average distance an injected electron can travel through the photoanode before a recombination event. A high charge collection efficiency requires the L_n to be greater than the film thickness, d.(14) The electron diffusion length is determined by competition between the charge transport time, τ_d , and the charge lifetime, τ_n , according to: $L_n = d(\tau_n/\tau_d)^{1/2}.(15-18)$ The charge lifetime and charge transport time may be derived from equivalent circuit analysis of the impedance spectra according to $\tau_n = R_{CT}C_\mu$ and $\tau_d = R_TC_\mu$. These measurements thus allow for the determination of the diffusion length of DSSCs employing outer-sphere redox shuttles as:

$$L_n = d(\tau_n / \tau_d)^{1/2} = d(R_{CT} / R_T)^{1/2}$$
(3.1)

EIS was thus used to investigate the electron dynamics in DSSCs employing outer-sphere redox shuttles using the equivalent circuit pioneered by Bisquert, shown in figure 2.7b, which has been shown to accurately describe the behavior of DSSCs in the dark. (19, 20)

3.2 Experimental

Photoanodes were prepared following procedure outlined in chapter 2, containing a 500 cycle TiO₂ blcking layer via ALD, a nanoparticle TiO₂ film, and a single Al₂O₃ layer via ALD. The resulting electrodes were allowed to cool after annealing to 100 °C before being added to a solution of 0.5 mM N3, [Ru(4,4'-dicarboxy-2,2'-bipyridine)2(NCS)2] (Dyesol, B4 dye) in ethanol. After 20-24 hours they were removed and rinsed briefly with acetonitrile. TiO₂ film thickness, *d*, was measured using a Dektak3 Surface Profiler to be 8 μm.

Sandwich DSSCs were fabricated by sandwiching a ~25µm thick Surlyn frame (Solaronix) between the photoanode and a platinized FTO electrode with light pressure applied at 140 °C to seal the cell. Electrical contact was achieved using copper wire and silver epoxy after scratching through the TiO₂ blocking layer with sand paper. Electrolyte was loaded through a hole in the counter electrode. Three-electrode measurements were made in a custom electrochemical cell. The photoanode was clamped over an opening in the cell and sealed with a viton o-ring. A AgNO₃/Ag reference electrode containing 0.1 M [(n-butyl)₄N](PF₆) supporting electrolyte in acetonitrile was prepared fresh each day, and was found to be +0.34 V vs. SCE, similar to accepted literature values.(21) The counter electrode consisted of a high surface area platinum mesh.

The three cobalt complexes employed in this study, cobalt(II) tris(4,4'-di-*tert*-butyl-2,2'-bipyridyl), [Co(*t*-Bu₂bpy)₃](PF₆)₂, cobalt(II) tris(4,4'-di-methyl-2,2'-bipyridyl), [Co(Me₂bpy)₃](PF₆)₂, and cobalt(II) tris(2,2'-bipyridyl), [Co(bpy)₃](PF₆)₂, were prepared following the procedure to prepare [Co(*t*-Bu₂bpy)₃](PF₆)₂ given in chapter 2. Elemental analysis calculated for [Co(bpy)₃](PF₆)₂: C, 44.06; H, 2.96; N, 10.28. Found: C, 43.97; H, 2.86; N, 10.30. Elemental analysis calculated for [Co(Me₂bpy)₃](PF₆)₂: C, 47.93; H, 4.03; N, 9.32. Found: C, 47.01; H, 4.03; N, 9.16.

All electrolytes contained 0.1 M LiClO₄, 0.2 M 4-*tert*-butylpyridine, tbp, and 0.22 M of a cobalt redox couple in acetonitrile. Sufficient NOBF₄ was added from a stock solution to each electrolyte to oxidize 20 mM of the cobalt unless otherwise stated. Photoanodes were aged before use by placing in a solution of 0.2 M tbp and 0.1 M LiClO₄ in acetonitrile overnight. Aging the electrodes allows for stable measurements free from time dependent effects observed in the first 12-18 hours after the electrode is placed in contact with the electrolyte.

Photoelectrochemical measurements were performed with a Gamry Reference 600 potentiostat interfaced with a Xe Arc Lamp. An AM 1.5 solar filter and neutral density filters were used to simulate sunlight at 100 mW cm⁻². EIS was performed in the dark with an Autolab PGSTAT 126N.

3.3 Results and Discussion

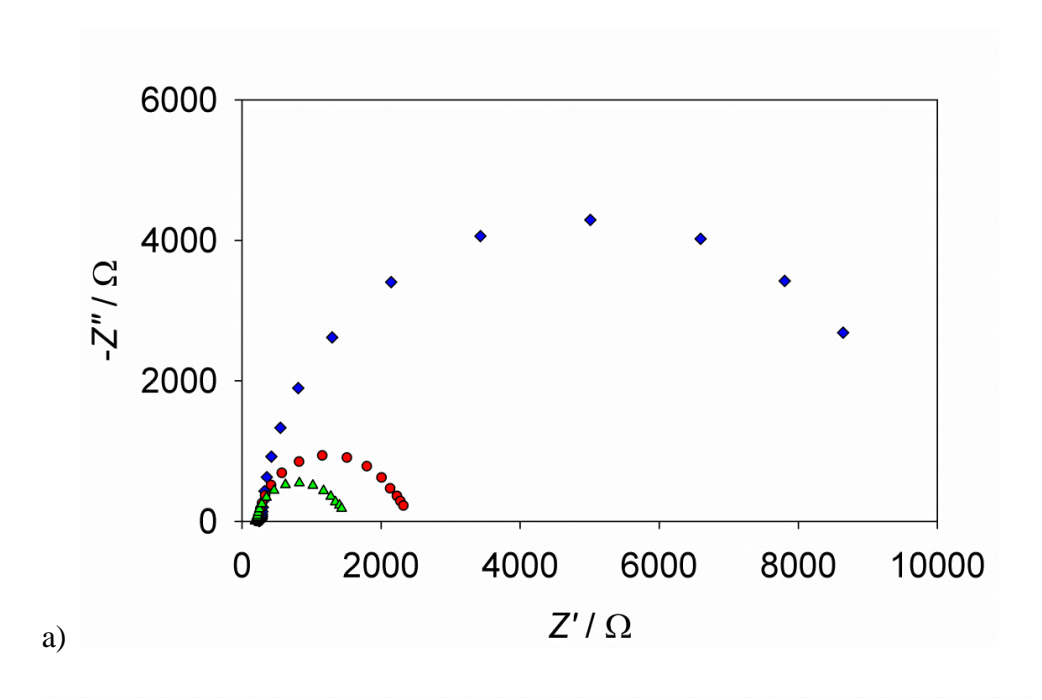
Impedance spectroscopy was used to investigate the electron dynamics in DSSCs employing cobalt bipyridyl redox shuttles. An important note needs to be made here regarding the time dependence of the working electrodes. The impedance spectra and corresponding photovoltaic measurements were observed to change over the first 12-18 hour period from when the electrode came into contact with the electrolyte solution; however were found to be stable afterwards. Specifically, R_T and R_{CT} were found to increase roughly by a factor of two and C_μ decreased slightly over this time period. These changes are all consistent with a positive shifting of the TiO_2 conduction band, which may be due to slow Li^+ intercalation; however the actual cause is speculative at this time. Consistent with our observations, changes in DSSC performance over time have been reported with iodide based electrolyte solutions containing additives such as Li^+ and $tip_{C}(22, 23)$ Any time dependence will obscure interpretation of the electron dynamics of interest, therefore the working electrodes were soaked for 18 hours in an

acetonitrile solution containing 0.1 M LiClO₄ and 0.2 M tbp immediately prior to use. After the soaking was completed the solution was replaced with the electrolytes described above. Since electrodes were to be used with multiple electrolyte solution, they were presoaked in a solution containing all additives except the redox shuttles in order to maintain a consistent age of the electrolyte before the measurements were taken. This presoak treatment effectively eliminated changes in both photovoltaic and impedance measurements over the eight hour testing period and was used in all measurements reported herein.

Impedance measurements using a three electrode DSSC were used to isolate the relevant processes to determine and compare the diffusion lengths of photoanodes in contact with different redox shuttles. A three-electrode cell with a high surface area platinum mesh counter electrode was used in order to eliminate impedance from the counter electrode, thus isolating the impedance of the photoanode and allowing measurement of charge transport as described in chapter 2. In addition to circumventing the counter electrode impedance, an advantage of employing a three-electrode configuration is the use of a constant reference electrode. The reference electrode allows for direct comparisons of the working electrode's interaction with multiple redox couples at the same electrode potential without any corrections or complications from changing solution potentials and overpotential drops at the counter electrode. Internal reference electrodes have been used in sandwich DSSCs, however, they reference solution potentials, which change dramatically between redox shuttles, not a constant potential. (24) Due to small variations between different individual electrodes, a single working electrode was used for each series of impedance measurements. All measurements were performed with several different electrodes, however, and the relative results (trends) were all comparable. Impedance parameters are potential dependant, thus impedance spectra were taken at potentials -0.6 to -0.8

V vs. Ag^+/Ag . This potential range was selected as the V_{oc} under AM 1.5 illumination for DSSCs containing any of the three redox shuttles falls within this range.

Figure 3.1a shows the impedance spectra obtained at constant potential (-0.750 V vs. Ag/AgNO₃) from one electrode in contact with three electrolyte solutions containing different cobalt redox shuttles: $\left[\text{Co}(t-\text{Bu}_2\text{bpy})_3\right]^{3+/2+}$, $\left[\text{Co}(\text{Me}_2\text{bpy})_3\right]^{3+/2+}$, and $\left[\text{Co}(\text{bpy})_3\right]^{3+/2+}$. The main semicircle feature results from the R_{CT} and C_{μ} elements with a smaller semicircle representing a smaller R_{CT} and thus faster recombination. Figure 3.1 (b) and (c) display plots of C_{μ} , R_T and R_{CT} derived from fitting the impedance spectra from a single electrode in contact with three electrolyte solutions containing the different cobalt redox shuttles to the equivalent circuit shown in figure 2.7a. Attempts to include I_3^-/I^- in this series of measurements were not successful since I and I₃ are able to migrate through the frit of the reference electrode and react with the silver reference electrode preventing consistent accurate measurements.(25) conduction band energy was constant during the duration of the measurements for all electrolytes as shown by the consistent C_{μ} and R_T values in figure 3.1b and 3.1c. All values of R_T are similar as expected since transport is a bulk property of the working electrode, which is the same for each of the three measurements, and independent of the contacting electrolyte (as long as the conduction band is constant). We point out here that it is actually the chemical diffusion coefficient, d_n , which is expected to be constant, whereas R_T and C_μ may vary somewhat between electrodes due to slightly different thicknesses or porosity. Since the chemical diffusion coefficient is described by $d_n = d^2/(R_T C_\mu)$, any difference in d between electrodes should produce an even larger difference in R_T and/or C_μ , for a constant d_n . Thus, a single working electrode was used for each series of impedance measurements to make comparisons as clear as possible and overcome any small variations between different individual electrodes.



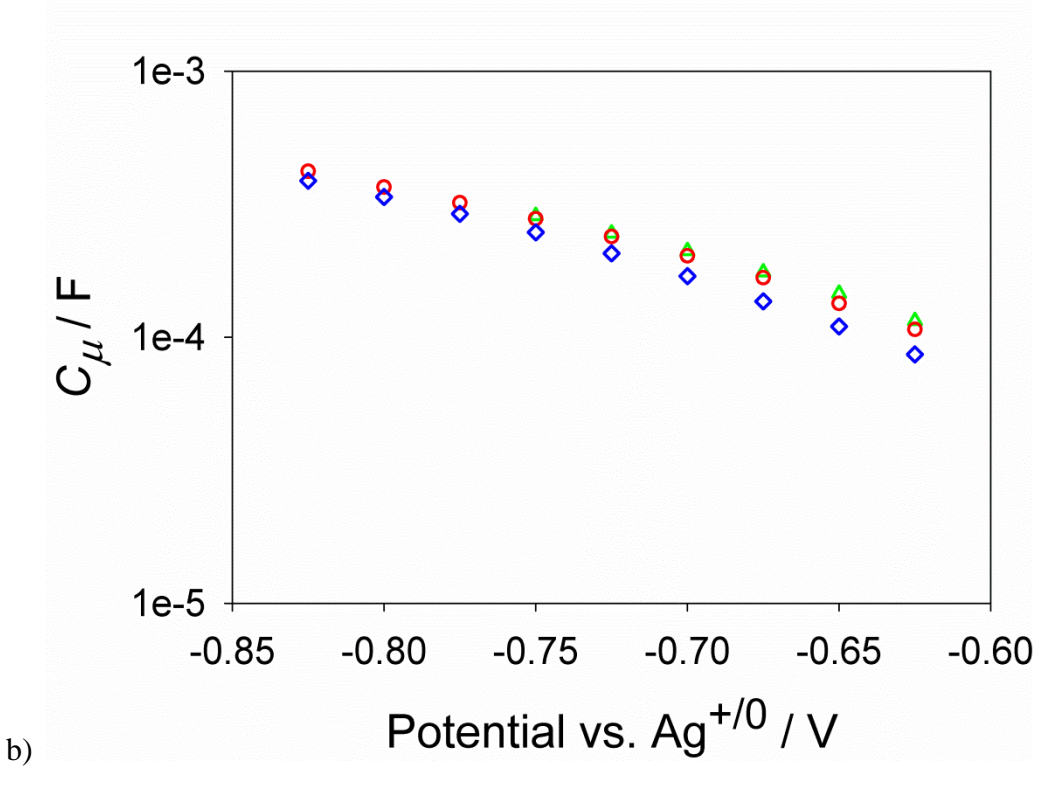
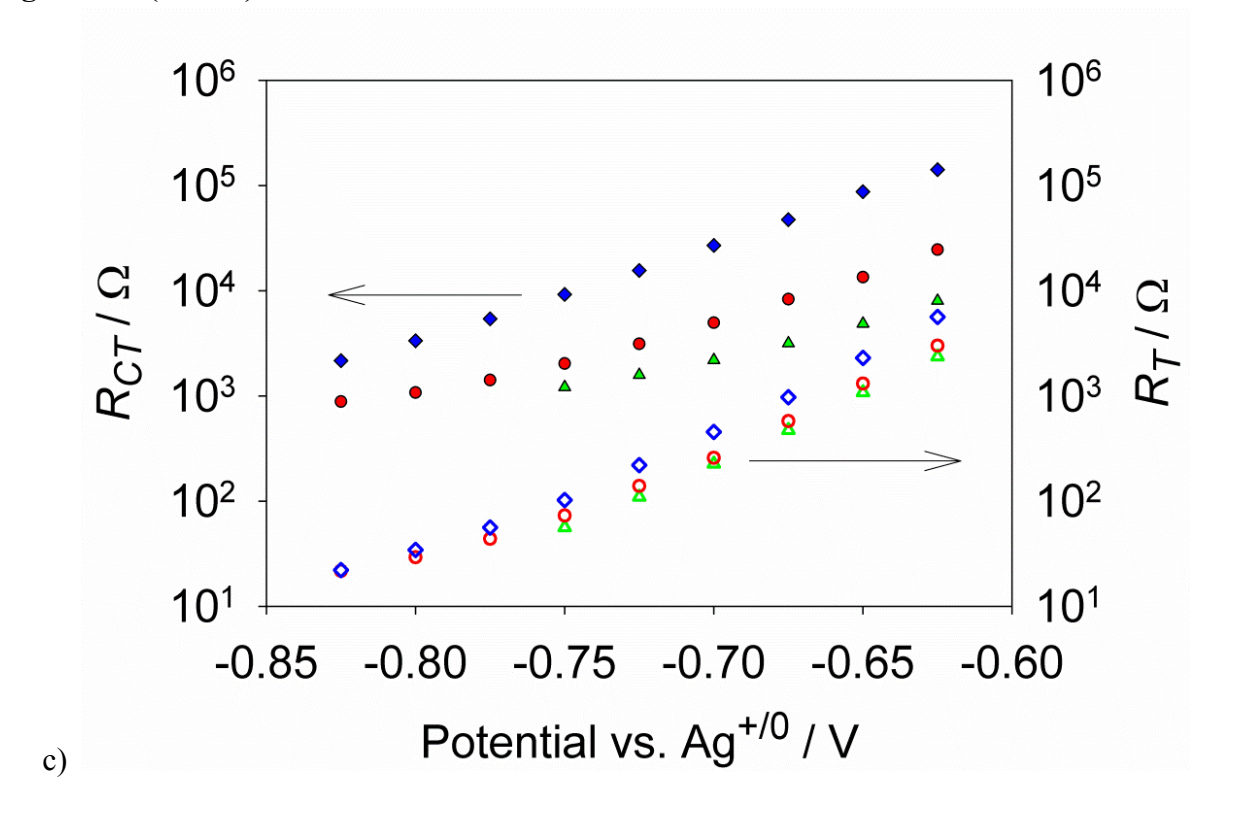
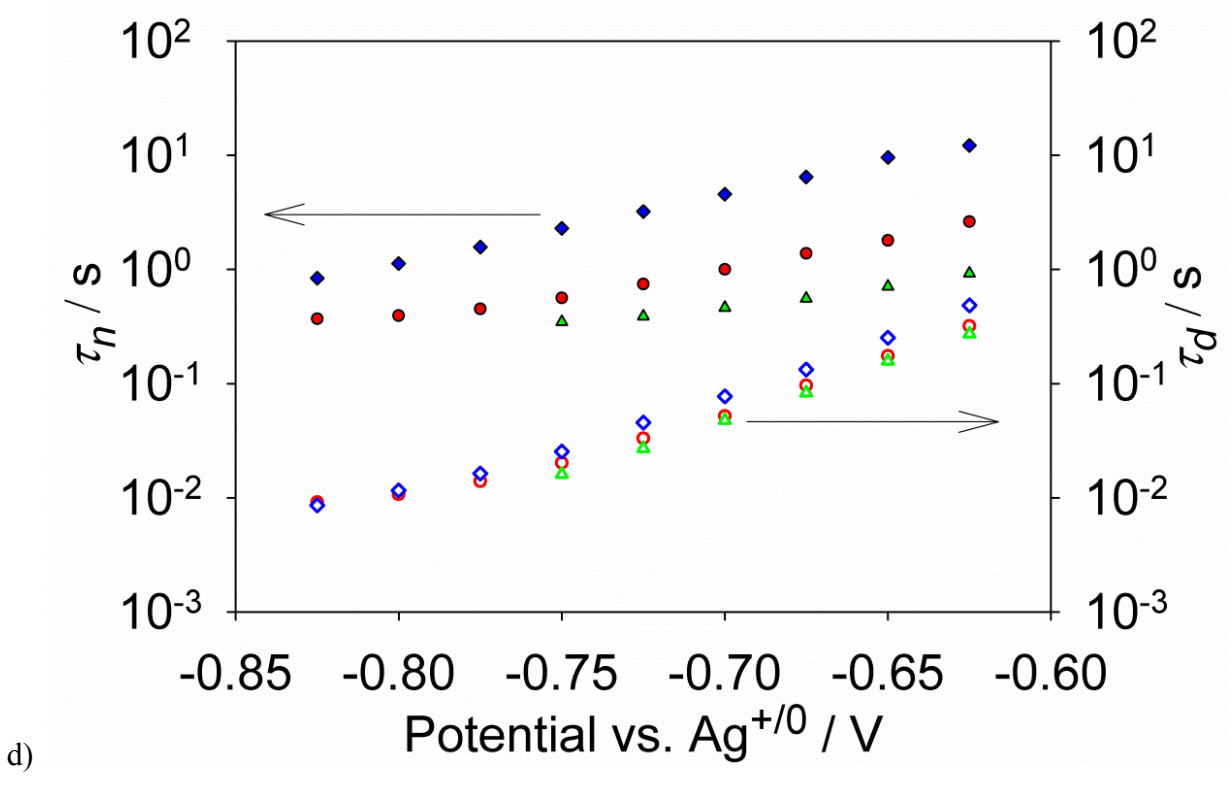


Figure 3.1. (a) Nyquist plots at -0.75 V vs. Ag^{+/0}, (b) capacitance, C_{μ} , (c) charge transfer resistance, R_{CT} , (filled symbols) and transport resistance, R_{T} , (hollow symbols) (d) electron lifetimes, τ_{n} , (filled symbols) and diffusion coefficient, d_{n} , (hollow symbols) of a single photoanode in contact with three separate redox shuttles: $\left[\text{Co}(t\text{-Bu}_{2}\text{bpy})_{3}\right]^{3+/2+}$ (blue diamond), $\left[\text{Co}(\text{Me}_{2}\text{bpy})_{3}\right]^{3+/2+}$ (Red circle), and $\left[\text{Co}(\text{bpy})_{3}\right]^{3+/2+}$ (green triangle).

Figure 3.1. (cont'd)





Both the diffusion coefficient and the electron lifetimes where calculated from the EIS results and are displayed in Figure 3.1d, which can be compared directly since the working electrodes were referenced to a fixed potential and the conduction band energy was constant. Application of a given potential produces a fixed electron concentration in the conduction band for all three redox shuttles, and the lifetimes are thus inversely proportional to the rate constant of electron transfer to the oxidized redox shuttle. The lifetimes reflect the same trend as R_{CT} , decreasing in the order $[Co(t-Bu_2bpy)_3]^{3+/2+} > [Co(Me_2bpy)_3]^{3+/2+} > [Co(bpy)_3]^{3+/2+}$ indicating the recombination rate constant increases in the opposite order, in excellent agreement with recently published results measuring the lifetimes with the open circuit voltage decay technique, but without relying on corrections for differences in solution potentials (the time dependence was also not accounted for in previous OCVD measurements).(11) The differences in formal potential of the redox shuttles follow the same trend, thus differences in driving force for recombination (the difference between the bottom of the conduction band and the formal potential of the redox shuttle) can partially account for the differences in lifetimes. This result is consistent with recombination in the Marcus normal region as expected for such large reorganization energy redox shuttles. Further, the relatively large difference in lifetimes between $[Co(t-Bu_2bpy)_3]^{3+/2+}$ and $[Co(Me_2bpy)_3]^{3+/2+}$, despite a small difference in formal potential, can be attributed to the increased bulk of the tert-butyl group compared to the methyl group. Lewis et al. have shown using analogous Osmium complexes that the insulating nature of the tert-butyl group relative to the methyl group can decrease electron transfer rates up to 100 fold by decreasing electronic coupling. (26)

Comparison of different τ_n , R_T , R_{CT} , or C_μ values for different electrodes or electrolytes can provide information regarding the physical characteristics in a DSSC as described above. It

is the separation of R_{CT} and R_T , however, which provides insight into the charge collection efficiency, η_{cc} , through the calculation of the effective diffusion length (Eq. 3.1). Since $[\text{Co}(t-\text{Bu}_2\text{bpy})_3]^{3+/2+}$ has the largest ratio of R_{CT} to R_T , it has the highest L_n and thus the highest collection efficiency of the three redox shuttles studied. The effective diffusion length must be calculated from R_{CT} and R_T measured at a constant quasi-Fermi level, which must be the case when R_{CT} and R_T are measured simultaneously.(16, 27) Correlation of L_n with applied potential is shown in figure 3.2a for all three cobalt redox shuttles studied. The charge collection efficiency increases with the ratio L_n/d , where $\eta_{cc} > 90\%$ requires $L_n > 2d$, and thus $R_{CT} > 4R_T.(14)$ In this study d was measured to be 8 μ m, thus both $[\text{Co}(t-\text{Bu}_2\text{bpy})_3]^{3+/2+}$ and $[\text{Co}(\text{Me}_2\text{bpy})_3]^{3+/2+}$ satisfy the $L_n > 2d$ condition for high η_{cc} over the entire potential range studied, but $[\text{Co}(\text{bpy})_3]^{3+/2+}$ only satisfied this condition at higher applied potentials. Similar dependence of L_n with potential as well as similar values of L_n/d measured by impedance and intensity modulated photocurrent and photovoltage spectroscopies have been reported for I_3^-/I^- with nanoparticle TiO2 in high-efficiency DSSCs.(28, 29)

Correlation of the calculated L_n values with the performance of DSSCs confirms recombination as the source of the observed discrepancy in performance. The photocurrent under 1 sun illumination has been demonstrated to be limited by the diffusion (mass transport) of the oxidized redox species, not the effective electron diffusion length.(30, 31) Therefore, steady-state current density, J, vs. applied potential, E, measurements were performed sunder low light intensities which should not be subject to mass transport effects to test the predictions of the impedance results. Figure 3.2b displays plots of the J-E curves for sandwich DSSCs under 10 mW cm⁻² illumination. Strikingly, the trend of the J-E curves matches the trend of effective

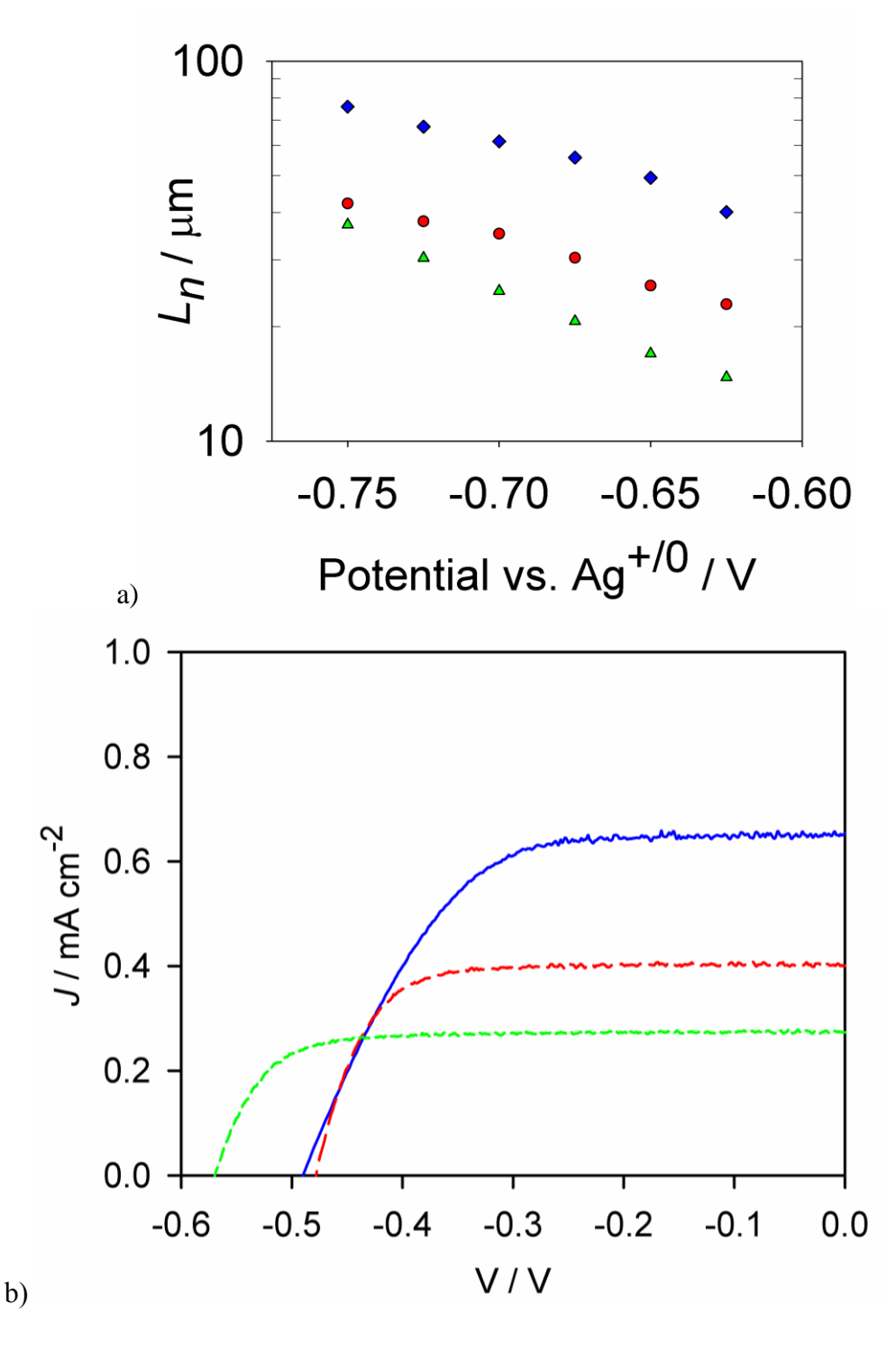


Figure 3.2. (a) Plots of calculated diffusion lengths, L_n , of a single photoanode in contact with three separate redox shuttles: $\left[\text{Co}(t\text{-Bu}_2\text{bpy})_3\right]^{3+/2+}$ (blue diamond), $\left[\text{Co}(\text{Me}_2\text{bpy})_3\right]^{3+/2+}$ (Red circle), and $\left[\text{Co}(\text{bpy})_3\right]^{3+/2+}$ (green triangle). (b) Current density vs. applied potential plots from DSSCs in contact with $\left[\text{Co}(t\text{-Bu}_2\text{bpy})_3\right]^{3+/2+}$ (blue solid), $\left[\text{Co}(\text{Me}_2\text{bpy})_3\right]^{3+/2+}$ (Red long dash), and $\left[\text{Co}(\text{bpy})_3\right]^{3+/2+}$ (green short dash) in response to 10 mW cm⁻² illumination.

diffusion lengths: $[\text{Co}(t-\text{Bu}_2\text{bpy})_3]^{3+/2+} > [\text{Co}(\text{Me}_2\text{bpy})_3]^{3+/2+} > [\text{Co}(\text{bpy})_3]^{3+/2+}$. These results are very similar to IPCE data reported previously (which are also not subject to mass transport limitations).(31) The J_{sc} of the DSSC employing $[\text{Co}(t-\text{Bu}_2\text{bpy})_3]^{3+/2+}$ is comparable to our I_3^-/I^- cell, which is consistent with a $L_n > 2d$. Our determinations of L_n from the impedance data indicate that there should not be a significant difference between J_{SC} 's of DSSCs employing $[\text{Co}(t-\text{Bu}_2\text{bpy})_3]^{3+/2+}$ and $[\text{Co}(\text{Me}_2\text{bpy})_3]^{3+/2+}$ since excellent charge collection is expected in both cases. There have been several reports in the literature recently using different techniques (both transient and steady state) to measure L_n which produce disparate values.(28, 32) Barnes *et al.* demonstrated that steady-state determination of L_n via analysis of IPCE data predicted 2-3 times lower values than dynamic techniques. Comparison of our impedance and J-E results are consistent with a slight overestimate of L_n by dynamic techniques. Importantly, however, the measured relative diffusion lengths are in excellent agreement with the photovoltaic behavior of DSSCs employing outer-sphere redox shuttles, and thus this dynamic EIS techniques offer a convenient way to screen new systems.

3.4 Conclusions

Electrochemical impedance spectroscopy is an excellent technique to probe relevant physical processes in DSSCs. Use of a three-electrode cell was found to be an ideal way to overcome the large charge-transfer resistance at the counter electrode thereby enabling EIS to measure charge transport and lifetimes of DSSCs containing outer-sphere redox shuttles. Further, use of an external reference electrode allows for accurate comparisons between redox shuttles with different solution potentials while maintaining a constant working electrode potential. This allowed for the determination of the diffusion length in DSSCs as a function of the contacting redox shuttle which agree with recombination being in the Marcus normal region

as expected for redox shuttles with large reorganization energies ($\lambda > 1.4$ eV). The relative diffusion lengths agree well with previously reported external quantum efficiencies, i.e. the redox shuttles with the longest diffusion lengths produced the highest external quantum efficiencies.(31) Although the overall photovoltaic performance of such cobalt complexes is limited by poor mass transport, this system offers an excellent model system for the investigations of DSSCs.(30) Finally, while $L_n > 2d$ is not the only criterion of a successful redox shuttle, it is a necessary condition, and EIS is an ideal technique to screen whether alternative redox shuttles are able to fulfill this condition.

REFERENCES

REFERENCES

- 1. B. A. Gregg, F. Pichot, S. Ferrere, C. L. Fields, *J. Phys. Chem. B* **105**, 1422 (Feb, 2001).
- 2. G. Oskam, B. V. Bergeron, G. J. Meyer, P. C. Searson, *J. Phys. Chem. B* **105**, 6867 (Jul, 2001).
- 3. T. W. Hamann, O. K. Farha, J. T. Hupp, *J. Phys. Chem. C* **112**, 19756 (Dec, 2008).
- 4. T. W. Hamann, R. A. Jensen, A. B. F. Martinson, H. Van Ryswyk, J. T. Hupp, *Energy Environ. Sci.* 1, 66 (2008).
- 5. T. W. Hamann, *Dalton Transactions* **41**, 3111 (2012).
- 6. S. A. Sapp, C. M. Elliott, C. Contado, S. Caramori, C. A. Bignozzi, *J. Am. Chem. Soc.* **124**, 11215 (Sep, 2002).
- 7. Y. Bai et al., J. Am. Chem. Soc. 133, 11442 (2011).
- 8. H. Nusbaumer, J. E. Moser, S. M. Zakeeruddin, M. K. Nazeeruddin, M. Gratzel, *J. Phys. Chem. B* **105**, 10461 (Nov, 2001).
- 9. S. M. Feldt et al., J. Am. Chem. Soc. 132, 16714 (Nov, 2010).
- 10. A. Yella et al., Science **334**, 629 (2011).
- 11. B. M. Klahr, T. W. Hamann, J. Phys. Chem. C 113, 14040 (2009).
- 12. G. Sauve et al., J. Phys. Chem. B 104, 6821 (Jul 27, 2000).
- 13. J. W. Ondersma, T. W. Hamann, J. Phys. Chem. C 114, 638 (2010).
- 14. J. Halme, G. Boschloo, A. Hagfeldt, P. Lund, *J. Phys. Chem. C* **112**, 5623 (2008).
- 15. A. J. Frank, N. Kopidakis, J. van de Lagemaat, *Coordination Chemistry Reviews* **248**, 1165 (Jul, 2004).
- 16. L. M. Peter, J. Phys. Chem. C 111, 6601 (May, 2007).
- 17. A. B. F. Martinson, T. W. Hamann, M. J. Pellin, J. T. Hupp, *Chem. Eur. J.* **14**, 4458 (2008).
- 18. A. N. M. Green, E. Palomares, S. A. Haque, J. M. Kroon, J. R. Durrant, *Journal of Physical Chemistry B* **109**, 12525 (Jun, 2005).

- 19. J. Bisquert, *Phys. Chem. Chem. Phys* **2**, 4185 (2000).
- 20. F. Fabregat-Santiago, J. Bisquert, G. Garcia-Belmonte, G. Boschloo, A. Hagfeldt, *Sol. Energy Mat. Sol. Cells* **87**, 117 (2005).
- 21. C. K. Mann, K. K. Barnes, *Electrochemical reactions in nonaqueous systems*. (Marcel Dekker Inc., New York, 1970).
- 22. K. D. Benkstein, N. Kopidakis, J. van de Lagemaat, A. J. Frank, *J. Phys. Chem. B* **107**, 7759 (2003).
- 23. S. Nakade, T. Kanzaki, S. Kambe, Y. Wada, S. Yanagida, *Langmuir* **21**, 11414 (2005).
- 24. A. Zaban, J. Zhang, Y. Diamant, O. Melemed, J. Bisquert, *J. Phys. Chem. B* **107**, 6022 (2003).
- 25. S. Standridge, G. C. Schatz, J. T. Hupp, *Langmuir* **25**, 2596 (2009).
- 26. T. W. Hamann, B. S. Brunschwig, N. S. Lewis, *J. Phys. Chem. B* **110**, 25514 (Dec, 2006).
- 27. J. Bisquert, V. S. Vikhrenko, *J. Phys. Chem. B* **108**, 2313 (Feb, 2004).
- 28. P. R. F. Barnes, A. Y. Anderson, S. E. Koops, J. R. Durrant, B. C. O'Regan, *J. Phys. Chem. C* **113**, 1126 (Jan, 2009).
- 29. Q. Wang et al., J. Phys. Chem. B 110, 25210 (Dec, 2006).
- 30. J. J. Nelson, T. J. Amick, C. M. Elliott, J. Phys. Chem. C 112, 18255 (Nov. 2008).
- 31. B. M. Klahr, T. W. Hamann, J. Phys. Chem. C 113, 14040 (Aug. 2009).
- 32. H. K. Dunn, L. M. Peter, *Journal of Physical Chemistry C* 113, 4726 (Mar, 2009).

Chapter 4: Modeling DSSC Performance to Predict a Route Towards Higher Efficiency

In order to rationally design new components for DSSCs we must first have a diagnostic method to predict the efficiency of a DSSC based on the characteristics of its components. This chapter outlines a model to approximate the efficiency of a DSSC based on the characteristics of a theoretical outer-sphere redox shuttle used as the electrolyte, assuming that the other components of the DSSC are optimized around the redox shuttle as discussed below.

The power conversion efficiency, η , of DSSCs is the ratio of the maximum power output, P_{max} , of the cell to the power of the incident light, P_{in} . The maximum power that can be produced is best separated into the useful diagnostic terms: short circuit photo-current density, J_{sc} , open circuit voltage, V_{oc} , and fill factor, ff, as expressed by equation 4.1.

$$\%\eta = \frac{P_{max}}{P_{in}} = \frac{J_{sc}V_{oc}ff}{P_{in}}$$
 4.1

The J_{SC} results from the absorption cross-section of the dye as well as efficient charge separation and collection, resulting from the balance of the electron transfer rates for the processes depicted in figure 1.1.(1) The open circuit potential, V_{OC} , is determined by the difference between the Nernstian potential of the redox couple in solution, E_{redox} , and the quasi-Fermi level, E_F/q , of the semiconductor when the photocurrent is exactly offset by recombination, resulting in no net current.(1) The fill factor is a diagnostically helpful term that has been introduced as the ratio of $P_{max}/J_{SC}*V_{OC}$. The FF in high efficiency solar cells is typically between the values of 0.7 and 0.75.

Following equation 4.1 the efficiency of a DSSC can be predicted by calculating J_{sc} , V_{oc} , and the fill factor, FF. For simplicity, we assume that a DSSC optimized for a particular redox-shuttle will have a reasonably good FF of 0.73. The current density can be calculated using

$$J_{sc} = \eta_{regen} \eta_{inj} \eta_{cc} \int_{400}^{Abs} \Phi(\lambda) \eta_{lhe}(\lambda) d\lambda$$
 4.2

where η_{regen} is the regeneration efficiency, η_{inj} is the electron injection efficiency, η_{cc} is the charge collection efficiency of electrons that are injected into the TiO₂, Φ is the incident light intensity, and η_{lhe} is the light harvesting efficiency.

The η_{lhe} is dependent on the dye absorption spectrum and dye loading on the TiO₂ film. However, in the calculation presented herein we will maintain a constant η_{lhe} and vary the effective absorption spectrum of the dye by modifying the limits of integration of equation 4.2. The integral allows for the calculation of the number of photons absorbed by integrating the AM1.5 solar spectrum from 400 nm to Abs, the absorption onset of the dye being used. For the calculations shown here the absorption onset of the dye will change with the mediator used such that there is always a 200 mV driving force for dye regeneration (E_{regen} in figure 1.1) i.e. $E^{\circ} = E_{redox} - 200$ mV; this value approximates the minimum driving force needed to produce quantitative regeneration, $\eta_{regen} \approx 1$; this value is similar to the 230 mV reported by Yum et al. for a cobalt shuttle with the organic dye Y123 which demonstrated excellent performance.(2) The actual value for the necessary driving force for quantitative regeneration will depend on reorganization energy of the redox shuttle and the dye and is discussed briefly below.

The η_{inj} is a property of the dye dependant on the electronic coupling between the dye and TiO₂ as well as the energy of the dyes LUMO and electron accepting states in TiO₂. For the

calculations presented here the dye LUMO will be constant at 100 mV above the conduction band minimum for TiO_2 . η_{inj} for the calculations here will be assumed to be 0.9, an optimized but reasonable figure.(3)

The L_n for DSSCs utilizing $[\text{Co}(t-\text{Bu}_2\text{bpy})_3]^{3+/2+}$ has been demonstrated to be greater than twice the thickness of the typical TiO_2 electrode used with a blocking layer of Al_2O_3 , therefore, a η_{cc} of one for the $[\text{Co}(t-\text{Bu}_2\text{bpy})_3]^{3+/2+}$ system is assumed.(4, 5) Now calculations of η_{cc} , and thus J_{sc} , can be made using $[\text{Co}(t-\text{Bu}_2\text{bpy})_3]^{3+/2+}$ as a reference since redox couples with slightly faster recombination such as $[\text{Co}(\text{Me}_2\text{bpy})_3]^{3+/2+}$ do not have a η_{cc} of one.(6) The charge collection efficiency is proportional to L_n which is inversely proportional to the rate constant of electron transfer from the semiconductor to the oxidized form of the redox shuttle, k_{et} . Combining this relationship with the equation for k_{et} provided by Marcus theory:(7, 8)

$$k_{et} = k_{et,\text{max}} \exp \left[\frac{-(\Delta G + \lambda)^2}{4\lambda k_B T} \right]$$
 4.3

 η_{cc} for any outer-sphere redox shuttle, with reference to $\left[\text{Co}(t\text{-Bu}_2\text{bpy})_3\right]^{3+/2+}$, can be calculated according to:

$$\frac{\eta_{cc,M}}{\eta_{cc,Co}} = \frac{L_{n,M}}{L_{n,Co}} = \frac{k_{et,Co}}{k_{et,M}} = \exp\left[\frac{-\left(\Delta G_{Co} + \lambda_{Co}\right)^2}{4\lambda_{Co}k_BT} - \frac{-\left(\Delta G_{M} + \lambda_{M}\right)^2}{4\lambda_{M}k_BT}\right]$$

$$4.4$$

where $-\Delta G = \mathbf{E_{cb}} - qE_{redox}$ is the driving force of electron transfer from TiO₂ to the oxidized redox shuttle, λ is the reorganization energy, and the subscripts Co and M represent values for $[\text{Co}(t\text{-Bu}_2\text{bpy})_3]^{3+/2+}$ ($\lambda_{\text{Co}} = 1.4 \text{ eV})(9)$ and the theoretical redox shuttle in question respectively. V_{oc} , which is the difference between the Fermi level, \mathbf{E}_{F} , at open circuit in the TiO₂ and the redox potential of the redox shuttle, can be calculated in a similar manner. For

recombination that is first order in free electron concentration the quasi-Fermi level at open circuit ideally varies 59 mV per decade change in k_{et} .(10) The V_{oc} can then be calculated by

$$V_{oc} = \left[E_{F,Co} + 0.059 \times \log \left(\frac{k_{et,Co}}{k_{et,M}} \right) \right] - E_{redox,M}$$
 4.5

where the ratio of the k_{et} 's is defined in equation 4.4. Placing equations 4.2-4.5 into equation 4.1 allows for the calculation of a DSSC's efficiency with only two variables, the redox potential and the reorganization energy of the mediator.

The resulting efficiency predictions are shown in figure 4.1. The rise on the right side of the plot is where the three cobalt mediators discussed above fall. Predicting that these mediators are capable of producing efficiencies in the 10-15% range agrees with performance demonstrated in laboratories.(11, 12) The large depression found for mediators with intermediate redox potentials and reorganization energies results from very fast electron transfer rates when $-\Delta G \approx \lambda$. This prediction agrees with literature reports where a DSSC using ferrocene/ferrocenium, a mediator which is located near the center of figure 4.1, showed poor photovoltaic effect due to very fast recombination.(13) The interesting prediction made in figure 4.1 is the rise on the left side of the plot where efficiencies rise above 20%. These high efficiencies are predicted to be obtainable using redox shuttles which are in the Marcus inverted region for electron recombination, i.e. mediators with low λ and more positive redox potentials. This results in improvement in V_{oc} through decreasing the solution potential and increasing the Fermi level, while maintaining excellent charge collection efficiency.

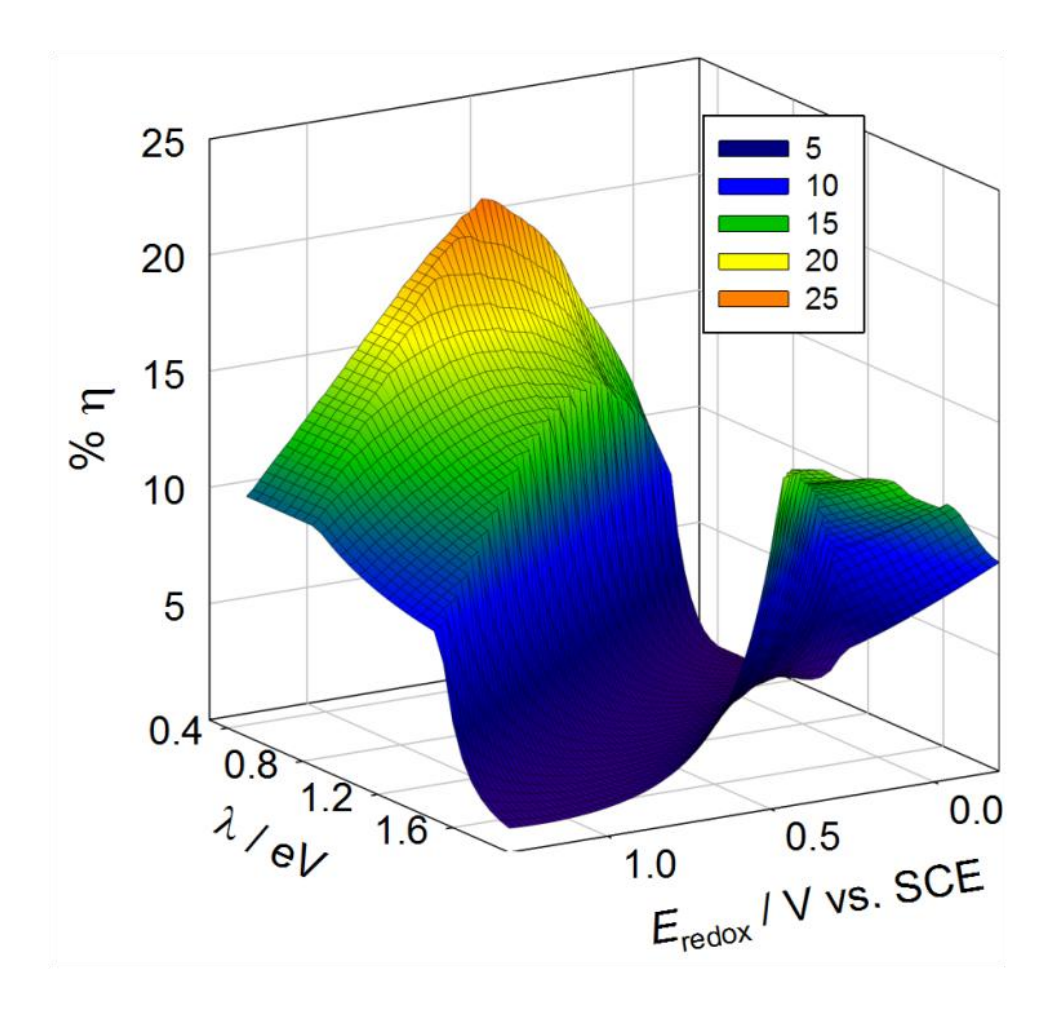


Figure 4.1. Calculated η as a function of E_{redox} and λ of the mediator in recombination limited DSSCs.

As stated above the above calculation assumes a low driving force is adequate for efficient regeneration. In reality the driving force, $-\Delta G$, necessary for quantitative regeneration will also depend on λ according to equation 3 and the Marcus cross-relation for the rate constant of regeneration, k_{regen} , (14)

$$k_{regen} = \sqrt{k_{D^+/D}k_{R^+/R}K_{DR}}$$
 4.6

where $k_{D+/D}$ and $k_{R+/R}$ are the self-exchange rate constants for the dye and redox shuttle, respectively, and K_{DR} is the equilibrium constant of the electron transfer reaction. For a fixed

 $-\Delta G$, k_{regen} will increase as λ decreases provided electron transfer is in the Marcus normal region, i.e. $-\Delta G < \lambda$. This prediction has been confirmed in a study comparing dye regeneration of N719 with $[\text{Co}(t-\text{Bu}_2\text{bpy})_3]^{3+/2+}$, having a very small self-exchange rate, and ferrocene/ferrocenium, having a fast self-exchange rate.(15) In this study Cazzanti *et al.* found that ferrocene regenerated N719 exceptionally fast when compared to $[\text{Co}(t-\text{Bu}_2\text{bpy})_3]^{3+/2+}$ despite ferrocene having a smaller driving force for regeneration.(15) Considering the effect of λ on η_{regen} in the above calculation will decrease the overall % η for redox shuttles with large λ . Additionally these calculations do not consider effects of decreased electronic coupling between the semiconductor and electron acceptor due to blocking layers or bulky dyes which could alter the predictions. Nevertheless, these calculations clearly indicate that shuttles with low reorganization energies and more positive potentials should prove interesting to study.

REFERENCES

REFERENCES

- 1. T. W. Hamann, J. W. Ondersma, Energy Environ. Sci. 4, 370 (2011).
- 2. R. E. Smalley, MRS Bulletin **30**, 412 (2005).
- 3. S. E. Koops, B. C. O'Regan, P. R. F. Barnes, J. R. Durrant, *J. Am. Chem. Soc.* **131**, 4808 (Apr, 2009).
- 4. J. W. Ondersma, T. W. Hamann, J. Phys. Chem. C 114, 638 (2010).
- 5. J. Halme, G. Boschloo, A. Hagfeldt, P. Lund, J. Phys. Chem. C 112, 5623 (2008).
- 6. B. M. Klahr, T. W. Hamann, J. Phys. Chem. C 113, 14040 (2009).
- 7. T. W. Hamann, F. Gstrein, B. S. Brunschwig, N. S. Lewis, *J. Am. Chem. Soc.* **127**, 7815 (Jun 1, 2005).
- 8. T. W. Hamann, F. Gstrein, B. S. Brunschwig, N. S. Lewis, *J. Am. Chem. Soc.* **127**, 13949 (Oct 12, 2005).
- 9. J. W. Ondersma, T. W. Hamann, J. Am. Chem. Soc. 133, 8264 (2011).
- 10. L. M. Peter, *J. Phys. Chem. C* **111**, 6601 (May, 2007).
- 11. A. Yella et al., Science **334**, 629 (2011).
- 12. H. N. Tsao et al., Energy and Environ. Sci. 4, 4921 (2011).
- 13. B. A. Gregg, F. Pichot, S. Ferrere, C. L. Fields, *J. Phys. Chem. B* **105**, 1422 (Feb, 2001).
- 14. R. A. Marcus, Ann. Rev. Phys. Chem. 15, 155 (1964).
- 15. S. Cazzanti, S. Caramori, R. Argazzi, C. M. Elliott, C. A. Bignozzi, *J. Am. Chem. Soc.* **128**, 9996 (Aug, 2006).

Chapter 5: Measurements and Modeling of Electron Transfer from Nanoparticle TiO₂ Electrodes to Outer-Sphere Redox Shuttles

5.1 Introduction

Since the largest energy loss mechanism in state-of-the-art DSSCs is the overpotential required for efficient dye regeneration by iodide, one strategy to significantly improve the efficiency is to replace I_3^-/I^- with a redox shuttle with a more positive potential. (1) The detriment of pursuing this strategy results from the increasing rate of recombination of photoinjected electrons from TiO2 to the oxidized form of the redox shuttle.(1-4) Development of alternative redox shuttles which are not hampered by fast recombination should be facilitated by a detailed understanding of this reaction. Several important details of the recombination mechanism are still not established, however, which is largely due to continued reliance on I₃/I as the redox shuttle.(5) An analysis of several proposed recombination mechanisms to I_3^-/I^- has An interesting ongoing discussion involving recently been presented elsewhere.(6) recombination is the extent to which surface states participate. Since the environment of surface atoms of the TiO2 film is inherently unique from those in the bulk, there will be localized electronic states on the surface. If these states are energetically located between the redox level of the redox shuttle in the electrolyte and the conduction band energy it is possible that they participate in recombination. In order to understand recombination, the role of surface states must be understood.

The predictions provided by the model described in chapter 4 require that recombination from the conduction band is the dominant recombination mechanism. Prior work examining

back electron transfer to oxidized dyes indicated Marcus inverted region behavior, suggesting recombination mainly originates from the conduction band.(7, 8) If this result holds for recombination to redox shuttles, a path to achieve high efficiency DSSCs is clear. There has been an ongoing discussion for several years as to the extent that sub-band gap trap states, or surface states, participate in facilitating recombination.(9-13) Since these states can occur in the energy range between the redox potential of the mediator and the conduction band edge they could theoretically participate in recombination. Thus, an important experimental question remained to be answered regarding whether recombination in the Marcus inverted region can be experimentally observed with outer-sphere redox shuttles and exploited in DSSCs.

A central measurement used to discuss recombination is the electron lifetime, or the average time an excited electron resides, or "lives", in the TiO₂ anode before transferring to the electrolyte. The lifetime has been measured in porous thin films for DSSCs by a variety of methods such as open circuit voltage decay, intensity modulated photovoltage spectroscopy, and electrochemical impedance spectroscopy, EIS.(10, 14, 15) Electron lifetimes have been well established to have an exponential dependence on potential which has been explained using the multiple trapping model.(15-17) This exponential dependence has been explained based on electronic processes happening prior to electron transfer to the redox shuttle. The multiple trapping model considers that TiO₂ contains a large number of electron traps and a low number of free electrons. Thus before a recombination event may occur an electron must become excited from a trap state into the conduction band before traveling to the surface of the nanoparticle. The lifetime therefore increases as the ratio of trapped to free electrons increases, which changes exponentially as the Fermi level moves through the band gap.(15, 16) This exponential

dependence holds true only when recombination is occurring primarily from the conduction band. A theoretical model for the participation of surface states in recombination further predicted a parabolic component in the electron lifetime. (10, 18) Prior reports of surface state mediated recombination have presented indirect evidence at best, however. For example, when an aqueous polysulfide electrolyte was used in a quantum dot sensitized solar cell a deviation of the exponential dependence of the lifetime indicated surface state mediated recombination. (10, 19) These prior reports utilized, such as I_3^-/I^- and polysulfide electrolytes, which greatly complicate the analysis of electron transfer. (10, 19)

A better picture of recombination kinetics from TiO_2 can be established by eliminating the complicated electrochemistry of the inner-sphere multiple electron redox shuttles. For example using a simple outer-sphere redox shuttle ensures that a single one-electron acceptor species is in solution.(5) Further, use of such redox shuttles offers the ability to tune the physical parameters, such as redox potential and reorganization energy, allowing systematic studies that are not possible with T_3 . Recently, a series of cobalt bipyridyl redox shuttles were used to investigate the bottlenecks which can limit the efficiency of outer-sphere redox shuttles in DSSCs.(11, 20) Based on these results, it was concluded that surface states do not appear to play a role in recombination.(11) It stands to reason that in order for recombination from surface state to be observable it must be of the same magnitude or faster than recombination from the conduction band. In this chapter, recombination is probed using redox shuttles with immensely different redox potentials and reorganization energies. A model based on Marcus theory to describe recombination, considering contributions from both conduction band and surface states

is then developed. The combined experimental and modeling results allow us to clearly identify each separate element of recombination.

5.2 Experimental

All working electrodes utilized either a TiO₂ or poly-phenyl oxide, PPO, blocking layer to prevent complications associated with electron transfer from the substrate (i.e. shunting) and ensure the measured recombination was strictly from the nanoparticle film.(2, 20, 21) A detailed comparison of the different blocking layers is presented in chapter 2. Nanoparticle TiO₂ electrodes utilizing a dense blocking layers of TiO₂ were prepared as described in chapter 2, with the exception of using Ti-Nanoxide T20 paste (Solaronix). The TiO2 film thickness, d, was measured using a Dektak3 Surface Profiler to be 8 µm. For electrodes utilizing a poly-phenol oxide (PPO) blocking layer, the PPO was selectively polymerized onto the bare FTO after the nanoparticle TiO2 film was deposited onto FTO and annealed. Electropolymerization was carried out following the reported procedure of Gregg et al.(2) Briefly, the electrodes were submerged in a solution of 60 mM phenol, 90 mM 2-allylphenol, 100 mM LiClO₄ in a 10/10/1 water/ethanol/2-butoxyethanol solvent mixture adjusted to pH 9 by addition of 10 mM tetrabutylammonium hydroxide in methanol. The potential of the electrodes was then scanned from 0 to 1.5 V vs. SCE at a rate of 100 mV/s for 60-80 cycles. The electrodes where then soaked in 10 mM tetrabutylammonium hydroxide in methanol to remove unreacted monomers and oligomers, rinsed with ethanol, and cured in air at 150 °C for 30 min. The electropolymerization process is self-limiting and deposits only on the conductive FTO substrate since the TiO₂ is insulating at the potentials used. Sandwich DSSCs were fabricated according to a procedure described in chapter 2. Three-electrode measurements were made in a custom electrochemical cell.(11) The photoanode was clamped over an opening in the cell and sealed with a viton o-ring. A commercial Ag/AgCl reference electrode (ESA 66-EE009 "No Leak") was used for all three-electrode measurements. The counter electrode consisted of high surface area platinum mesh.

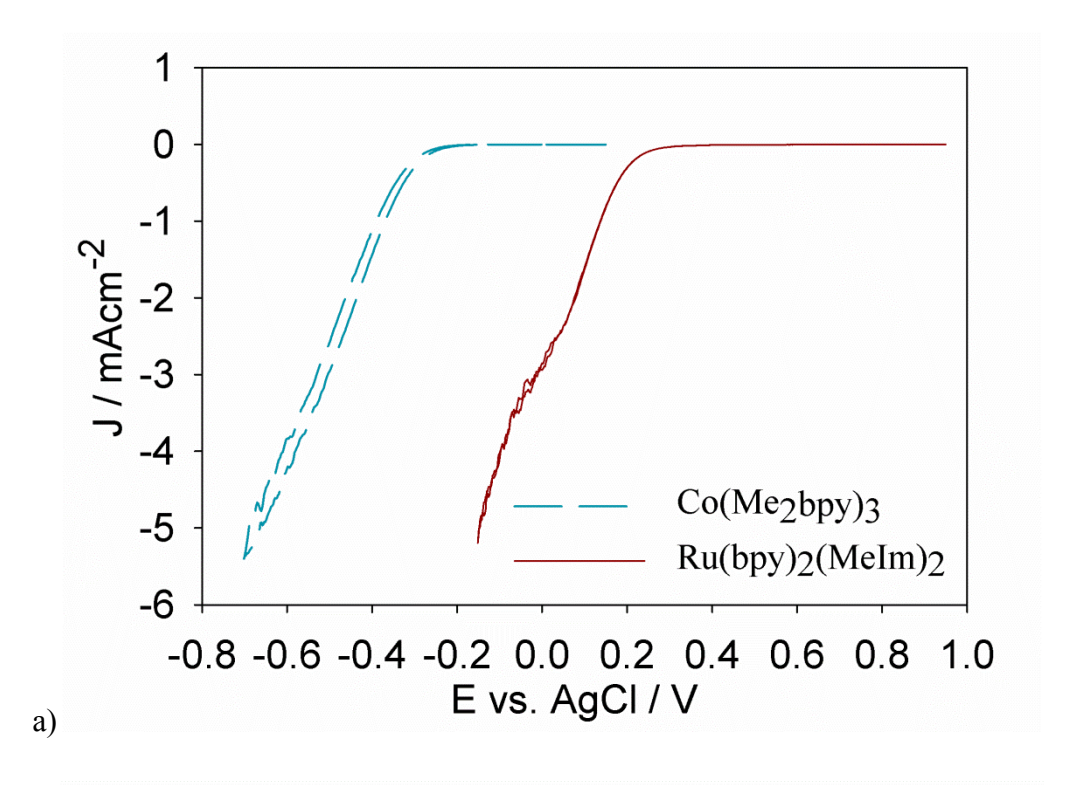
Ruthenium(II) bis(2,2'-bipyridyl)-bis(N-methylimidozole) hexafluorophosphate, [Ru(bpy)₂(MeIm)₂](PF₆)₂ was prepared as described in chapter 2. The cobalt outer-sphere redox couple employed in this study, cobalt(II) tris(4,4'-di-methyl-2,2'-bipyridyl) hexafluorophosphate, [Co(Me₂bpy)₃](PF₆)₂ was prepared as described in chapter 3. All electrolytes contained 0.1 M LiClO₄, and 40 M of either [Co(Me₂bpy)₃](PF₆)₂ or [Ru(bpy)₂(MeIm)₂](PF₆)₂ in acetonitrile. Sufficient NOBF₄ was added from a stock solution to each electrolyte to oxidize 20 mM of the redox shuttle unless otherwise stated. Photoanodes were aged before use by placing in a solution of 0.1 M LiClO₄ in acetonitrile overnight. Opencircuit voltage decay measurements were performed by monitoring the voltage vs. time response when the cell is switched to open-circuit conditions from a potentiostatically controlled applied potential on the TiO₂ electrode. All electrochemical measurements were performed in the dark with an Autolab PGSTAT 126N.

5.3 Measurements

Current density vs. applied potential, J-E, measurements were performed for DSSCs employing $[Co(Me_2bpy)_3]^{3+/2+}$ and $[Ru(bpy)_2(MeIm)_2]^{3+/2+}$ redox shuttles in the dark. Figure 5.1a shows representative J-E plots using a single TiO_2 nanoparticle electrode in contact with both electrolytes. For reference, the formal potentials of $[Co(Me_2bpy)_3]^{3+/2+}$ and $[Ru(bpy)_2(MeIm)_2]^{3+/2+}$ were measured to be 0.08 V and 0.89 V vs. Ag/AgCl, respectively.

The dark *J-E* curve for $[Co(Me_2bpy)_3]^{3+/2+}$ is characteristic for a DSSC utilizing cobalt-based redox shuttles. (11, 20, 22-26) The dark current density at more negative potentials deviated from the expected exponential dependence due to the increasing diffusion resistance of the electrolyte. (5) Substantially larger dark current density was found at a given potential when $[Ru(bpy)_2(MeIm)_2]^{3+/2+}$ was employed as the redox shuttle. Since the dark current density is a measure of recombination, this indicates that at a single potential recombination is much faster to $[Ru(bpy)_2(MeIm)_2]^{3+/2+}$ compared to $[Co(Me_2bpy)_3]^{3+/2+}$. (2, 4, 27)

Another way to compare rates of recombination is through determinations of the lifetimes, τ_n .(5, 10, 11, 20) Lifetimes of DSSCs employing $[\text{Co}(\text{Me}_2\text{bpy})_3]^{3+/2+}$ and $[\text{Ru}(\text{bpy})_2(\text{MeIm})_2]^{3+/2+}$ were measured using the open-circuit voltage decay technique displayed in figure 5.1b.(16, 28)



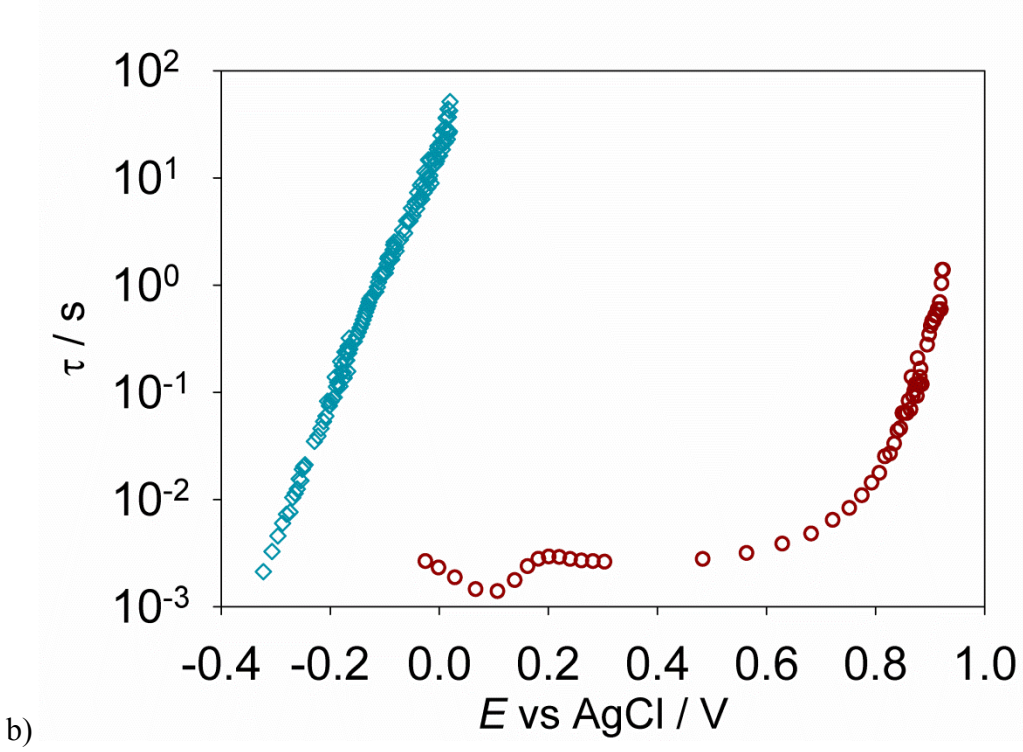


Figure 5.1. a) Current density vs. applied potential curves and b) lifetimes vs. potential plots for DSSCs utilizing $[Co(Me_2bpy)_3]^{3+/2+}$ (blue, dash line/diamonds) and $[Ru(bpy)_2(MeIm)_2]^{3+/2+}$ (red, solid line/circles) redox shuttles.

Since the open-circuit voltage decay measurement is made at open circuit, and represents the average time a free electron survives before recombining, the results do not depend on any variation of the quasi-Fermi level, \mathbf{E}_{F} in the film, whereas the Fermi level may not be completely constant in the dark current density measurements as discussed in chapter 2.(29) The open circuit voltage, V_{oc} , decay can be transformed into the lifetime by:(16)

$$\tau_n = -\frac{k_{\rm B}T}{q} \left(\frac{dV_{oc}}{dt}\right)^{-1}$$
 5.1

were $k_{\rm B}$ is the Boltzmann constant, T is temperature, q is the elementary charge and t is time. As displayed in figure 5.1b, the lifetime for the cell with $[{\rm Co(Me_2bpy)_3}]^{3+/2+}$ shows the typical semi-logarithmic dependence on potential. Strikingly, however, the lifetime for the $[{\rm Ru(bpy)_2(MeIm)_2}]^{3+/2+}$ couple is highly non-linear, and appears parabolic at positive potentials. The concentration of $[{\rm Ru(bpy)_2(MeIm)_2}]^{3+}$ was varied by a factor of three and the lifetime shifted proportionally, however the shape did not change. Larger concentrations were not possible due to limited solubility, and lower concentrations resulted in concentration polarization effects. Nevertheless, the concentration dependence of the lifetime demonstrates that recombination is first order in acceptor species.

Bisquert has suggested that recombination from surface states should lead to such a parabolic shape of the lifetime. (18) To the best of our knowledge, however, such a parabolic lifetime has not been observed experimentally when care is taken to passivate the back FTO electrode. (21) The vast majority of research reports on DSSCs have relied on the I_3^-/I^- redox shuttle which may preclude observation of such parabolic lifetimes due to the particularly complicated electrochemistry of this couple. (5, 30) Use of outer-sphere redox shuttles, however,

allows for substantial variations in recombination rates and should additionally be more straightforward to interpret.(5) Below a model to quantitatively describe recombination to these outer-sphere redox shuttles is developed.

5.4 Modeling

The lifetime of electrons in the TiO_2 can be expressed as the ratio of the concentration of electrons, n, at a given quasi-Fermi level, \mathbf{E}_F , to the rate at which they are being lost, which in the dark is simply the recombination rate, U, at \mathbf{E}_F . Defining values for both $n(\mathbf{E}_F)$ and $U(\mathbf{E}_F)$ therefore allows for the use of the following equation to calculate the lifetime(10):

$$\tau_n(\mathbf{E}_{\mathrm{F}}) = \frac{\partial n(\mathbf{E}_{\mathrm{F}}) / \partial \mathbf{E}}{\partial U(\mathbf{E}_{\mathrm{F}}) / \partial \mathbf{E}}$$
5.2

5.4.1 Electron concentration

The concentration of electrons may be broken down into free electrons (those which are in the conduction band), $n_{cb}(\mathbf{E}_{\mathrm{F}})$, and those residing in localized trap states, $n_t(\mathbf{E}_{\mathrm{F}})$. The concentration of conduction band electrons is dependent on the quasi-Fermi level according to:

$$n_{cb}\left(\mathbf{E}_{\mathrm{F}}\right) = N_{c} \exp\left[\frac{\mathbf{E}_{\mathrm{cb}} - \mathbf{E}_{\mathrm{F}}}{k_{B}T}\right]$$
 5.3

where N_c is the effective density of states in the conduction band and \mathbf{E}_{cb} is the energy of the conduction band minimum. A value of $\mathbf{E}_{cb}/\mathbf{q} \approx -0.7$ V vs. Ag/AgCl was used from literature data of anatase TiO₂ nanoparticle electrodes in contact with 0.1 M Li⁺ in acetonitrile.(31) The effective density of states in the conduction band was determined using the effective electron mass of $m_e^* = 10m_e$ providing a value of $N_c = 8 \times 10^{20}$ cm⁻³.(32, 33)

For trap states, the concentration of electrons in the TiO_2 given a certain Fermi-level is determined by integrating the density of trap states, $g(\mathbf{E})$, multiplied by the occupancy of those traps. The trap state occupancy is described by the Fermi-Dirac Function, $f(\mathbf{E}-\mathbf{E}_F)$:

$$f\left(\mathbf{E} - \mathbf{E}_{\mathrm{F}}\right) = \frac{1}{1 + exp\left(\mathbf{E} - \mathbf{E}_{\mathrm{F}} / k_{B}T\right)}$$
 5.4

Only electrons in traps with an energy between the solution (zero) potential, $E_{F,\theta}$, and the conduction band are expected to contribute to recombination. The total concentration of electrons in trap states in the energy range $qE_{F,\theta} < \mathbf{E} < \mathbf{E}_{cb}$ is therefore given by

$$n_t(\mathbf{E}_{\mathrm{F}}) = \int_{qE_{F,0}}^{\mathbf{E}_{cb}} g(\mathbf{E}) f(\mathbf{E} - \mathbf{E}_{\mathrm{F}}) d\mathbf{E}$$
 5.5

The distribution of trap states can be determined experimentally through capacitance measurements. Figure 5.2a shows a typical cyclic voltammogram of a TiO_2 nanoparticle electrode in an electrochemically inert electrolyte (0.1 M LiClO₄ in acetonitrile). The small current peak at a potential of -0.3 V, present only in the first scan, has been identified in literature as mono-energetic surface states.(34, 35) Boschloo *et al.* have measured these states spectroelectrochemically to rule out the possibility that this peak is a result of contamination reduction.(34) The larger current at more negative potentials is due to the charging of an exponential distribution of trap states tailing off below the conduction band edge.(35-38) The current density can be transformed to a capacitance, C_{μ} , by

$$J = d(1-p)sC_{\mu}$$
 5.6

where d is the film thickness, p is the porosity, and s is the scan rate. (35) Figure 5.2b shows a plot of $ln(C_{\mu})$ vs. E. The capacitance peak associated with the mono-energetic surface states,

near E = -0.3 V, as well as the exponential distribution of trap states are more apparent in this plot. The total density of trap states can thus be separated into two components: exponentially distributed trap states, $g_{exp}(\mathbf{E})$, and mono-energetic surface states, $g_{s,me}(\mathbf{E})$.

The exponentially distributed density of trap states in TiO_2 has been well established to be described by (37, 39-41)

$$g_{exp}\left(\mathbf{E}\right) = \frac{N_{exp}}{k_B T_0} exp \left[\frac{qE - \mathbf{E}_{cb}}{k_B T_0}\right]$$
 5.7

where N_{exp} is the total density of the exponential distribution of trap states, and T_0 is a characteristic parameter with temperature units describing the depth of the trap state distribution. The tailing parameter is sometimes described in literature as m_c , a parameter with energy units which can be interchanged by $m_c = k_B T_0$ or by a unitless coefficient $\alpha = T/T_0$.(37, 39) The slope of the $\ln(C_\mu)$ data can be used to determine the T_0 parameter from slope = $q/k_B T_0$.(35) A fit of the capacitance data to equation 5.7, shown in figure 5.2b, produced a value of 850 K for T_0 ($m_c = 0.073$ eV, $\alpha = 0.35$). This value is in good agreement with literature values which fall in the range $T_0 = 550-950$ K.(39, 41-43) An estimate of N_{exp} was obtained from the fitted capacitance data as shown in figure 5.2b. The data was integrated from \mathbf{E}_{cb} to $E_{F,0}$, which produced a value of $N_{exp} \approx 1.7 \times 10^{19}$ cm⁻³, in good agreement with literature values.(34, 37, 41)

The mono-energetic surface states were modeled using a normalized Gaussian function

$$g_{s,me}\left(\mathbf{E}\right) = \frac{N_{s,me}}{\sqrt{2\pi\sigma^2}} exp \left[\frac{-\left(\mathbf{E} - qE_{s,me}\right)^2}{2\sigma^2} \right]$$
 5.8

where $N_{s,me}$ is the total density of mono-energetic surface states, $E_{s,me}$ is the potential at the center of the Gaussian function, and σ describes the width of the distribution. Approximate

values for both $N_{s,me}$ and σ were obtained by integrating the difference of the capacitance measured by cyclic voltammetry and the fitted exponential capacitance, $C_{exp,fit}$, shown in figure 5.2c, and determined to be 4.86×10^{17} cm⁻³ and 66 meV respectively. It should be noted, however, that the values derived from these measurements and fits were found to be somewhat variable between films. Further, the center of this distribution, $E_{s,me}$ shifts more positive with slower scan rates as expected. Thus a more positive value than is indicated in figure 5.2c was used for modeling purposes as shown in table 5.1.

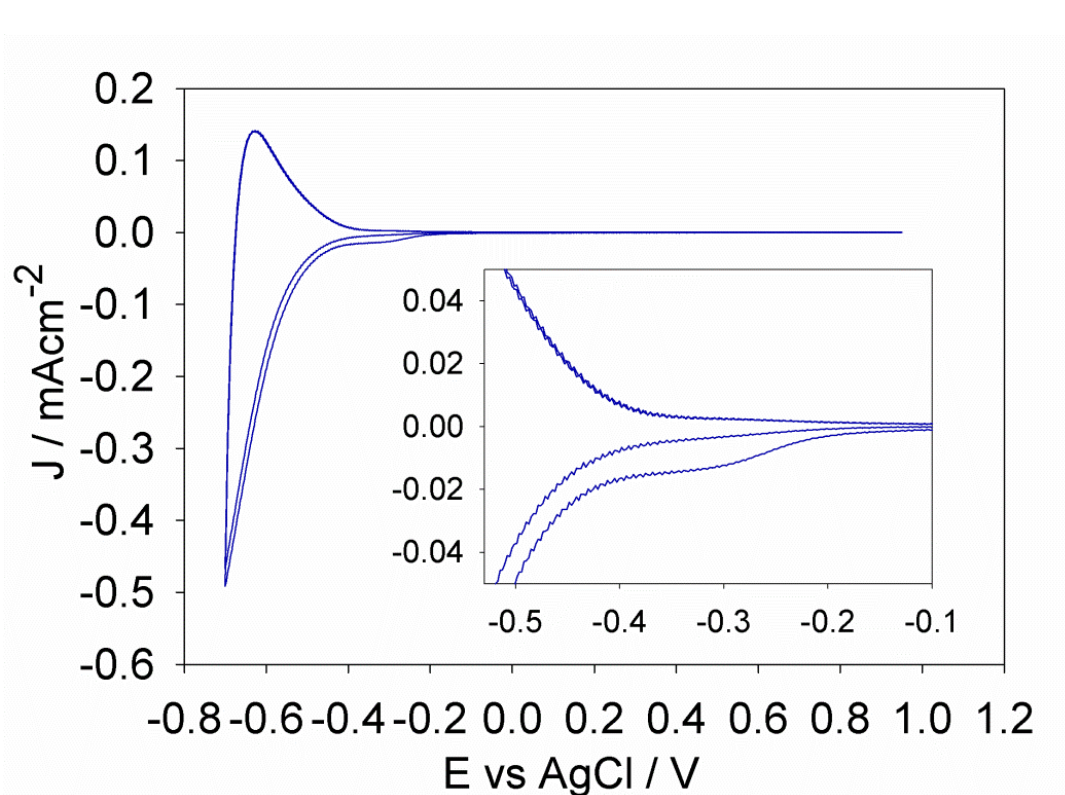
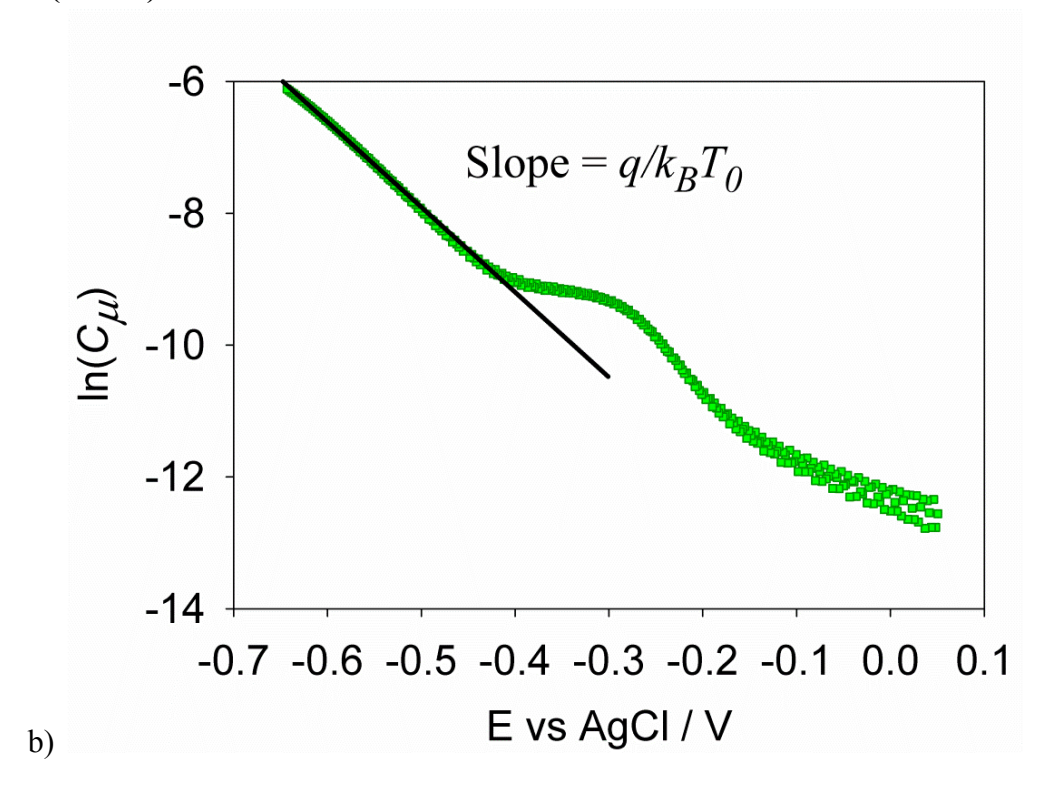
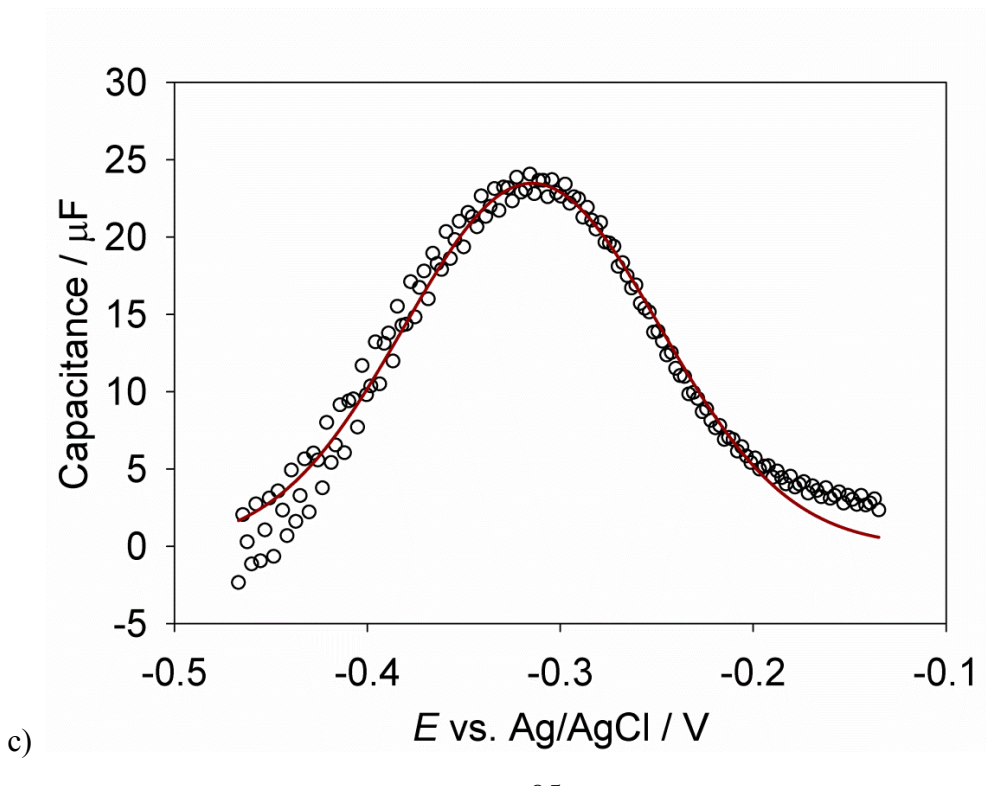


Figure 5.2. a) Cyclic voltammogram and b) plot of $ln(C_{\mu})$ vs potential for a TiO_2 electrode in a blocking electrolyte composed of 0.1 M LiClO₄ in acetonitrile. c) The difference between the measured total capacitance and the fitted exponential capacitance (circles). Also shown is the result of fitting the capacitance difference to a Gaussian (red line).

Figure 5.2 (cont'd)





5.4.2 Recombination Rate

Recombination is comprised of electron transfer from TiO_2 to the oxidized form of the redox shuttle. In general, the equation for recombination density due to electron transfer is

$$U(\mathbf{E}_{\mathbf{F}}) = [A] n(\mathbf{E}_{\mathbf{F}}) k_{\rho t}(\mathbf{E})$$
5.9

where [A] is the concentration of acceptor species dissolved in solution, $n(\mathbf{E}_{\mathrm{F}})$ is the concentration of electrons able to participate in recombination at a given quasi-Fermi level, and $k_{el}(\mathbf{E})$ is the electron-transfer rate constant for electron transfer originating at energy \mathbf{E} in the TiO₂. In principle, any electron that is near the surface in a state higher in energy than qE_{redox} should be able to participate in recombination. The total rate of recombination is then the sum of all recombination reactions. Since we have identified three types of states containing electrons in the section above, we consider three sources of recombination here: electron transfer from 1) the conduction band, U_{cb} , 2) the exponential distribution of surface states, $U_{s,exp}$, and 3) the mono-energetic band of surface states, $U_{s,me}$, displayed in figure 5.3. Use of equation 5.9 allows separate equations to be written for each source of recombination using the proper expressions for $n(\mathbf{E}_{\mathbf{F}})$ and $k_{el}(\mathbf{E})$.

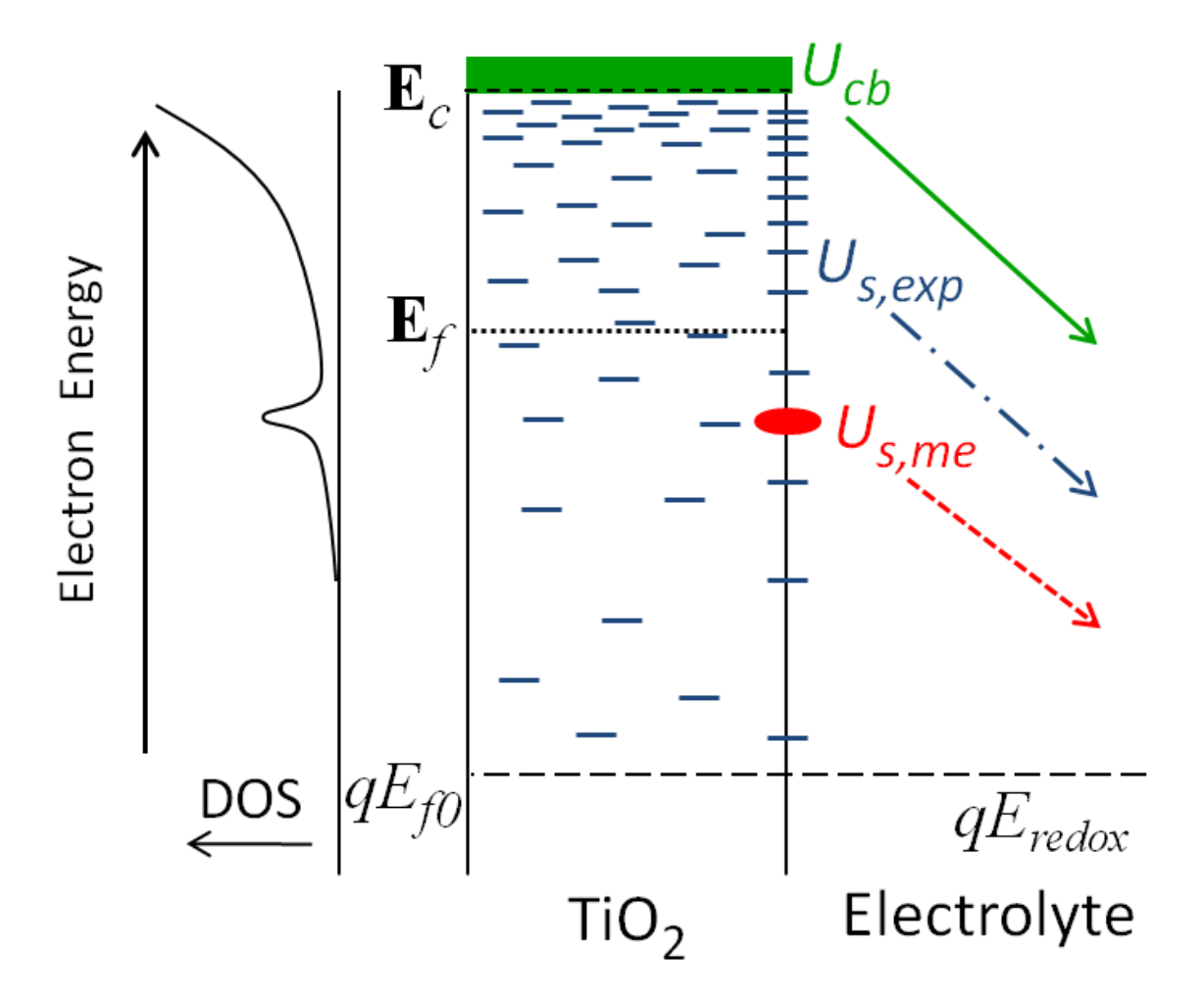


Figure 5.3. Energy diagram displaying the distribution of localized states and recombination from the conduction band (green solid), from an exponential distribution of surface states (blue dot-dash), and from a mono-energetic distribution of states (red dash). $qE_{f,0}$ is the quasi-Fermi level in the dark equilibrated with the redox potential of the redox shuttle, E_{redox} , E_{cb} is the conduction band energy and E_{F} is the Fermi energy.

Recombination resulting from direct electron transfer from the conduction band follows the equation

$$U_{cb}\left(\mathbf{E}_{\mathrm{F}}\right) = [A]V_{f}n_{cb}\left(\mathbf{E}_{\mathrm{F}}\right)k_{et,cb}$$
5.10

where $k_{et,cb}$ is the electron transfer rate constant and V_f is the volume fraction of electrons in the conduction band near enough to the surface to participate in electron transfer. An expression for $n_{cb}(\mathbf{E}_F)$ was presented above (equation 5.3). The volume fraction is determined by the effective coupling length of the acceptor species in solution to the semiconductor electrode. Lewis and co-workers used a coupling length of 0.3 nm to estimate rate constants for electron transfer at semiconductor electrodes, an assumption originating in the approximate width of one gold atom, which does not seem applicable in this work.(44) If the electronic coupling is strong, it has been estimated that adiabatic charge transfer can occur for species up to a nanometer from the electrode surface, which would correspond to a coupling length of 1 nm.(44, 45) Since there is no clear experimental evidence to support an exact value for V_f at this time, electrons within 1 nm of the surface of the nanoparticle are assumed able to participate in recombination, thus $V_f = 0.27$ for the 20 nm in diameter nanoparticles used. The consequences of this assumption are discussed in more detail below in section 5.4.4.

Since electrons transfering from the conduction band are all coming from the same energy – the conduction band minimum – the rate constant has a single value, and the potential dependence of recombination is contained in $n_{cb}(E_F)$. The rate constant has been established to follow the relationship described using Marcus theory(46, 47)

$$k_{et,cb} = k_{et,max} exp \left[\frac{-(\Delta G + \lambda)^2}{4\lambda k_B T} \right]$$
 5.11

where $\Delta G = \mathbf{E}_{cb} - qE_{redox}$ is the driving force of electron transfer and λ is the reorganization energy. The prefactor $k_{\rm et,max}$ is the rate constant at optimum exoergicity, obtained when $-\Delta G^{\rm or}$ = λ . Values of $k_{\rm et,max}$ have been estimated theoretically, and confirmed experimentally, to be

approximately $10^{-17} - 10^{-16}$ cm⁴ s⁻¹.(46-48) In addition, the value of $k_{\rm et,max}$ is expected to be a weak function of the reorganization energy $\left(k_{\rm et,max} \propto \lambda^{-1/2}\right)$. Accounting for this dependency, values of $k_{\rm et,max} = 6 \times 10^{-17}$ cm⁴ s⁻¹ for $\left[\text{Co(Me_2bpy)_3}\right]^{3+/2+}$ and 1.2×10^{-16} cm⁴ s⁻¹ for $\left[\text{Ru(bpy)_2(MeIm)_2}\right]^{3+/2+}$ were used. Determination of the reorganization energies are described below.

Recombination resulting from electron transfer from surface states requires a more elaborate definition. In order to quantify the rate of recombination, the contributions from all occupied surface states must be included. The total density of electron transfer at a given quasi-Fermi level, again only considering surface states in the energy range $qE_{F,0} < \mathbf{E} < \mathbf{E}_{cb}$, is described by

$$U_{s}(\mathbf{E}_{F}) = [A] \int_{qE_{F},0}^{\mathbf{E}_{cb}} f(\mathbf{E} - \mathbf{E}_{F}) [(g_{s,exp}(\mathbf{E}) + g_{s,me}(\mathbf{E})] k_{et,s}(\mathbf{E}) d\mathbf{E}$$
 5.12

where $g_{s,exp}(\mathbf{E})$ is the density of exponentially distributed states at the electrode surface and $k_{et,s}(\mathbf{E})$ is the electron-transfer rate constant from a surface state at energy \mathbf{E} . Here it is assumed the rate constant is strictly a function of energy and thus independent of the type of surface state, however, it is possible that the electronic coupling can differ between types of surface states and acceptor species, which would affect the values of $k_{et,s}(\mathbf{E})$ for these states. The electron-transfer rate constants for transfer from surface states is dependent on the difference between the energy of the surface state, \mathbf{E} , and the solution qE_{redox} , according to (49, 50)

$$k_{et,s}(\mathbf{E}) = k_{et,max} exp \left[\frac{-(\mathbf{E} - qE_{redox} + \lambda)^2}{4\lambda k_B T} \right]$$
 5.13

The density of states of the mono-energetic surface states was presented above. Assuming that the surface (or near surface) states have the same distribution as the bulk trap states, the exponentially distributed density of trap states at (or near) the TiO_2 surface, $g_{s,exp}(\mathbf{E})$, can be described by the volume fraction, V_f , of bulk traps near enough to the surface of the nanoparticle to participate in electron transfer time:

$$g_{s,exp}\left(\mathbf{E}\right) = V_f g_{exp}\left(\mathbf{E}\right) \tag{5.14}$$

There is no definitive evidence that the distribution of trap states is evenly distributed spatially throughout the nanoparticle. It has in fact been suggested that trap states are located preferentially at the nanoparticle surface.(51) The consequence of a distribution of trap states having a higher concentration nearer to the surface is discussed below in section 5.4.4. For simplicity, a homogeneous spatial distribution of trap states and an effective coupling length of 1 nm are assumed.

5.4.3 Reorganization energy

The total reorganization energy is a summation of the inner-sphere and outer-sphere components: $\lambda = \lambda_{in} + \lambda_{out}$. It has been shown for group VIII bipyridyl complexes $\lambda_{in} \approx 0$ for the M^{2+} to M^{3+} transition or vice versa by showing a negligible change in the metal-ligand bond lengths. Therefore for $[Ru(bpy)_2(MeIm)_2]^{3+/2+}$ the following approximation is employed: $\lambda = \lambda_{out}$. (52) A theoretical value for λ_{out} for a redox couple at a TiO₂ interface can be calculated by (7, 53-56)

$$\lambda_{out} = \frac{\left(\Delta zq\right)^{2}}{8\pi\varepsilon_{0}} \left[\frac{1}{a} \left(\frac{1}{n_{sol}^{2}} - \frac{1}{\varepsilon_{sol}} \right) - \frac{1}{2R_{e}} \left(\frac{1}{n_{sol}^{2}} \left(\frac{n_{TiO_{2}}^{2} - n_{sol}^{2}}{n_{TiO_{2}}^{2} + n_{sol}^{2}} \right) - \frac{1}{\varepsilon_{sol}} \left(\frac{\varepsilon_{TiO_{2}} - \varepsilon_{sol}}{\varepsilon_{TiO_{2}} + \varepsilon_{sol}} \right) \right] \right] \quad 5.15$$

where Δz is the change in charge of the acceptor species, n_{sol} and n_{TiO2} are the refractive index of acetonitrile (1.3442)(57) and anatase TiO₂ (2.54)(57) respectively, ε_{sol} and ε_{TiO2} are the static dielectric constants of acetonitrile (36)(58) and anatase TiO₂ (114)(33, 59) respectively, a is the radius of the reactant, and R_e is the distance from the acceptor to the electrode. Using $a = R_e = 0.65$ nm results in a value of $\lambda_{out} = 0.41$ eV which was used as λ for $[\text{Ru}(\text{bpy})_2(\text{MeIm})_2]^{3+/2+}$.(60)

Cobalt bipyridyl redox couples, however, are known to have significant inner-sphere reorganization energies. The inner-sphere reorganization energy at a semiconductor electrode is half of the value derived from a self-exchange reaction, $\lambda_{se,in}$, since half as many molecules participate in each electron-transfer. The total reorganization energy is therefore given by $\lambda = \lambda_{se,in}/2 + \lambda_{out}$. The $\lambda_{se,in}$ has been determined previously to be 2.04 eV.(46) Using equation 15, with $a = R_e = 0.68$ nm, produces a value of $\lambda_{out} = 0.39$ eV.(60) The total reorganization energy for $[\text{Co}(\text{Me}_2\text{bpy})_3]^{3+/2+}$ is therefore (2.04 eV)/2 + 0.39 eV = 1.41 eV.

5.4.4 Calculated lifetimes

Introducing the expressions developed above for electron concentration and recombination rates into equation 5.2 produces the following general expression for electron lifetime:

$$\tau_n(\mathbf{E}_{\mathrm{F}}) =$$

$$\frac{\partial \left(N_{c} \exp\left[\frac{\mathbf{E}_{cb} - \mathbf{E}_{F}}{k_{B}T}\right] + \int_{\mathbf{E}_{F},0}^{\mathbf{E}_{cb}} f\left(\mathbf{E} - \mathbf{E}_{F}\right) \left[\left(g_{exp}(\mathbf{E}) + g_{s,me}\left(\mathbf{E}\right)\right] d\mathbf{E}\right) / \partial \mathbf{E}}{\partial \left[\left[A\right] \left(V_{f} N_{c} \exp\left[\frac{\mathbf{E}_{cb} - \mathbf{E}_{F}}{k_{B}T}\right] k_{et,cb} + \int_{\mathbf{E}_{F},0}^{\mathbf{E}_{cb}} f\left(\mathbf{E} - \mathbf{E}_{F}\right) \left[\left(g_{s,exp}(\mathbf{E}) + g_{s,me}\left(\mathbf{E}\right)\right] k_{et,s}(\mathbf{E}) d\mathbf{E}\right)\right] / \partial \mathbf{E}}$$

Equation 5.16 was used to calculate the electron lifetimes using the parameters displayed in table 5.1. Figure 5.4a shows the experimental lifetimes of $[Ru(bpy)_2(MeIm)_2]^{3+/2+}$ with the results from the calculated lifetimes superimposed. The calculated lifetimes (red solid line), are in excellent agreement with the experimental data.

Modifications of the model further allows for the identification of each source of recombination appearing in the measured lifetimes. For example, removing the contribution of electron transfer from conduction band electrons to recombination has no effect on the calculated lifetimes. This elimination indicates that conduction band recombination is negligible and

Table 5.1: Parameters used for full model of lifetimes given in equation 5.16.

Parameter	Value used for Co	Value used for Ru
$E_{F,0}$ / V vs. Ag/AgCl	0.080	0.890
$E_{ss,me}$ / V vs. Ag/AgCl	-0.16	-0.16
\mathbf{E}_{cb}/q / V vs. Ag/AgCl	-0.7	-0.7
N_c / cm^{-3}	8 × 10 ²⁰	8 × 10 ²⁰
$N_b / \text{ cm}^{-3}$	1.73 × 10 ¹⁹	1.73 × 10 ¹⁹
$N_{s,me}$ / cm ⁻³	1 × 10 ¹⁶	1 × 10 ¹⁶
T / K	295	295
T_{0} / K	850	850
$k_{et,max}$ / cm ⁴ s ⁻¹	1.2×10^{-16}	6×10^{-17}
σ/eV	0.08	0.08
λ/eV	1.41	0.41
$[A] / \text{cm}^{-3}$	1.20×10^{19}	1.20 × 10 ¹⁹

surface state recombination is dominant when using $[Ru(bpy)_2(MeIm)_2]^{3+/2+}$. This result is consistent with recombination from the conduction band being in the Marcus inverted region as expected for this couple. Alternatively, removing the contribution of the mono-energetic surface states to recombination from the model produces a parabolic lifetime with a single minimum located near 0.49 V (green dot dot dash). The experimental minimum in the lifetime at 0.49 V is therefore attributed to recombination from the exponential distribution of surface states. This minimum occurs near where $-\Delta G = \lambda$, and thus the $k_{et}(\mathbf{E})$ function reaches its maximum. The minimum in lifetime is shifted slightly from $\mathbf{E}_{redox} - \lambda$, however, due to the contribution of the increasing $g_s(\mathbf{E})$ function to the overall rate of recombination. Finally, removing the contribution of the exponential distribution of surface states to recombination produces a parabolic lifetime with a single minimum located near 0.05 V (blue dash). The experimental minimum in the lifetime at 0.05 V is therefore attributed to recombination from mono-energetic surface states. The minimum in the lifetime is near the energetic center of the mono-energetic surface states, but is shifted positive due to the sharply decreasing $k_{et}(\mathbf{E})$ function with more negative potentials.

The full model using [Co(Me₂bpy)₃]^{3+/2+} results in a reasonable fit over part of the experimental data, but deviates at more positive potentials, shown in figure 5.4b. Removal of the contribution to recombination from the mono-energetic surface states from the full model given in equation 5.16, results in the calculated lifetimes being in excellent agreement with the experimental results. Further removal of recombination from the exponential distribution of surface states does not significantly change the modeled lifetime and thus only one line is included in figure 5.4b for clarity. It is interesting that the mono-energetic surface states appear

to contribute to recombination to [Ru(bpy)₂(MeIm)₂]³⁺, but not to [Co(Me₂bpy)₃]³⁺. In chapter 3, linear (semi-logarithmic) lifetimes for an array of cobalt polypyridyl redox shuttles are presented, similar to the data presented here.(11, 20) Peter and coworkers also reported linear (semi-logarithmic) lifetimes to the [Co(dbbip)₂]^{3+/2+} (dbbip = 2,6-bis(1'-butylbenzimidazol-2'-yl)pyridine) redox shuttle, in agreement with our measurements.(61) The difference may be explained by the cobalt-based redox shuttles coupling weaker to the mono-energetic surface states compared to the ruthenium-based redox shuttle. Hupp and coworkers, however, reported non-linear (semi-logarithmic) lifetimes for a series of cobalt-based redox shuttles, which appears to be consistent with our model including the mono-energetic surface states.(26) As noted above and reported by others, we have found a fairly large variance in the magnitude of the mono-energetic states' capacitance, for different electrodes and preparation procedures. Thus, differences in the nanoparticle preparation can possibly account for differences is linearity of measured lifetimes.

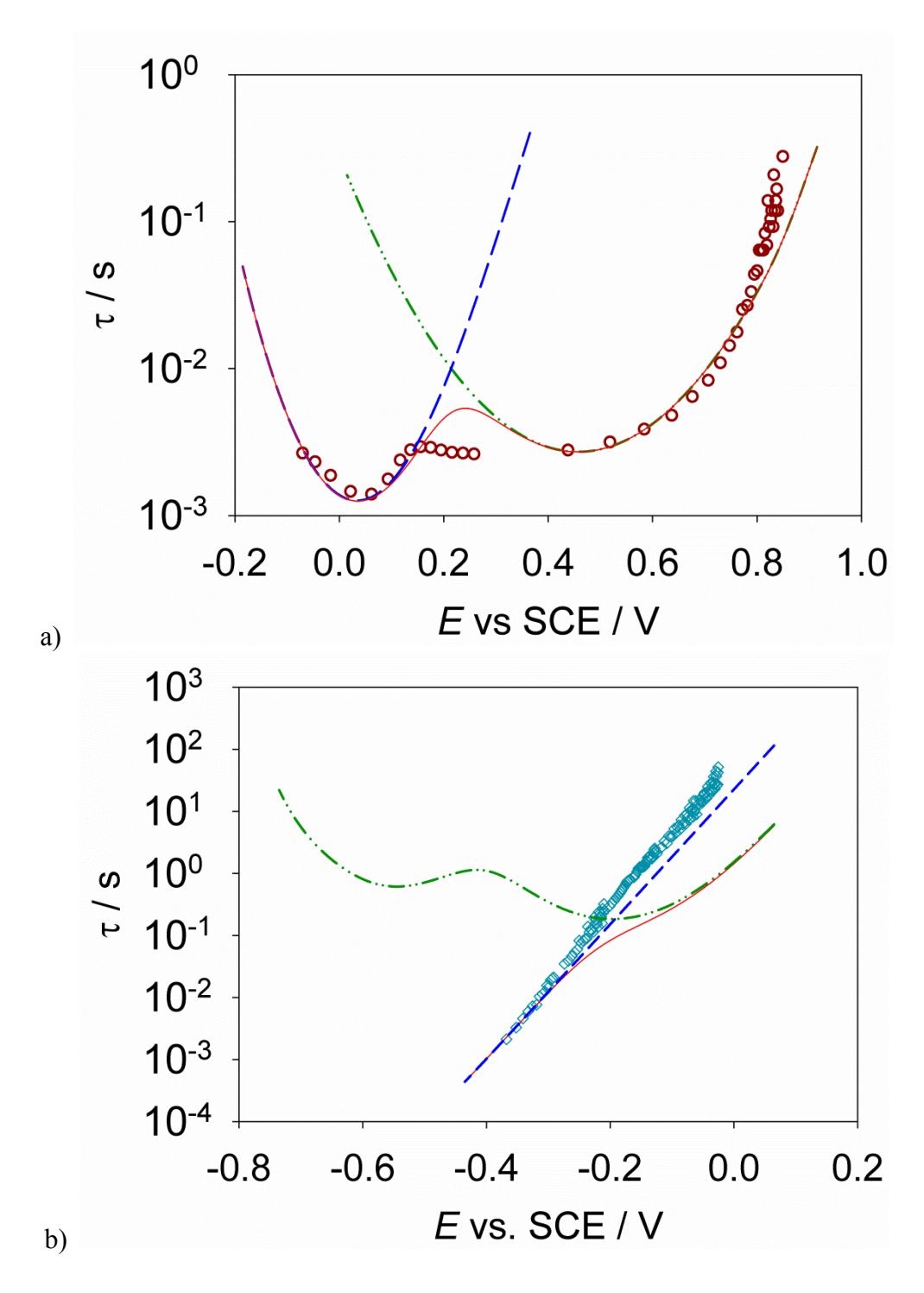


Figure 5.4. Experimental and modeled lifetimes for both a) $[Ru(bpy)_2(MeIm)_2]^{3+/2+}$, experimental (circles), full model (red line), model without $U_{s,me}$ (green, dot-dot-dash), model without $U_{s,exp}$ (blue, dash), and b) $[Co(Me_2bpy)_3]^{3+/2+}$: experimental (diamonds), full model (red line), without surface state recombination (blue, dash), and without conduction band recombination (green line, dot-dot-dash).

As mentioned, removal of recombination from surface states to $[Co(Me_2bpy)_3]^{3+/2+}$ gives excellent agreement with experimental lifetimes. Likewise, considering only recombination from surface states and removing conduction band recombination, results in a failure to fit the experimental data, figure 5.4b. This case results once again with two parabolic components to the calculated lifetimes as with the ruthenium redox shuttle, however, due to the large increase in λ the contributions are reversed; the minimum centered near -0.2 V results from $U_{SS,me}$ while the minimum at more negative potentials results from $U_{SS,exp}$.

If a smaller coupling length were used in the calculation it would produce a smaller V_f ; which would result in an increase in the electron lifetime. For example, using a coupling length of 0.3 nm, instead of 1 nm, would produce $V_f = 0.09$ and increase the calculated lifetime by a factor of 3 as shown in figure 5.5. Additionally, the distribution of trap states may not have a spatially homogeneous distribution and may have an increased concentration nearer to the surface which would produce a larger $g_{s,exp}(\mathbf{E})$ and concomitantly shorter lifetimes. If a lower value for V_f were employed as described above, the decreased lifetimes could be offset by the surface-concentrated trap states. Any error on the value of either of these parameters would result in a proportionally minor shift in the magnitude of the calculated lifetimes (up to a factor of 3), however the shape of the lifetimes would be unaffected as shown in figure 5.5.

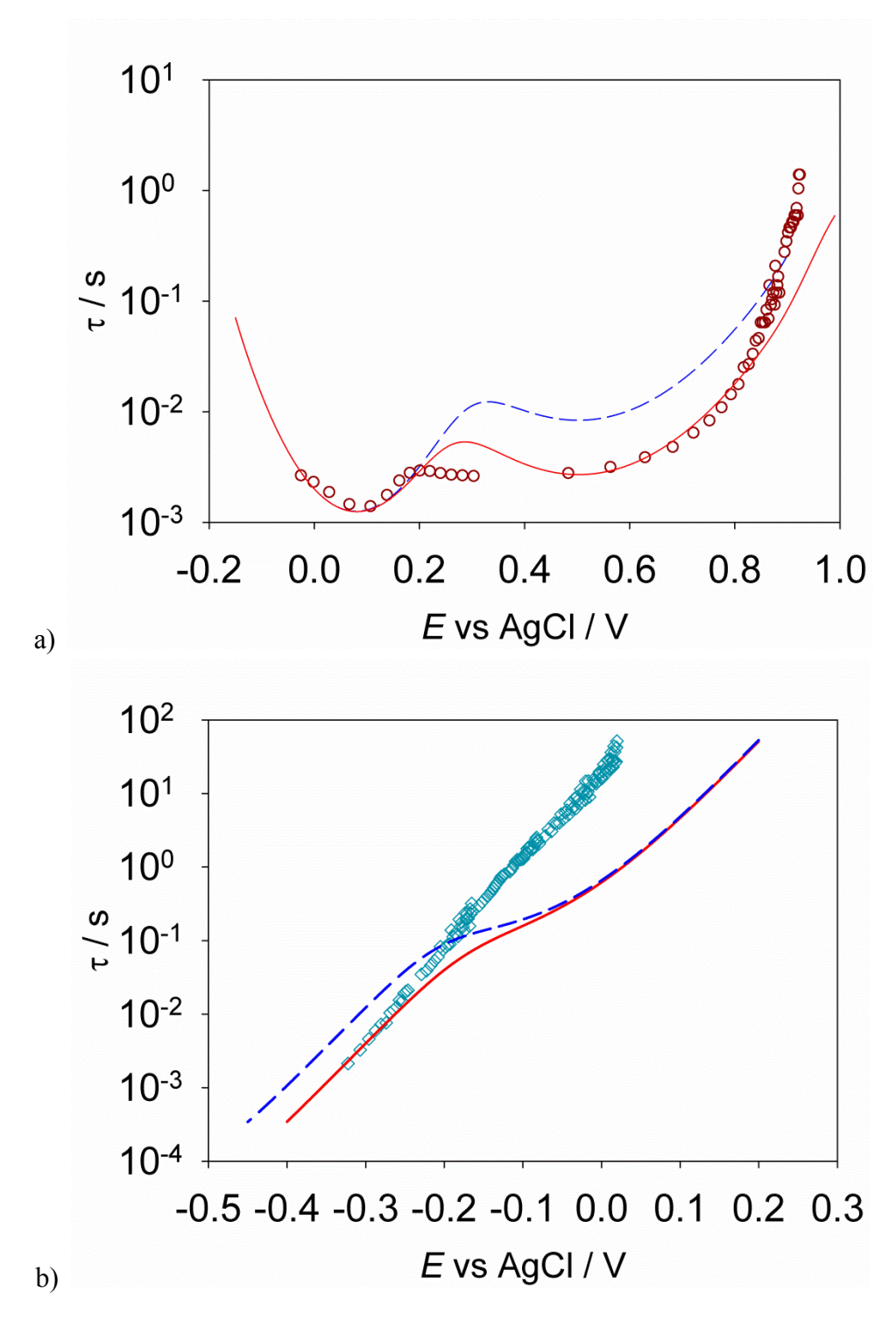


Figure 5.5. Experimental and modeled lifetimes demonstrating coupling length dependence on recombination for both a) $[Ru(bpy)_2(MeIm)_2]^{3+/2+}$ and b) $[Co(Me_2bpy)_3]^{3+/2+}$ experimental (hollow symbols), full model with 1 nm coupling length (red line, solid), and full model with 0.3 nm coupling length without surface state recombination (blue line, dashed).

5.5 Conclusions

Measurements of recombination to outer-sphere redox shuttles with widely varying E_{redox} and λ produced widely varying magnitude and potential dependency of the electron lifetimes. In order to interpret this behavior, a model was developed using Marcus theory to describe recombination from three distinct sources of electrons: the conduction band, an exponential distribution of surface states and mono-energetic surface states. logarithmic plots of the lifetimes were linear when $[Co(Me_2bpy)_3]^{3+/2+}$ was the redox shuttle. This behavior is in accord with our model when recombination is strictly from the conduction band. These results are in good agreement with previous observations and essentially all literature reports using I_3^-/I^- . It is worth noting that surface state recombination is still expected to occur, however, since the rate is lower compared to recombination from the conduction band, it is not observed experimentally. The semi-logarithmic plots of the lifetimes were parabolic when $[Ru(bpy)_2(MeIm)_2]^{3+/2+}$ was the redox shuttle. This behavior is in accord with our model when recombination is strictly from the surface states. Recombination from the conduction band is also still anticipated to occur, however in this case it is expected to be in the Marcus inverted region and thus significantly slower compared to recombination from surface states. parabolic lifetimes are also in good agreement with Bisquert's predictions of surface state recombination.(18) To the best of our knowledge, however, this is the first definitive experimental verification of surface state dominated recombination in DSSCs.

It is well-known that one strategy to achieve significantly higher efficiency DSSCs is to use redox shuttles with more positive potentials in order to produce higher photovoltages.(1) We

and others have previously demonstrated that when 'slow' redox shuttles are employed, such as $[\text{Co}(\text{X}_2\text{bpy})_3]^{3+/2+}$ or pseudo-halogens, a more positive potential increases the rate of recombination, thus off-setting (at least) any gains in voltage.(3, 11, 20) This behavior is consistent with Marcus normal region behavior of recombination. This work demonstrates that Marcus inverted behavior can be observed using very positive redox shuttles with slow recombination from the conduction band. Recombination from surface states, however, becomes energetically favored, and as a result even shorter lifetimes are observed. These combined results highlight the challenge faced when designing alternative redox shuttles which are capable of exceeding the performance of the long-standing champion I_3^-/I^- .

REFERENCES

REFERENCES

- 1. T. W. Hamann, R. A. Jensen, A. B. F. Martinson, H. Van Ryswyk, J. T. Hupp, *Energy Environ. Sci.* **1**, 66 (2008).
- 2. B. A. Gregg, F. Pichot, S. Ferrere, C. L. Fields, *J. Phys. Chem. B* **105**, 1422 (Feb, 2001).
- 3. G. Oskam, B. V. Bergeron, G. J. Meyer, P. C. Searson, *J. Phys. Chem. B* **105**, 6867 (Jul, 2001).
- 4. T. W. Hamann, O. K. Farha, J. T. Hupp, *J. Phys. Chem. C* **112**, 19756 (Dec, 2008).
- 5. T. W. Hamann, J. W. Ondersma, Energy Environ. Sci. 4, 370 (2011).
- 6. S. Ardo, G. J. Meyer, *Chem. Soc. Rev.* **38**, 115 (2009).
- 7. D. Kuciauskas, M. S. Freund, H. B. Gray, J. R. Winkler, N. S. Lewis, *J. Phys. Chem. B* **105**, 392 (Jan, 2001).
- 8. D. A. Gaal, J. T. Hupp, *J. Am. Chem. Soc.* **122**, 10956 (Nov, 2000).
- 9. J. Bisquert, A. Zaban, P. Salvador, J. Phys. Chem. B 106, 8774 (Aug, 2002).
- 10. J. Bisquert, F. Fabregat-Santiago, I. Mora-Sero, G. Garcia-Belmonte, S. Gimenez, J. *Phys. Chem. C* **113**, 17278 (2009).
- 11. J. W. Ondersma, T. W. Hamann, J. Phys. Chem. C 114, 638 (2010).
- 12. M. J. DeVries, M. J. Pellin, J. T. Hupp, *Langmuir* **26**, 9082 (Jun, 2010).
- 13. F. Fabregat-Santiago *et al.*, *J. Appl. Phys.* **96**, 6903 (Dec, 2004).
- 14. J. Kruger, R. Plass, M. Gratzel, P. J. Cameron, L. M. Peter, *J. Phys. Chem. B* **107**, 7536 (2003).
- 15. J. Bisquert, V. S. Vikhrenko, *J. Phys. Chem. B* **108**, 2313 (Feb, 2004).
- 16. A. Zaban, M. Greenshtein, J. Bisquert, *ChemPhysChem* 4, 859 (2003).
- 17. G. Schlichthorl, S. Y. Huang, J. Sprague, A. J. Frank, *J. Phys. Chem. B* **101**, 8141 (1997).
- 18. J. Bisquert, A. Zaban, M. Greenshtein, I. Mora-Sero, *J. Am. Chem. Soc.* **126**, 13550 (Oct, 2004).

- 19. I. Mora-Sero et al., Acc. Chem. Res. 42, 1848 (2009).
- 20. B. M. Klahr, T. W. Hamann, J. Phys. Chem. C 113, 14040 (2009).
- 21. P. J. Cameron, L. M. Peter, *J. Phys. Chem. B* **109**, 7392 (Apr, 2005).
- 22. S. A. Sapp, C. M. Elliott, C. Contado, S. Caramori, C. A. Bignozzi, *J. Am. Chem. Soc.* **124**, 11215 (Sep, 2002).
- 23. H. Nusbaumer, S. M. Zakeeruddin, J. E. Moser, M. Gratzel, *Chem.-Eur. J.* **9**, 3756 (Aug, 2003).
- 24. P. J. Cameron, L. M. Peter, S. M. Zakeeruddin, M. Gratzel, *Coord. Chem. Rev.* **248**, 1447 (Jul, 2004).
- 25. J. J. Nelson, T. J. Amick, C. M. Elliott, J. Phys. Chem. C 112, 18255 (Nov, 2008).
- 26. M. J. De Vries, M. J. Pellin, J. T. Hupp, *Langmuir* **26**, 9082 (2010).
- 27. B. A. Gregg, Coord. Chem. Rev. 248, 1215 (Jul, 2004).
- 28. A. B. Walker, L. M. Peter, K. Lobato, P. J. Cameron, *J. Phys. Chem. B* **110**, 25504 (Dec, 2006).
- 29. ****, To clarify notation used throughout this work: an italicized E denotes potential while a bold E denotes energy.
- 30. G. Boschloo, A. Hagfeldt, Acc. Chem. Res. 42, 1819 (2009).
- 31. G. Redmond, D. Fitzmaurice, *J. Phys. Chem.* **97**, 1426 (Feb. 1993).
- 32. J. Nelson, *The Physics of Solar Cells*. (Imperial College Press, London, 2003), pp. 9-11.
- 33. B. Enright, D. Fitzmaurice, *J. Phys. Chem.* **100**, 1027 (1996).
- 34. G. Boschloo, D. Fitzmaurice, *J. Phys. Chem. B* **103**, 2228 (1999).
- 35. J. Bisquert et al., Inorg. Chem. Acta **361**, 684 (2008).
- 36. A. Kay, R. Humphry-Baker, M. Gratzel, *J. Phys. Chem.* **98**, 952 (1994).
- 37. F. Fabregat-Santiago, I. Mora-Sero, G. Garcia-Belmonte, J. Bisquert, *J. Phys. Chem. B* **107**, 758 (2003).

- 38. Z. Zhang, S. M. Zakeeruddin, B. C. O'Regan, R. Humphry-Baker, M. Gratzel, *J. Phys. Chem. B* **109**, 21818 (2005).
- 39. J. van de Lagemaat, A. J. Frank, J. Phys. Chem. B 104, 4292 (2000).
- 40. G. Boschloo, A. Hagfeldt, *J. Phys. Chem. B* **109**, 12093 (2005).
- 41. L. M. Peter, J. Phys. Chem. C 111, 6601 (May, 2007).
- 42. R. Konenkamp, *Physical Review B* **61**, 11057 (2000).
- 43. A. C. Fisher, L. M. Peter, E. A. Ponomarev, A. B. Walker, K. G. U. Wijayantha, *J. Phys. Chem. B* **104**, 949 (2000).
- 44. W. J. Royea, A. M. Fajardo, N. S. Lewis, *Journal of Physical Chemistry B* **102**, 3653 (Apr 30, 1998).
- 45. S. W. Feldberg, N. Sutin, *Chemical Physics* **324**, 216 (May 9, 2006).
- 46. T. W. Hamann, F. Gstrein, B. S. Brunschwig, N. S. Lewis, *J. Am. Chem. Soc.* **127**, 13949 (Oct 12, 2005).
- 47. T. W. Hamann, F. Gstrein, B. S. Brunschwig, N. S. Lewis, *J. Am. Chem. Soc.* **127**, 7815 (Jun 1, 2005).
- 48. W. J. Royea, A. M. Fajardo, N. S. Lewis, *J. Phys. Chem. B* **101**, 11152 (1997).
- 49. R. Memming, *Semiconductor Electrochemistry*. (Wiley-VCH Verlag GmbH, Weinheim, Germany, 2001).
- 50. N. S. Lewis, Zeitschrift Fur Physikalische Chemie-International Journal of Research in Physical Chemistry & Chemical Physics 212, 161 (1999).
- 51. N. Kopidakis, N. R. Neale, K. Zhu, J. van de Langemaat, A. J. Frank, *Appl. Phys. Lett.* **87**, 202106 (2005).
- 52. M. Biner, H.-B. Burgi, A. Ludi, R. C., J. Am. Chem. Soc. 114, 5197 (1992).
- 53. R. A. Marcus, *J. Chem. Phys.* **43**, 679 (1965).
- 54. R. A. Marcus, *Electrochimica Acta* **13**, 995 (1968).
- 55. R. A. Marcus, *J. Phys. Chem.* **94**, 1050 (1990).
- 56. Y. Q. Gao, Y. Georgievskii, R. A. Marcus, *J. Chem. Phys.* **112**, 3358 (Feb 15, 2000).

- 57. D. R. Lide, Ed., CRC Handbook of Chemistry and Physics, (CRC Press, ed. 81, 2001), 81.
- 58. G. E. Blomgren, *Nonaqueous Electrochemistry*. D. Aurbach, Ed., (Marcel Dekker, New York, 1999).
- 59. G. Rothenberger, D. Fitzmaurice, M. Gratzel, J. Phys. Chem. 96, 5983 (Jul, 1992).
- 60. W. J. Royea, T. W. Hamann, B. S. Brunschwig, N. S. Lewis, *J. Phys. Chem. B* **110**, 19433 (2006).
- 61. H. Wang, P. G. Nicholson, L. Peter, S. M. Zakeeruddin, M. Gratzel, *J. Phys. Chem. C* **114**, 14300 (2010).

Chapter 6. Conduction Band Energy Determination by Variable Temperature Spectroelectrochemistry

6.1 Introduction

Nanostructured semiconductor electrodes are an important class of materials exhibiting remarkable performance in energy conversion paradigms such as dye-sensitized solar cells, DSSCs, and photocatalysis.(1-7) The most important electronic parameters of these materials are the conduction and valence band edge positions; knowledge of these energies is crucial in understanding the photophysical and chemical behavior. For example, it is essential in determining the driving force for key charge-transfer reactions, such as recombination in DSSCs or water reduction/oxidation in photocatalytic water splitting.(3, 7-9) Remarkably, however, there is no reliable method to measure the absolute band edge positions in mesoporous semiconductor electrodes. Herein a simple new method to measure the band energies in such electrodes is described.

Before discussing the novel method, it is helpful to discuss shortcomings in traditional methods for determining band edge positions when applied to mesoporous semiconductors. Mott-Schottky analysis is the most commonly used method to measure band edge positions of flat crystalline semiconducting electrodes; however this cannot be accurately applied to nanostructured electrodes. The Mott-Schottky equation is derived from modeling the depletion region capacitance as a parallel plate capacitor, and is thus applicable to flat semiconductor-electrolyte interfaces. The use of nanoparticles, for example, immersed in an electrolyte would require solution of Poisson's equation in spherical coordinates,(10) analogous to that derived for nanorods.(11) In addition, the depletion region for nanoparticle based semiconductors is typically

larger than the radius of the nanoparticle, making the film unable to support traditional band-bending required for such techniques.(12-14) Furthermore, Mott-Schottky analysis describes the depletion region capacitance in terms of the dopant density, $N_{\rm D}$; however a nanoparticle based film comprised of 10 nm diameter particles of a semiconductor with $N_{\rm D} = 10^{17}$ cm⁻³, which has been measured for thin dense films of anatase TiO₂ annealed in air to 500 °C,(15) translates to one dopant for every twenty nanoparticles. Clearly a homogenous depletion region capacitance would not be produced under such conditions.

During the 1990s Fitzmaurice and co-workers conducted a series of studies focused on using spectroelectrochemistry to determine the conduction band position in mesoporous nanoparticle based transparent semiconducting films. (16-22) This method relies on determining the concentration of electrons in the conduction band of the semiconducting film by measuring the absorption of sub-band gap energy photons, typically near-IR, by these electrons as a function of applied potential. The absorbance spectrum of electrons in mesoporous TiO2 has garnered much debate over the past twenty years.(14, 16-18, 21, 23-28) This debate arises from very broad absorption features and wildly ranging conditions in which measurements are taken (protic vs. aprotic solvents, pH, presence of intercalating cations, etc.). Nevertheless, the resulting estimates for Ecb in TiO2 from spectroelectrochemistry studies have been used for nearly twenty years, despite several drawbacks that have become apparent with these measurements. These problems include: (1) the assumption of a flat interface and an accumulation layer is maintained throughout the film, (17) an assumption that has been demonstrated to be highly unlikely. (12, 14, 29) (2) The requirement that a large negative bias be applied to the electrode to achieve a substantial accumulation layer irreversibly alters the electrode during the measurement when electrolytes contain small cations that can intercalate.(19, 21, 23, 30) (3) The extinction coefficient of conduction band electrons and the dopant density must be known or easily estimated.(22, 31) (4) Monitoring the absorbance of TiO₂ during a cyclic voltammogram results in a large hysteresis and a scan rate dependence on the absorbance indicating steady-state electron filling is not achieved.(21)

In this chapter a variable temperature spectroelectrochemical measurement to determine the conduction band edge in transparent mesoporous semiconducting electrodes which overcomes the limitations of Mott Schottky and spectroelectrochemical techniques applied previously is introduced. The absorbance of conduction band electrons, following Beer's Law, is given by $A = \varepsilon ln_{cb}$, where ε is the molar extinction coefficient, l is the effective path length and n_{cb} is the electron concentration in the conduction band of TiO₂. The quantity n_{cb} can be calculated according to the equation:(32, 33)

$$n_{cb} = N_c \exp\left(\frac{\mathbf{E}_{cb} - \mathbf{E}_F}{k_B T}\right)$$
 6.1

where $k_{\rm B}$ is Boltzmann's constant, T is temperature, $\mathbf{E}_{\rm cb}$ is the energy of the conduction band minimum, $\mathbf{E}_{\rm F}$ is the Fermi level energy and $N_{\rm c}$ is the effective conduction band density of states. $N_{\rm c}$ can be calculated according to:(32)

$$N_c = 2 \left(\frac{m_e^* k_B T}{2\pi \hbar^2} \right)^{3/2} \tag{6.2}$$

where m_e^* is the effective mass of an electron ($m_e^* \approx 10 \ m_e$ for TiO₂).(34) Inserting equation 6.1 into Beer's law, and taking the natural log for an Arrhenius type temperature dependent equation results in the following final equation:

$$\ln(A) = \ln(\varepsilon l N_c) + \frac{1}{T} \left(\frac{\mathbf{E}_{cb} - \mathbf{E}_F}{k_B} \right)$$
 6.3

Thus, a plot of $\ln(A)$ vs. 1/T should be near linear with a slope that produces the conduction band energy directly. In addition, the intercept yields the extinction coefficient of conduction band electrons. It is important to note that there is a slight temperature dependence of the density of states function, demonstrated by equation 6.2, which additionally needs to be accounted for to accurately determine the extinction coefficient. As a point of reference, at 300 K a value of $N_c = 7.94 \times 10^{20}$ cm⁻³ is obtained from equation 6.2.

6.2 Experimental Considerations for Spectroelectrochemistry

In order to obtain reliable and reproducible results, it is necessary to avoid strong accumulation conditions in the TiO_2 which leads to lithium intercalation and the formation of lithium titanate according to equation 6.4.(24, 25, 30)

$$xLi^{+} + xe_{TiO_{2}}^{-} + TiO_{2} \rightarrow Li_{x}TiO_{2}$$
 6.4

To this end a potential range was determined in which Li⁺ was not noticeably intercalated into the TiO₂ electrode. Absorbance spectra were taken over a wide potential range, subtracting the baseline absorbance which was taken at 0.5 V vs. Ag/AgCl, displayed in figure 6.1. The baseline potential was chosen since the absorbance does not change with potential over a large potential range near 0.5 V vs. Ag/AgCl. At significantly negative potentials a large localized peak appear near 700 nm indicates when lithium intercalation is appreciable and trapped electrons significantly absorb as both have been shown to present local maxima in the range 700-770 nm.(21, 24-26, 28) An additional absorption of trapped electrons appears near 400 nm and has been correlated to surface traps.(20)

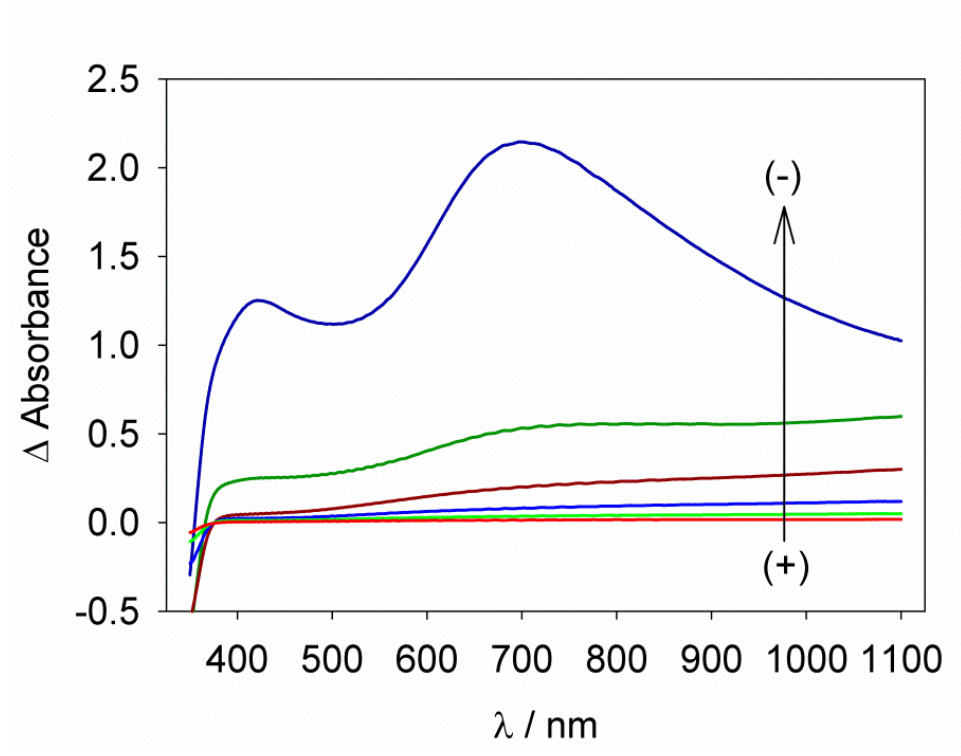


Figure 6.1. Change in absorbance from -0.70, -0.80, -0.90, -1.00, -1.10, and -1.15 V vs. Ag/AgCl to 0.5 V vs. Ag/AgCl. Potentials move from more negative to more positive from top to bottom in the figure as indicated.

Past spectroelectrochemical measurements used to determine the conduction band edge in TiO₂ used potential rages that went well negative of the potential range in figure 6.1.(19) To demonstrate that this lithium intercalation process is irreversible a measurement of the percent transmittance, %T, at 800 nm while performing 25 cycles of cyclic voltammetry from 0 to -2 V vs. Ag/AgCl, similar to the wavelength and potential range used in past spectroelectrochemical measurements containing lithium, is shown in figure 6.2a.(19, 21) It is apparent that the electrode is strongly intercalating lithium, leading to an ever increasing absorbance with each additional scan as the composition of the electrode changes according to equation 6.4. In contrast, performing 25 cycles of cyclic voltammetry from 0.5 to -1 V vs. Ag/AgCl results in consistent %T changes and constant electron absorption features such as shown in figure 6.2b, indicating that Li⁺ intercalation is not interfering with measurements over this potential range.

The remainder of the results presented will be limited to monitoring the %T at potentials positive of -1 V vs. Ag/AgCl.

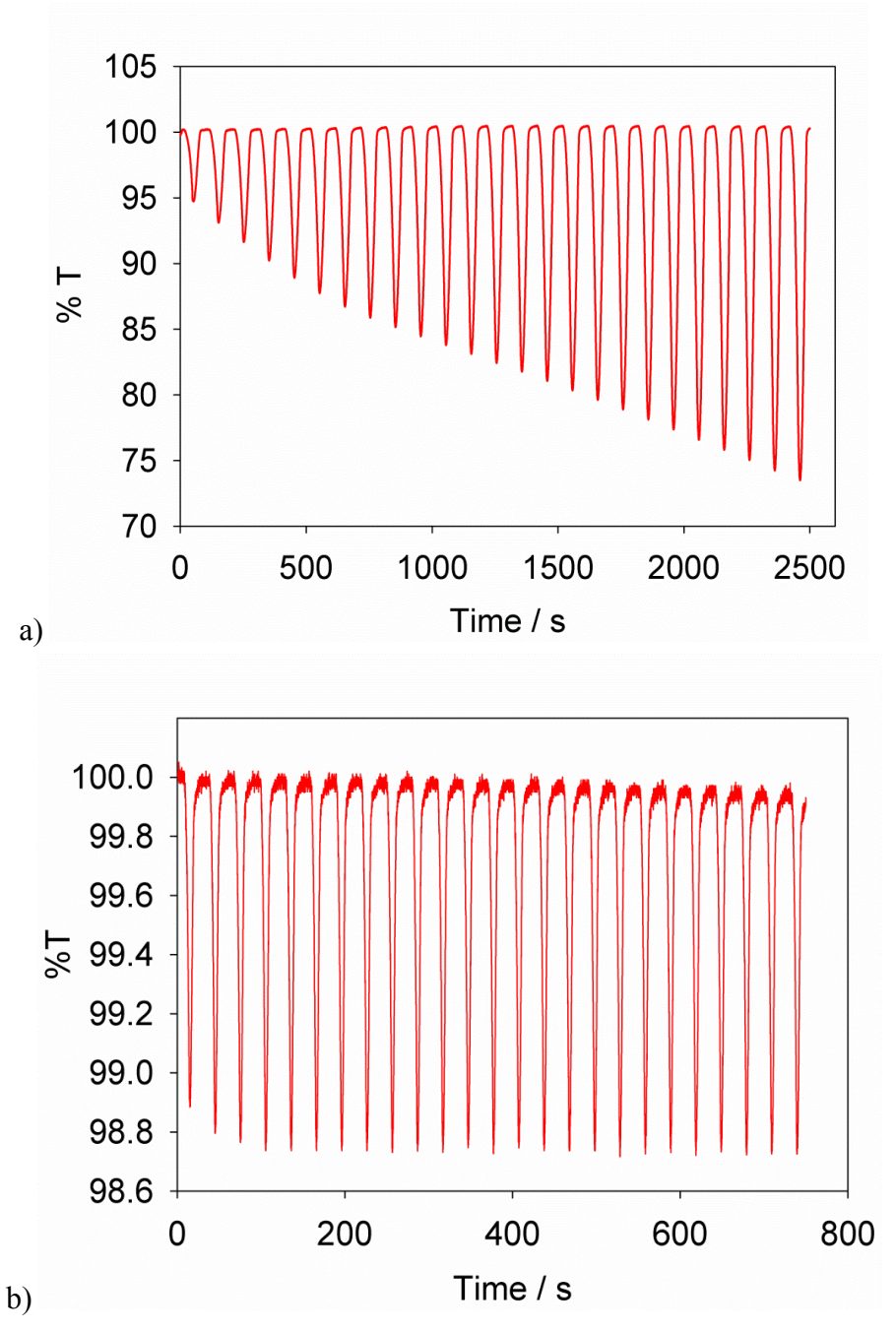


Figure 6.2. Monitoring %T at 800 nm of a nanoparticle based TiO_2 electrode while performing 25 cycles of cyclic voltammetry a) from 0.5 to -2 V vs. Ag/AgCl at 0.05 V/s and b) from 0.5 to -1 V vs. Ag/AgCl at 0.1 V/s.

An additional problem with fitting the absorbance measured during cyclic voltammetry arises from scan rate dependence of the absorbance. This point is demonstrated by plotting the absorbance as a function of potential at several scan rates; the absorbance at any given potential increases as the scan rate is decreased, displayed in figure 6.3. A steady state absorbance value is not achieved. Therefore the electrode must be held at a constant potential (E_F) to achieve steady state conditions in order to determine an accurate absorbance measurement at a given temperature.

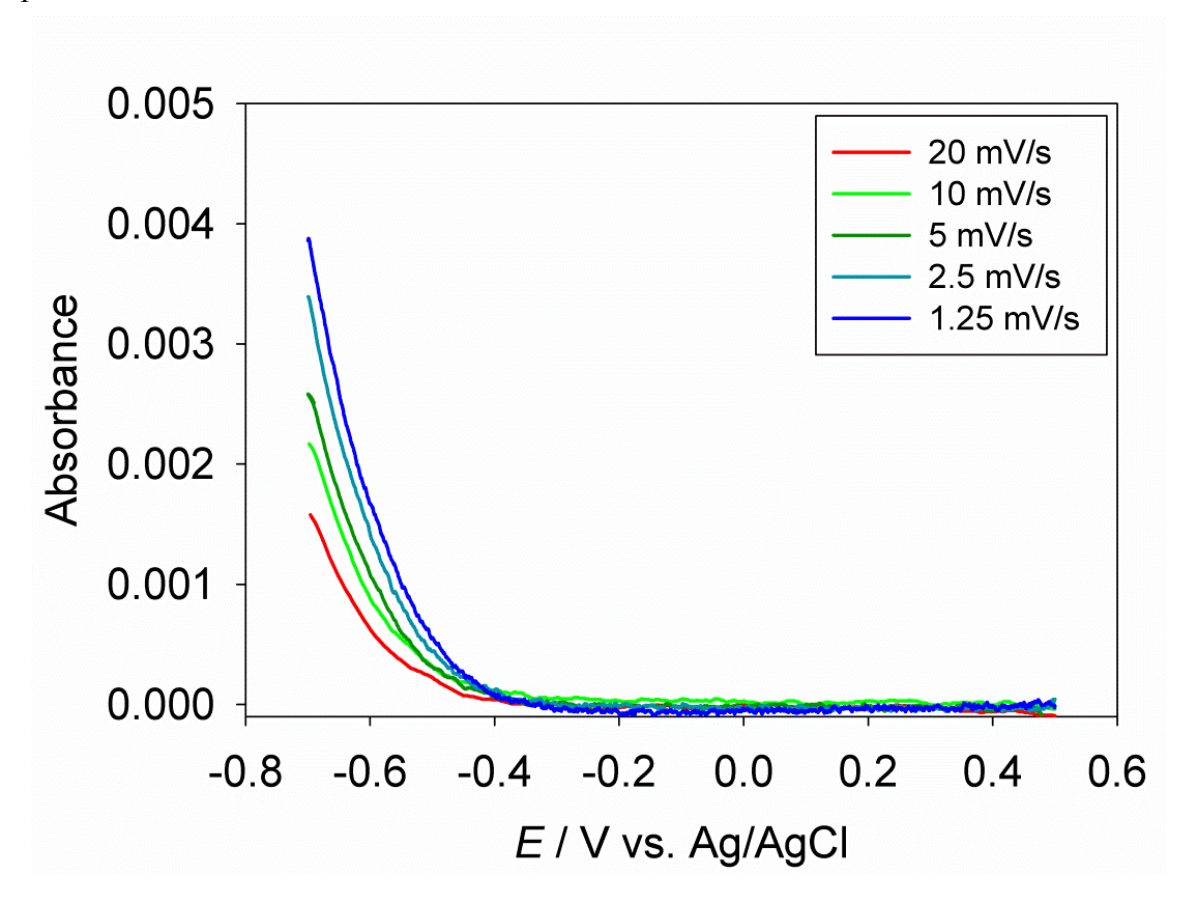


Figure 6.3. Absorbance at 950 nm for a nanoparticle TiO₂ film during cyclic voltammetry with several scan rates from 20 mV/s to 1.25 mV/s.

6.3 Variable Temperature Spectroelectrochemistry Results

An example of a typical optical absorption spectrum of a mesoporous TiO₂ electrode, taken as the difference spectra between 0.5 V and -0.8 V vs. Ag/AgCl, is displayed in figure 6.4. The characteristic features are the bleach of absorbance at wavelengths less than ~380 nm attributed to a Burstein shift, signifying that conduction band filling is occurring.(22, 35) The second characteristic is a lack of local absorbance maxima, indicating that lithium intercalation is not appreciable and trapped electrons are not significantly absorbing at these potentials as discussed above.(21, 24-26, 28) The third characteristic is the observed monotonic increase in absorbance with wavelength, distinctive of a delocalized electron absorption.(26, 36, 37) The fourth characteristic is the interference pattern signifying a highly uniform TiO₂ film.(16, 20)

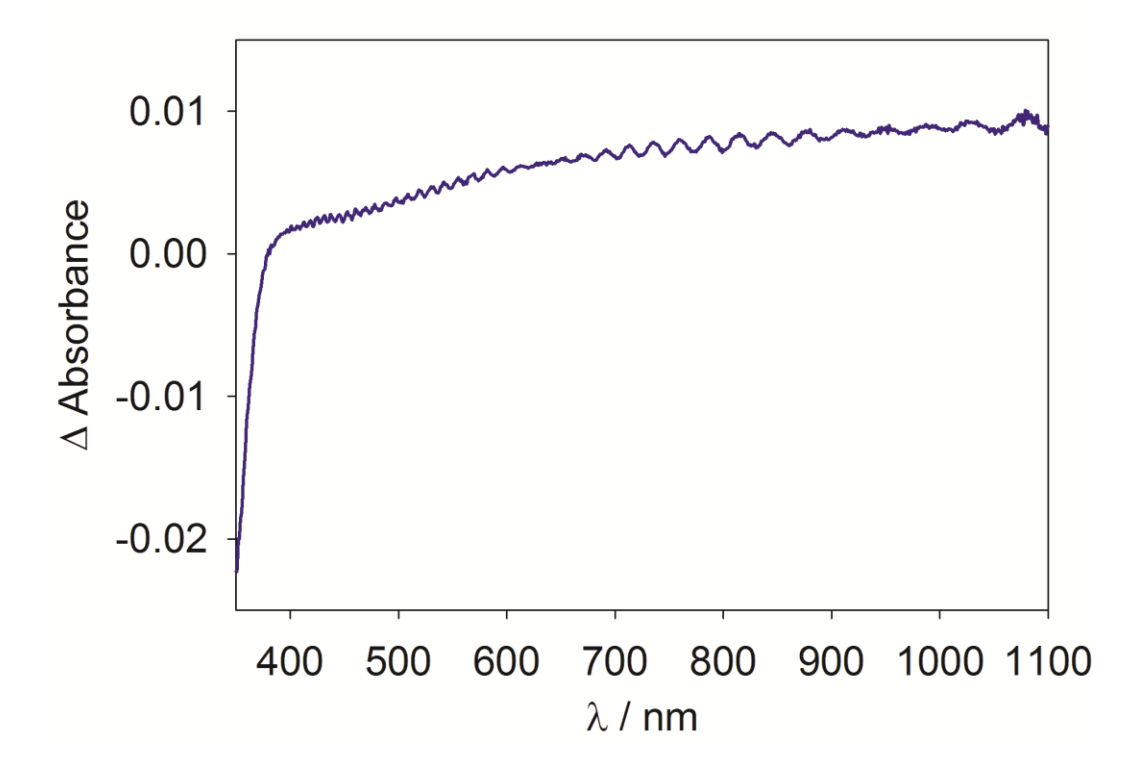


Figure 6.4. Change in absorbance of a TiO_2 electrode when potential is stepped from +0.5 to -0.8 V vs. Ag/AgCl.

The results of monitoring %T at 950 nm of a TiO₂ film while performing chronoamperometry are displayed in figure 6.5. As expected, both increasing the applied potential (moving from left to right in the figure) and increasing the temperature (moving down the plot) decreased the %T of the film. The decreasing %T (thus increasing A) indicates an increased concentration of free conduction band electrons as predicted by equation 6.1.

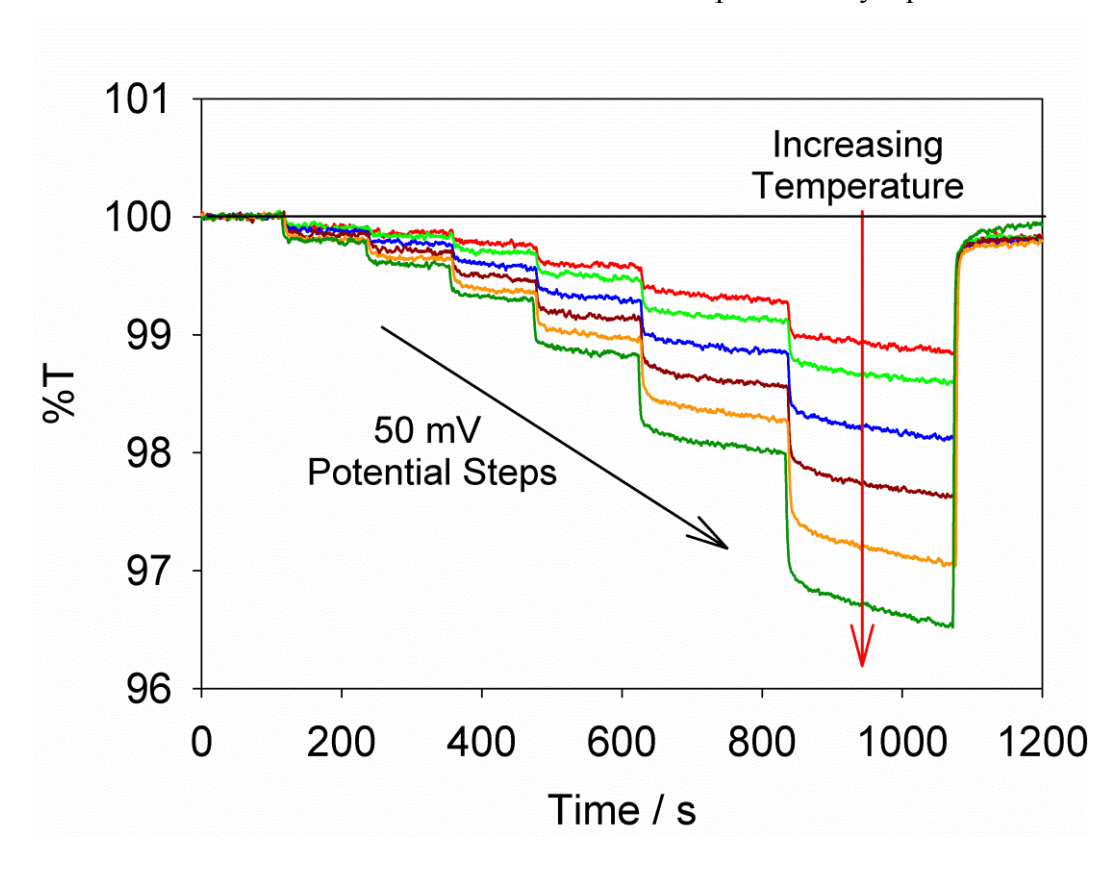


Figure 6.5. Plot of %T at 950 nm while stepping the potential from 0.50 to -0.45, -0.50, -0.55, -0.60, -0.65, -0.70, and back to +0.50 V vs. Ag/AgCl. Each trace represents a different temperature: 15.0, 21.1, 27.5, 34.5, 40.9, 47.3 and 53.8°C, with increasing temperatures resulting in decreasing %T.

The absorbance values averaged for the last 60 seconds of each applied potential at each temperature are plotted in figure 6.6. In order to account for the slight temperature dependence of N_C , equation 6.2 was incorporated into equation 6.3 to produce the following final equation:

$$\ln(A) = \ln\left(\varepsilon l 2 \left(\frac{m_e^* k_B T}{2\pi\hbar^2}\right)^{3/2}\right) + \frac{1}{T} \left(\frac{\mathbf{E}_{cb} - \mathbf{E}_F}{k_B}\right)$$
 6.5

The solid lines in figure 6.6 represent the results of a non-linear least-squares fit to equation (5) for the data obtained at potentials between -0.45 and -0.70 V vs. Ag/AgCl. A global fit to all the data was performed to produce a single value for the extinction coefficient with a conduction band energy that was allowed to float. This fit produced a value of $\varepsilon = 1 \pm 0.3 \times 10^5$ M $^{-1}$ cm $^{-1}$; the fit results for \mathbf{E}_{cb} are displayed in table 6.1. Potentials more positive than -0.45 V vs. Ag/AgCl did not elicit a change in %T that could be accurately measured, as can be seen in figures 6.3 and 6.5, thus representing a limitation to the method introduced herein.

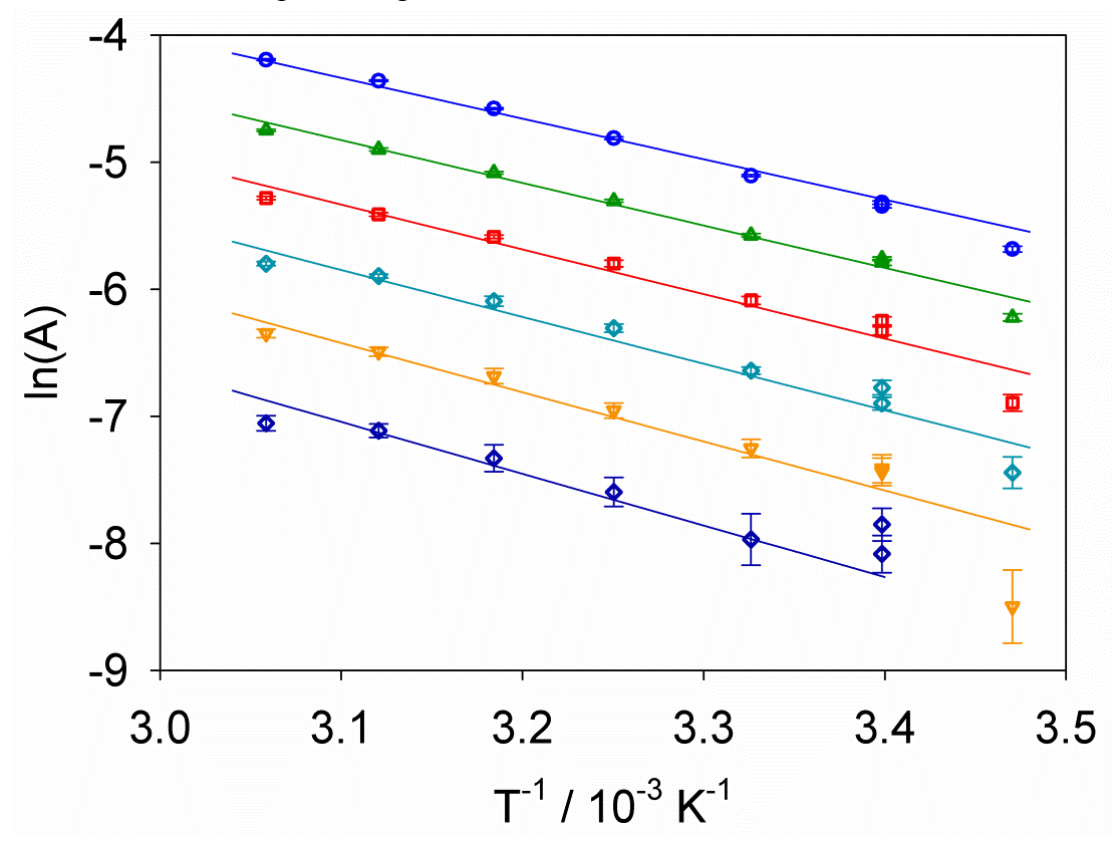


Figure 6.6. Plot of ln(A) vs. T⁻¹ each line represents a different potential from -0.70 to -0.45 V vs. Ag/AgCl in 50 mV increments from top to bottom. The temperatures correspond to 288, 294, 301, 308, 314, 320 and 327 K. Error bars represent one standard deviation. The solid lines depict a global fit result to equation 6.5 as described in the text.

Table 6.1. Fit results of absorbance vs. temperature to equation 6.5.

E_F (mV vs. Ag/AgCl)	E_{cb}/q (mV vs. Ag/AgCl)
-450	-761 ± 6
-500	-794 ± 6
-550	-828 ± 6
-600	-863 ± 6
-650	-899 ± 6
-700	-936 ± 6

6.4 Discussion

Due to the problems with obtaining accurate values for \mathbf{E}_{cb} with Mott Schottky or spectroelectrochemical methods as described above, direct comparison of the presented results to previous literature reports is problematic. However, boundary values for \mathbf{E}_{cb} can be readily determined by considering the energetics in a DSSC; the \mathbf{E}_{cb} must lie somewhere between the dye excited potential, E^{o^*} , and the quasi Fermi level, E_F , at V_{oc} . For the commonly used DSSC sensitizer N3, $E^{o^*} = -1.05$ V vs. Ag/AgCl.(38, 39) The V_{oc} is the difference between the solution potential, E_{redox} , and E_F ; thus E_F can be estimated from subtracting V_{oc} from E_{redox} .(40) Considering the I_3^-/I^- redox shuttle with a $E_{redox} \sim 0.05$ V vs. Ag/AgCl,(2, 39, 41, 42) and a maximal V_{oc} of 0.8 V,(43) a value of $E_F = -0.75$ V vs. Ag/AgCl is produced. This calculation places a limit of $-1.05 < \mathbf{E}_{cb}/q < -0.75$ V vs. Ag/AgCl; in excellent agreement with our measured value.

The results displayed in table 6.1 also show an increasing \mathbf{E}_{cb} with applied potential, consistent with a model of band edge unpinning (also referred to as Fermi-level pinning). This model is based on a semiconductor with a high concentration of electrically active surface states.

Band edge unpinning will occur when the charge in the surface states becomes greater than the charge in the space charge region, resulting in further applied potential being dropped across the Helmholtz layer instead of the semiconductor.(44) Fermi-level pinning is more generally observed rather than an accumulation layer for n-type semiconductors/liquid junctions.(14, 23, 44, 45) This is particularly expected, and has been reported, for porous nanocrystalline TiO₂ due to its very high surface area and known high density of surface states.(14, 45, 46)

The fit results for ε are significantly higher than those that have been presented previously. Literature values of ε for the wavelengths 700-1000 nm are in the range 470-3400 M⁻¹cm⁻¹.(17, 27, 28, 47, 48) These literature values are typically determined by measuring the concentration of electrons in the TiO₂, either by chronoamperometry(28, 47) or titration(48), and comparing this concentration to the measured absorbance. Using chronoamperometry to determine ε from the data displayed in figure 6.5 results in $\varepsilon \approx 1000\text{-}3000 \text{ M}^{-1}\text{cm}^{-1}$, in good agreement with literature values. However, these techniques measure the total concentration of charge in the TiO₂ film, both trapped and free electrons, and could thus substantially over estimate the concentration of electrons contributing to the measured absorbance. Accounting for the relative concentration of trapped and free electrons would easily increase the measured extinction coefficients by one or two orders of magnitude. Indeed, the multiple trapping model used to describe electron transport through nanoparticle TiO₂ electrodes is based on the fact that the vast majority of electrons in the film are trapped, not free. (49-52) Further, as noted above, the model of band edge unpinning is also based on the idea that most electrons are trapped and it has been demonstrated that trapped electrons absorb light differently than free electrons. Therefore, considering these arguments, a measured value of $\epsilon = 1 \pm 0.3 \times 10^5 \text{ M}^{-1} \text{cm}^{-1}$ is in excellent agreement with the reasoning that the majority of electrons in the film are indeed trapped and do not participate in the measured absorption.

Finally, the variable temperature spectroelectrochemical method presented in this work is compared with previous spectroelectrochemical methods. It is worth pointing out that in principle careful spectroelectrochemical measurements could produce E_{cb} by incorporation of equation 6.1 into Beers law. Since the measured absorbance is proportional to ε , this would only produce an accurate value of E_{cb} if an accurate value of ε was independently known. Our results indicate that determination of ε by charge extraction underestimates ε by approximately two orders of magnitude for TiO2, however, which would produce an error of Ecb by ~0.12 eV. Therefore, a significant advantage of the method presented herein is that the temperature variation effect on the absorbance is independent of ε , thus allowing for a more direct and accurate determination of E_{cb} with minimal assumptions or prior knowledge. An additional advantage is that ε is determined simultaneously with E_{cb} ; however we reiterate that accurate determination of ε requires taking into account the temperature dependence of the density of states as shown above. In addition, it has been reported that there may be a small dependence of the band gap and dielectric constant of TiO₂ over the modest temperature variation employed here which was not accounted for. (53) Since the E_{cb} values reported in Table 1 can be obtained at a fixed temperature using our fitted value of ε , i.e. all the data is self-consistent, we believe these effects are negligible.

6.5 Conclusion

The method described herein for conduction band edge determination is relatively simple; it is quick, makes a minimal number of assumptions, does not require a priori knowledge of either n_{cb} or ε for free electrons, and does not require band-gap excitation. The only demands

of this method are the preparation of an electrode with good optical quality and detectable free electron absorption. Additionally, this method is remarkably versatile; this method should allow band edge determination in a variety of porous semiconductor materials.

6.6 Experimental

An ~8 µm thick film of nominally 5 nm radii TiO₂ nanoparticles was deposited on fluorine doped tin oxide, FTO, via a doctor blade technique using Solaronix T/SP TiO₂ paste. A custom jacketed three electrode electrochemical cell was incorporated into a Perkin Elmer Lamda 35 UV-Vis spectrophotometer such that the mesoporous TiO₂ film was positioned normal to the optical path. The temperature of the electrochemical cell was controlled using a Neslab chiller/circulator. The specific temperatures used were 15.0, 21.1, 27.5, 34.5, 40.9, 47.3 and 53.8°C. Practical limitations prohibited expanding the temperature range, at cooler temperatures condensation formed on the outside of the cell and warmer temperatures were avoided in order to maintain reference electrode stability.

Cyclic voltammetry and potential step voltammetry (chronoamperometry), using an μAutoLabII potentiostat/galvonostat, were performed while monitoring the percent transmittance, %T, of the TiO₂ electrode. For the potential step measurements the potential started at 0.5 V, stepped to −0.45 and then stepped in 50 mV increments to −0.7 V before being returned to 0.5 V. Between measurements the potential was held at 0.5 V vs. Ag/AgCl to drain excess electrons from the TiO₂, %T returned to 100%. All %T measurements are given setting the %T at 0.5 V as 100 %T. A control was constructed using a bare FTO electrode to confirm the absence of any contribution to the %T measurement from the FTO due to varying either potential or temperature. The potential was measured vs. a Ag/AgCl reference electrode (EDAQ ET072) determined to be −400 mV vs. ferrocene, and a platinum wire was used as a counter electrode.

All measurements reported here where made using an electrolyte of $0.20~M~LiClO_4$ in acetonitrile, replaced every hour to prevent an appreciable concentration of Ag^+ or Cl^- from building up due to migration through the reference electrode frit. Data fitting was performed using Origin Pro 8.

REFERENCES

REFERENCES

- 1. S. Ardo, G. J. Meyer, *Chem. Soc. Rev.* **38**, 115 (2009).
- 2. A. Hagfeldt, G. Boschloo, L. C. Sun, L. Kloo, H. Pettersson, *Chem. Rev.* 110, 6595 (Nov, 2010).
- 3. M. G. Walter et al., Chem. Rev. 110, 6446 (2010/11/10, 2010).
- 4. X. Chen, S. Shen, L. Guo, S. S. Mao, *Chem. Rev.* **110**, 6503 (2010/11/10, 2010).
- 5. D. Gust, T. A. Moore, A. L. Moore, *Accounts of Chemical Research* **42**, 1890 (2009/12/21, 2009).
- 6. W. J. Youngblood, S.-H. A. Lee, K. Maeda, T. E. Mallouk, *Accounts of Chemical Research* 42, 1966 (2009/12/21, 2009).
- 7. A. Kay, I. Cesar, M. Gratzel, *J. Am. Chem. Soc.* **128**, 15714 (Dec, 2006).
- 8. J. W. Ondersma, T. W. Hamann, J. Am. Chem. Soc. 133, 8264 (2011).
- 9. C. M. McShane, K. S. Choi, *J. Am. Chem. Soc.* **131**, 2561 (Feb, 2009).
- 10. L. M. Peter, *Physical Chemistry Chemical Physics* **9**, 2630 (Jun 7, 2007).
- 11. I. Mora-Sero et al., Appl. Phys. Lett. 89, (Nov. 2006).
- 12. W. J. Albery, P. N. Bartlett, *J. Electrochem. Soc.* **131**, 315 (1984).
- 13. G. Hodes, I. D. J. Howell, L. M. Peter, *J. Electrochem. Soc.* **139**, 3136 (Nov. 1992).
- 14. F. Cao et al., J. Phys. Chem. 99, 11974 (1995).
- 15. H. Tian, Z. Yu, A. Hagfelt, L. Kloo, L. Sun, J. Am. Chem. Soc. 133, 9413 (2011).
- 16. B. O'Regan, M. Gratzel, D. Fitzmaurice, *Chem. Phys. Lett.* **183**, 89 (1991).
- 17. G. Rothenberger, D. Fitzmaurice, M. Gratzel, J. Phys. Chem. 96, 5983 (Jul, 1992).
- 18. B. O'Regan, M. Gratzel, D. Fitzmaurice, *J. Phys. Chem.* **95**, 10525 (1991).
- 19. G. Redmond, D. Fitzmaurice, *J. Phys. Chem.* **97**, 1426 (Feb. 1993).
- 20. G. Boschloo, D. Fitzmaurice, *J. Phys. Chem. B* **103**, 2228 (1999).

- 21. G. Boschloo, D. Fitzmaurice, J. Phys. Chem. B 103, 7860 (1999).
- 22. D. Fitzmaurice, Solar Energy Mater. Solar Cells 32, 289 (1994).
- 23. L. A. Lyon, J. T. Hupp, J. Phys. Chem. 99, 15718 (Oct, 1995).
- 24. H. Lindstrom et al., J. Phys. Chem. B 101, 7710 (1997).
- 25. H. Lindstrom et al., J. Phys. Chem. B 101, 7717 (1997).
- 26. H. Masuhara, S. Kawata, Eds., *Nanophotonics: Integrating Photochemistry, Optics, and Nano/bio Materials*, vol. 1 (Elsevier, San Diego, ed. 1, 2004), vol. 1, 1.
- 27. G. Franco, J. Gehring, L. M. Peter, E. A. Ponomarev, I. Uhlendorf, *J. Phys. Chem. B* **103**, 692 (1999).
- 28. H. van't Spijker, B. O'Regan, A. Goossens, *J. Phys. Chem. B* **105**, 7220 (2001).
- 29. A. Hagfeldt, M. Gratzel, Chem. Rev. 95, 49 (1995).
- 30. N. Kopidakis, K. D. Benkstein, J. van de Lagemaat, A. J. Frank, *J. Phys. Chem. B* **107**, 11307 (Oct, 2003).
- 31. B. Enright, G. Redmond, D. Fitzmaurice, *J. Phys. Chem.* **98**, 6195 (Jun, 1994).
- 32. J. Nelson, *The Physics of Solar Cells*. (Imperial College Press, London, 2003), pp. 9-11.
- 33. ****, To clarify notation used throughout this work: an italicized E denotes potential while a bold \mathbf{E} denotes energy.
- 34. B. Enright, D. Fitzmaurice, *J. Phys. Chem.* **100**, 1027 (1996).
- 35. E. Burstein, *Phys. Rev.* **93**, 632 (1954).
- 36. J. I. Pankove, *Optical Processes in Semiconductors*. (Dover Publications, New York, 1975).
- 37. R. van de Krol, A. Goossens, E. A. Meulenkamp, *J. Appl. Phys.* **90**, 2235 (2001).
- 38. G. Sauve et al., J. Phys. Chem. B 104, 6821 (Jul 27, 2000).
- 39. S. K. Sarkar et al., Journal of Physical Chemistry C 114, 8032 (May, 2010).
- 40. T. W. Hamann, J. W. Ondersma, *Energy Environ. Sci.* **4**, 370 (2011).
- 41. J. Datta, A. Bhattacharya, K. K. Kundu, Bull. Chem. Soc. Jpn. 61, 1735 (1988).

- 42. G. Boschloo, A. Hagfeldt, Acc. Chem. Res. 42, 1819 (2009).
- 43. M. Gratzel, *Inorg. Chem.* 44, 6841 (Oct, 2005).
- 44. A. J. Bard, A. B. Bocarsly, F. R. F. Fan, E. G. Walton, M. S. Wrighton, **102**, 3671 (1980).
- 45. G. Schlichthorl, S. Y. Huang, J. Sprague, A. J. Frank, *J. Phys. Chem. B* **101**, 8141 (1997).
- 46. F. Fabregat-Santiago, I. Mora-Sero, G. Garcia-Belmonte, J. Bisquert, *J. Phys. Chem. B* **107**, 758 (2003).
- 47. D. Kuciauskas *et al.*, *J. Phys. Chem. B* **106**, 9347 (Sep, 2002).
- 48. A. Safrany, R. Gao, J. Rabani, *J. Phys. Chem. B* **104**, 5848 (2000).
- 49. J. Bisquert, V. S. Vikhrenko, *J. Phys. Chem. B* **108**, 2313 (Feb, 2004).
- 50. J. van de Lagemaat, A. J. Frank, J. Phys. Chem. B 104, 4292 (2000).
- 51. A. C. Fisher, L. M. Peter, E. A. Ponomarev, A. B. Walker, K. G. U. Wijayantha, *J. Phys. Chem. B* **104**, 949 (2000).
- 52. L. Dloczik et al., J. Phys. Chem. B 101, 10281 (1997/12/01, 1997).
- 53. S. M. Sze, *The Physics of Semiconductor Devices*. (Wiley, New York, ed. 2nd, 1981).

Chapter 7. Diffusion Limitations in DSSCs Utilizing Outer-Sphere Redox Shuttles: Desirability of Methanol

7.1 Introduction to Diffusion Limitations in DSSCs Utilizing Outer-Sphere Redox Shuttles

The dye sensitized solar cell field recently passed an important milestone; a record efficiency of 12% for DSSCs was achieved without the staple I_3^-/I^- electrolyte system which every previous record cell in the two decades after O'Regan and Gratzel's breakthrough paper.(1, 2) Replacing I_3^-/I^- electrolyte with single electron outer-sphere redox shuttles such as $[Co(bpy)_3]^{3+/2+}$ as the standard system is the culmination of many years work and opens endless possibilities of dye/redox shuttle possibilities. There is, however, one main limitation that still plagues DSSCs utilizing outer-sphere redox shuttles: mass transport limited current densities.

The obvious detriment of lethargic redox shuttle diffusion is the direct limit placed the current density such that $J_{sc} \leq J_{lim}$ which is controlled by:

$$J_{\lim} \propto \frac{[A] pD}{I}$$
 7.1

where [A] is the concentration of the limiting redox shuttle, p is the porosity, D is the diffusion coefficient, and l is the distance the shuttle must diffuse to the counter electrode. An additional limitation diffusion places on DSSC efficiency is through the addition of diffusion resistance, R_d , to the DSSC, which results in a decreased ff. In addition, the resistance associated with slow electron-transfer kinetics at the counter electrode can contribute to a poor ff. In order to demonstrate the effects of these resistances associated with outer-sphere shuttles, electrochemical impedance spectroscopy, EIS, was performed under AM 1.5 illumination (100)

mW cm⁻²) on a DSSC utilizing the $[Co(t-Bu_2bpy)_3]^{3+/2+}$ redox shuttle was fabricated in identical fashion as reported in chapter 2.

A characteristic Nyquist plot resulting from EIS is shown in figure 7.1a. Three overlapping semicircular impedance features are present which are associated with charge transfer at the counter electrode, charge transfer at the photoanode (recombination), and diffusion of the redox species, as labeled in the figure 7.1a. To extract the resistances associated with each process these spectra were fitted to the equivalent circuit introduced in chapter 2.(3) Since a platinized counter electrode is used, R_{Pt} and C_{Pt} represent the charge transfer resistance and the double layer capacitance at the platinized counter electrode respectively. The magnitude of the diffusion resistance, R_d , can be determined from the Warburg element, which is used to describe diffusion, following the equation:

$$Z_d = R_d \frac{\tanh\left[\left(I\omega / \omega_d \right)^{1/2} \right]}{\left(I\omega / \omega_d \right)^{1/2}}$$
 7.2

where ω is the frequency of the ac perturbation, and ω_d (= l^2D_o) is the characteristic frequency of diffusion. The R_d values obtained from EIS, displayed in figure 7.1b, show how the mass transport resistance decreases as the current decreases as expected. Due to the poor electron-transfer kinetics between $[\text{Co}(t-\text{Bu}_2\text{bpy})_3]^{3+/2+}$ and platinum, the charge transfer resistance at the platinized counter electrode, R_{Pt} , is another significant source of resistance. Values of R_{Pt} varied slightly with electrode preparation conditions, but were generally in the range of 70-100 Ω . Choosing an alternative material for the counter electrode can minimize R_{Pt} . For example, gold and poly(3,4-ethylenedioxythiophene), PEDOT, have been found to exhibit faster kinetics than platinum with such cobalt complexes and are thus often uses as the counter electrode material.(4-10)

The J-V curve of the DSSC investigated with EIS is displayed in figure 7.1c. The fill factor is 0.49, consistent with what has been previously reported.(4, 5, 7, 8, 11-13) The J-V curve can be corrected for the two resistance losses, R_d and R_{Pt} , by subtracting the ohmic drop, IR, from the applied potential, V_{app} , according to $V_{corr} = V_{app} - IR$. The resultant J- V_{corr} curve is displayed in figure 7.1c). After correcting for R_{Pt} and R_d , an increase in the ff from 0.49 to 0.7 is produced. Overcoming these resistive processes would thus represent an improvement in efficiency of 43%. The series resistance of ~45 Ω was not included in the correction since that is not necessarily a result of the redox shuttle, but most likely a general feature of cell design / fabrication. Further corrections including the series resistance would bring the ff close to the ideal value of ~0.8, consistent with a diode quality factor close to 1.

The mass transport limitation for metal tris(bi-pyridyl) redox shuttles results from a combination of lower diffusion coefficients and lower solubility than I_3^-/I^- in acetonitrile: the standard solvent system used. One way to overcome the mass transport problem is through the use of more polar solvents which increases the solubility of charged redox shuttles. Before DSSCs can be rationally designed to work well with solvents other than the conventional acetonitrile, any effect on the energetics and kinetics of DSSC operation must be determined.

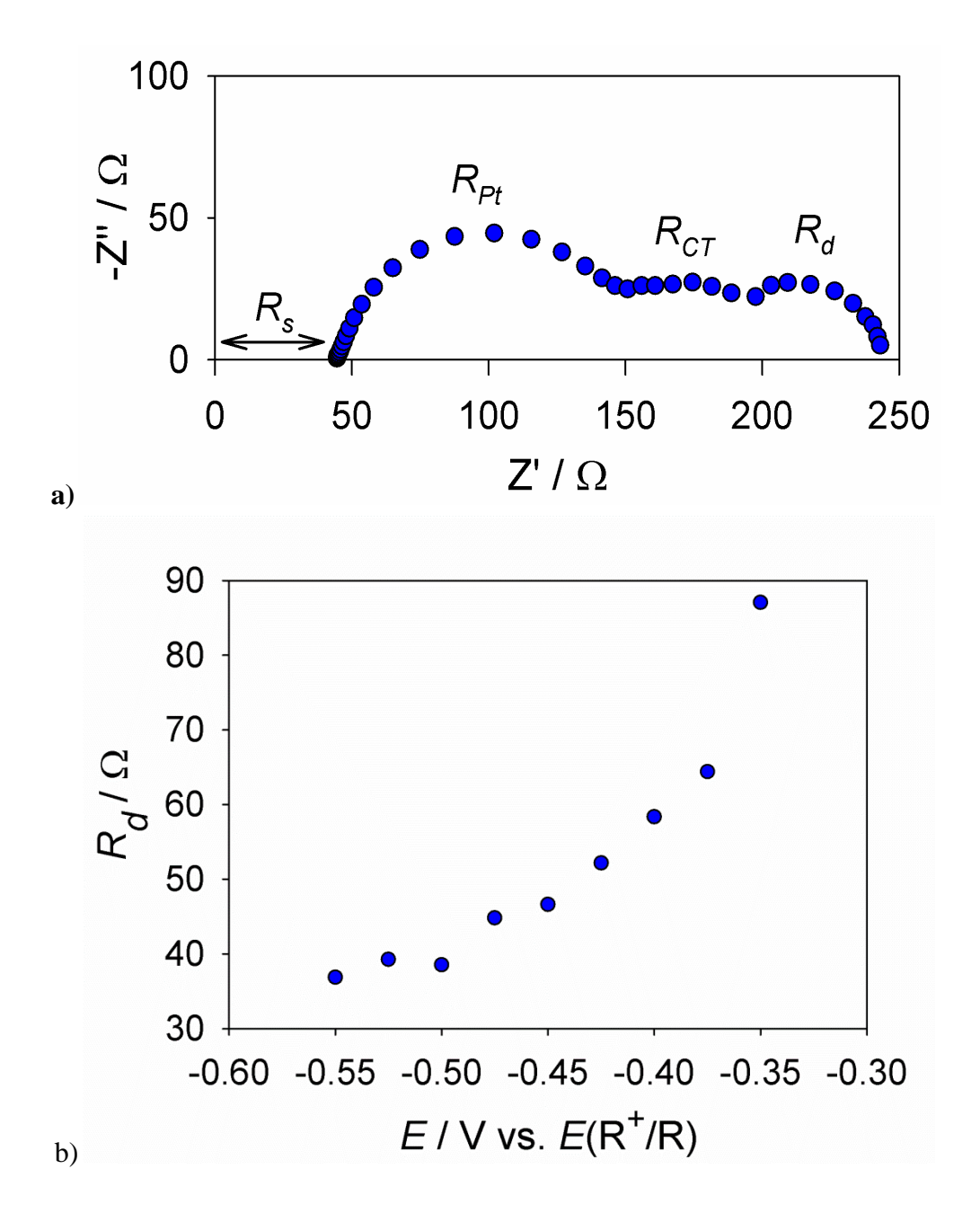
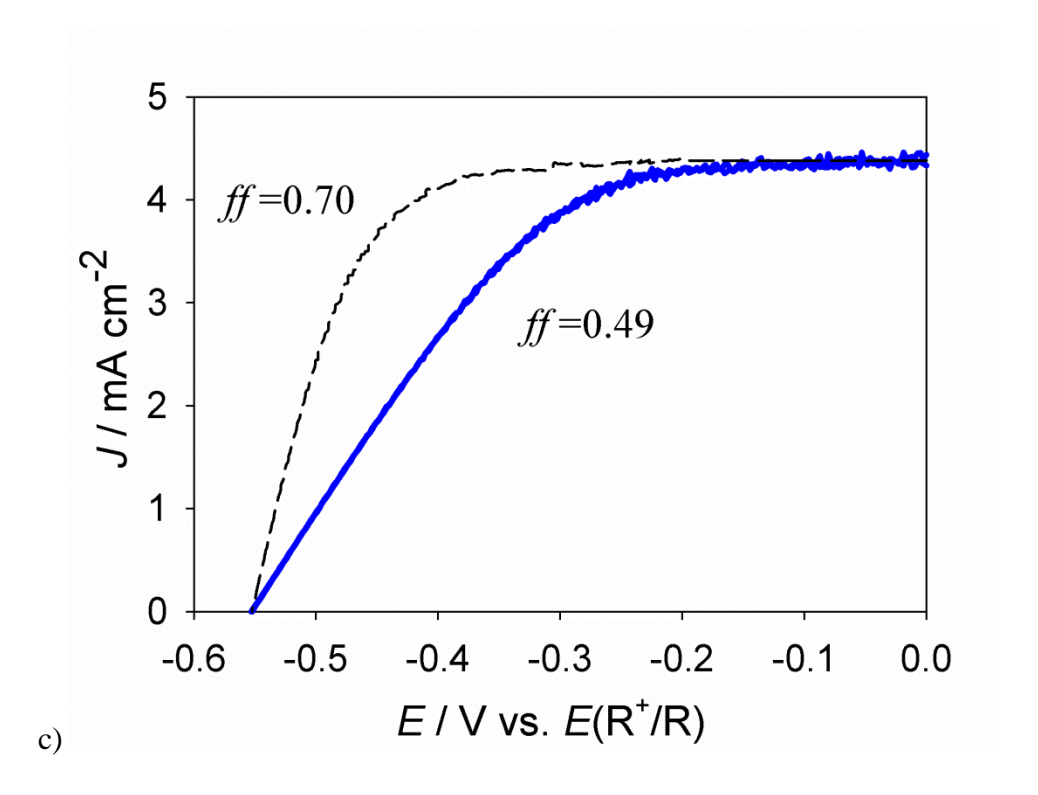


Figure 7.1: Experimental results for an N3 sensitized TiO₂ nanoparticle based DSSC utilizing $[\text{Co}(t-\text{Bu}_2\text{bpy})_3]^{3+/2+}$ as a redox shuttle. a) EIS spectrum taken at -0.425 V vs. $E(R^+/R)$ showing each resistive element. b) Extracted R_d values taken between P_{max} and V_{oc} . c) Experimental (blue solid) *J-V* curve and a *J-V*_{corr} curve correcting for R_d and R_{Pt} (135Ω total correction, black dashed line), with the resulting improvement in ff indicated.

Figure 7.1 (Cont'd):



The conduction band energy, \mathbf{E}_{cb} , the potential of the redox shuttle, E_{redox} , the ground state potential, E° , and the excited state potential, $E^{\circ*}$, of the dye can all shift as the dielectric of the solvent changes. The work presented in this chapter demonstrates the shifts in energetics and the ensuing changes in kinetics which must be accounted for when changing the DSSC solvent from acetonitrile to methanol.

7.2 DSSC Performance in Methanol

Figure 7.2 shows the steady state current density, J, versus potential of two DSSCs utilizing the dye Z907 and the redox couple $[\text{Co}(t-\text{Bu}_2\text{bpy})_3]^{3+/2+}$ dissolved in one of two different solvents: acetonitrile or methanol. Despite the identical construction of the DSSCs, other than solvent, there is a large discrepancy in device performance. When moving from

acetonitrile to methanol, the short circuit current density, J_{sc} , decreased by half from 9.8 to 4.9 mAcm⁻² while the open-circuit voltage increased from 0.51 to 0.59 V. While the J–V curve shown provides the key parameters needed to calculate the efficiency of the DSSC, it does not provide diagnostic information on why the performance of these cells differs. A change in solvent polarity would be expected to affect many of the energetics in a DSSC. Determining the change in energetics of the DSSC, and the resulting change in kinetics of operation, will provide insight into the difference in performance and guide future work.

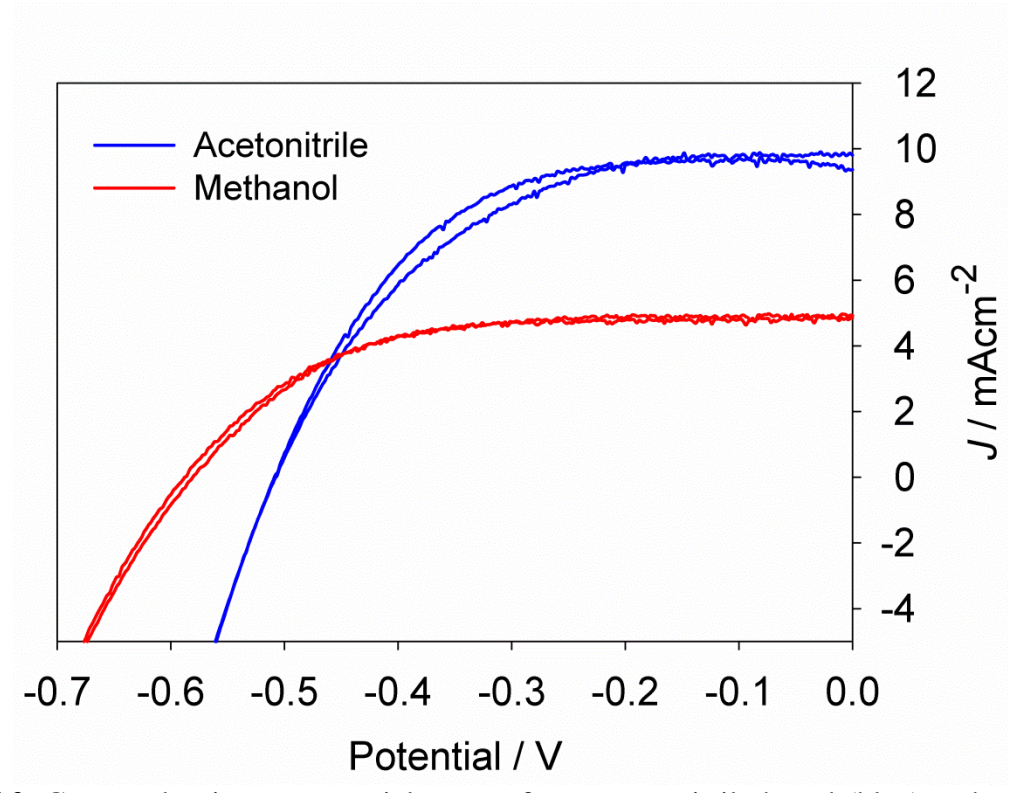
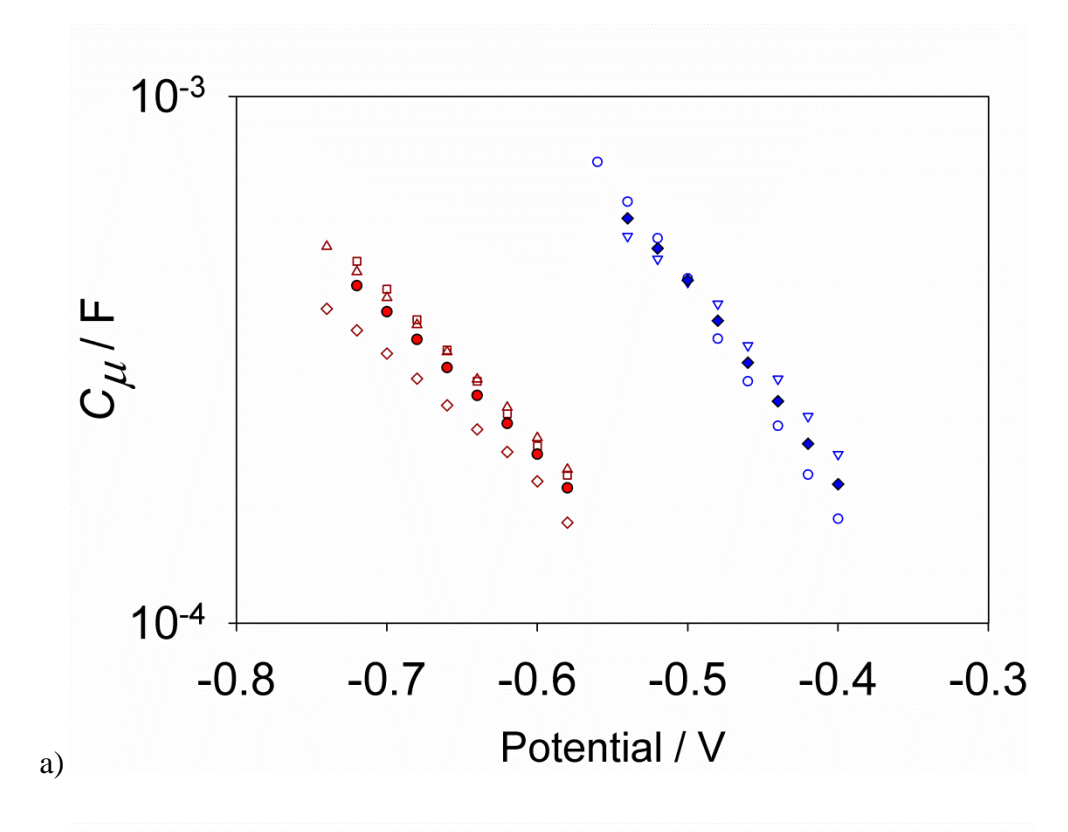


Figure 7.2. Current density vs. potential curves for an acetonitrile based (blue) and a methanol based (red) DSSCs, both using the same dye and redox shuttle as described in text.

7.3 Energetic and Kinetic Considerations for Methanol Based Dye Sensitized Solar Cells

7.3.1 Effect of Methanol on TiO₂ Energetics

A large effect on DSSC performance would be expected if the band energies of TiO₂ were to shift.(14) Electrochemical impedance spectroscopy, EIS, was employed to determine if the conduction band of TiO₂ shifts when the solvent is changed to methanol. Since the EIS measurements were made using full working DSSCs, the potential referenced is the solution potential and not a standard reference potential. Consequently, before any comparisons can be made using the EIS results the shift of the solution potential with solvent must be known. To this end cyclic voltammetry was performed on $\left[\text{Co}(t\text{-Bu}_2\text{bpy})_3\right]^{3+/2+}$ in both acetonitrile and methanol using decamethylferrocene as an internal reference. Taking into account an 80 mV shift in the potential of decamethylferrocene between solvents, the change in potential of [Co(t- $[Bu_2bpy)_3]^{3+/2+}$ was found to be < 5 mV and thus neglected.(15) Both C_μ and R_T depend on \mathbf{E}_{cb} and were measured using EIS on full working DSSCs using $\left[\text{Co}(t-\text{Bu}_2\text{bpy})_3\right]^{3+/2+}$ with either acetonitrile or methanol, displayed in figure 3(b) and (c). C_{μ} is proportional to the density of states in TiO_2 and thus shifts concomitantly with the conduction band energy. R_T depends on the occupancy of trap states (determined by the difference between E_{cb} and the quai-Fermi level) manifesting as an exponential dependence of R_T with potential. The results shown in figure 7.3(b) and 3(c) demonstrate that both C_{μ} and R_{T} shift negative by roughly 200 mV when moving from acetonitrile to methanol, indicating that the conduction band shifts approximately 200 meV higher in energy (negative in potential), similar to the shift reported for bare TiO2 films by Redmond and Fitzmaurice using a spectroelectrochemical method. (16)



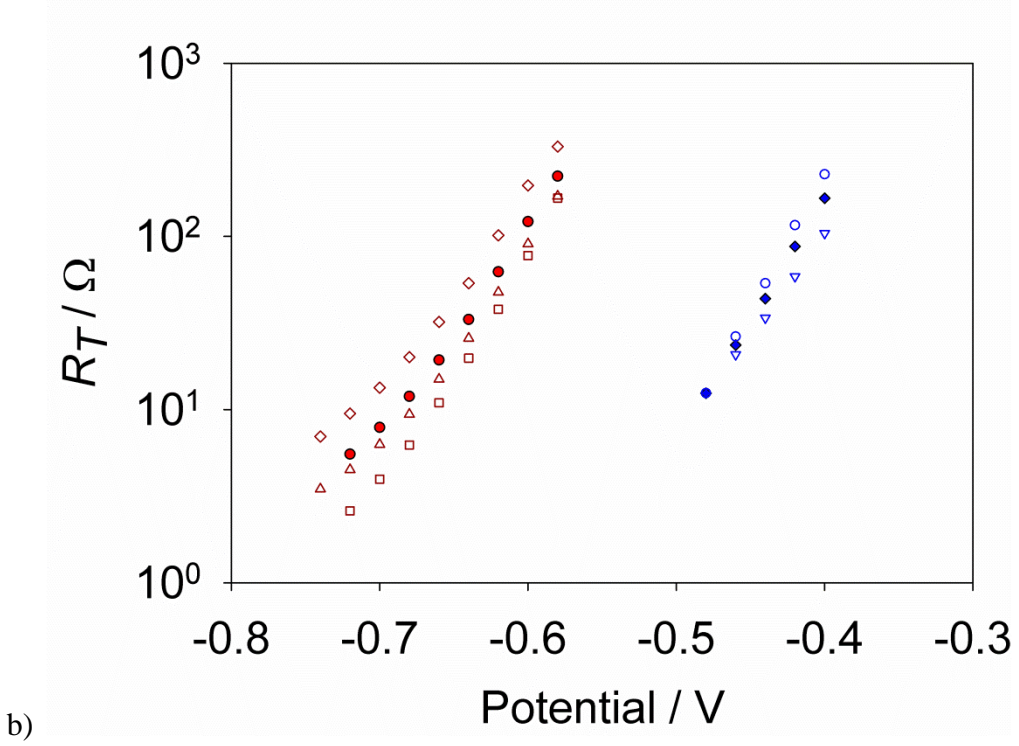


Figure 7.3. a) Comparison of chemical capacitance, C_{μ} , and b) transport resistance, R_T , in acetonitrile (blue) and methanol (red) based DSSCs. Open symbols represent individual cell data while solid symbols represent averages.

7.3.2 Effect of Methanol on TiO₂ Recombination Kinetics

EIS also provides information on the rate of back electron transfer from TiO_2 to $[Co(t-Bu_2bpy)_3]^{3+}$ through the charge transfer resistance R_{CT} , shown in figure 7.4(a). R_{CT} in the methanol based DSSC is larger at a given potential than for the acetonitrile based DSSC indicating a slower rate of recombination in the methanolic cell as R_{CT} is inversely related to the recombination rate $U(E_F)$:

$$\frac{1}{R_{CT}} \propto U(E_F) = k[A] n_{cb}(E_F)$$
7.3

where [A] is the concentration of electron acceptor in solution, n_{cb} is the concentration of electrons in the conduction band of TiO₂, and k is the electron transfer rate constant.(17) For DSSCs using $[\text{Co}(t-\text{Bu}_2\text{bpy})_3]^{3+/2+}$, recombination has been shown to overwhelmingly originate from the conduction band rather than surface states; k in this chapter will thus specifically denote the rate constant for electron transfer from the conduction band.(17) Both n_{cb} and k depend on \mathbf{E}_{cb} as:

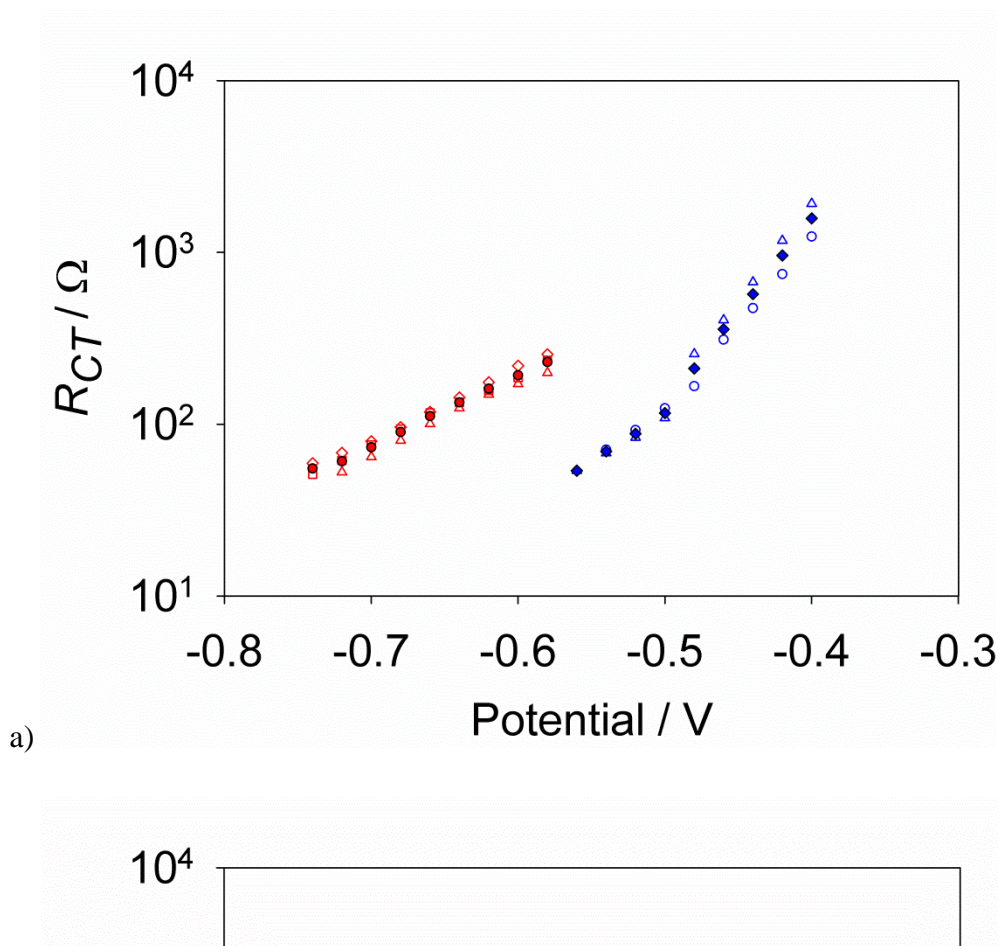
$$n_{cb} = N_c \exp\left(\frac{\mathbf{E}_{cb} - qE_F}{k_B T}\right)$$
 7.4

and

$$k = k_{\text{max}} \exp \left[\frac{-\left(\mathbf{E}_{cb} - qE_{redox} + \lambda\right)}{4\lambda k_B T} \right]$$
 7.5

where N_c is the total density of electrons in the conduction band of TiO₂, k_B is the Boltzmann constant, T is temperature, λ is the reorganization energy, and k_{max} is the rate constant of electron transfer at maximum exoergicity.(18, 19)

The 200 mV negative shift of \mathbf{E}_{cb} has two opposing effects. First, resulting from equation 7.4, n_{cb} decreases as \mathbf{E}_{cb} – qE_F increases resulting in a decrease in the recombination rate. Second, following equation 7.5, k increases as \mathbf{E}_{cb} – E_{redox} increases resulting in an increase in the recombination rate. The increase in k can be verified by plotting R_{CT} for both cells versus C_{μ} , shown in figure 7.4b. Here, the recombination rate can be compared when both cells have similar concentrations of electrons in the TiO_2 since C_{μ} is dependent on \mathbf{E}_{cb} – qE_F . As expected for Marcus normal behavior the methanolic DSSC, with a higher energy \mathbf{E}_{cb} , shows smaller values of R_{CT} , indicating faster recombination. However, the decrease in n_{cb} has a larger effect on the resulting R_{CT} than the increase in k due to the 4λ in the denominator of the exponential in equation 7.5 explaining the decrease in recombination rate at a given potential, as observed in figure 7.4a. The competition of these effects explains why the shift in R_{CT} is smaller than the 200 mV shift observed for both R_T and C_{μ} . The increase in R_{CT} ultimately results in the increase in V_{oc} on the J–V curves shown in figure 7.2.



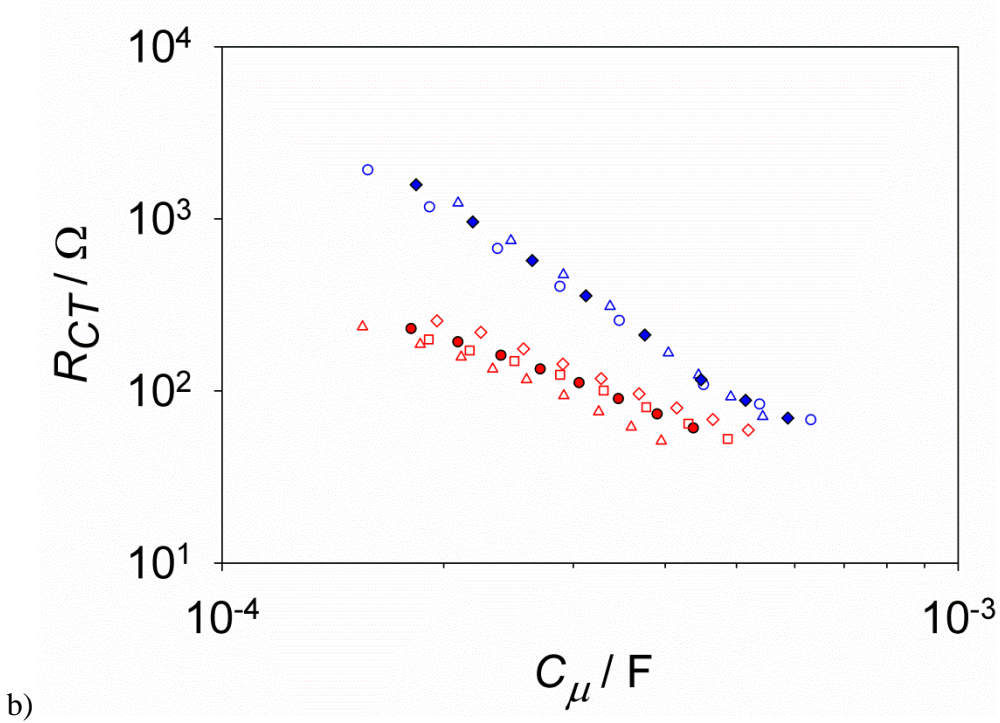


Figure 7.4. Comparison of charge transfer resistance, R_{CT} , a) vs. potential and b) vs. C_{μ} in acetonitrile (blue) and methanol (red) based DSSCs. Open symbols represent individual data while solid symbols represent averages.

7.3.3 Effect of Methanol on Dye Energetics

Cyclic voltammetry was carried out to determine if there is a shift in the energetics of the Z907 dye between solvents. The $E_{1/2}$ for Z907 shifted approximately +50 mV from acetonitrile to methanol. To determine if a shift in the dye excited state occurred, both absorbance and emission spectra of Z907 were taken in both solvents, shown in figure 7.5. The HOMO-LUMO gap can be quickly estimated by the intersection of the normalized absorbance and emission spectra. The intersection of these spectra was found to be nearly identical at 700 nm, indicating a similar HOMO-LUMO gap of ~1.77 eV in either acetonitrile or methanol. Considering the slight positive shift of the ground state of Z907 in methanol the excited state is predicted to shift approximately the same amount.

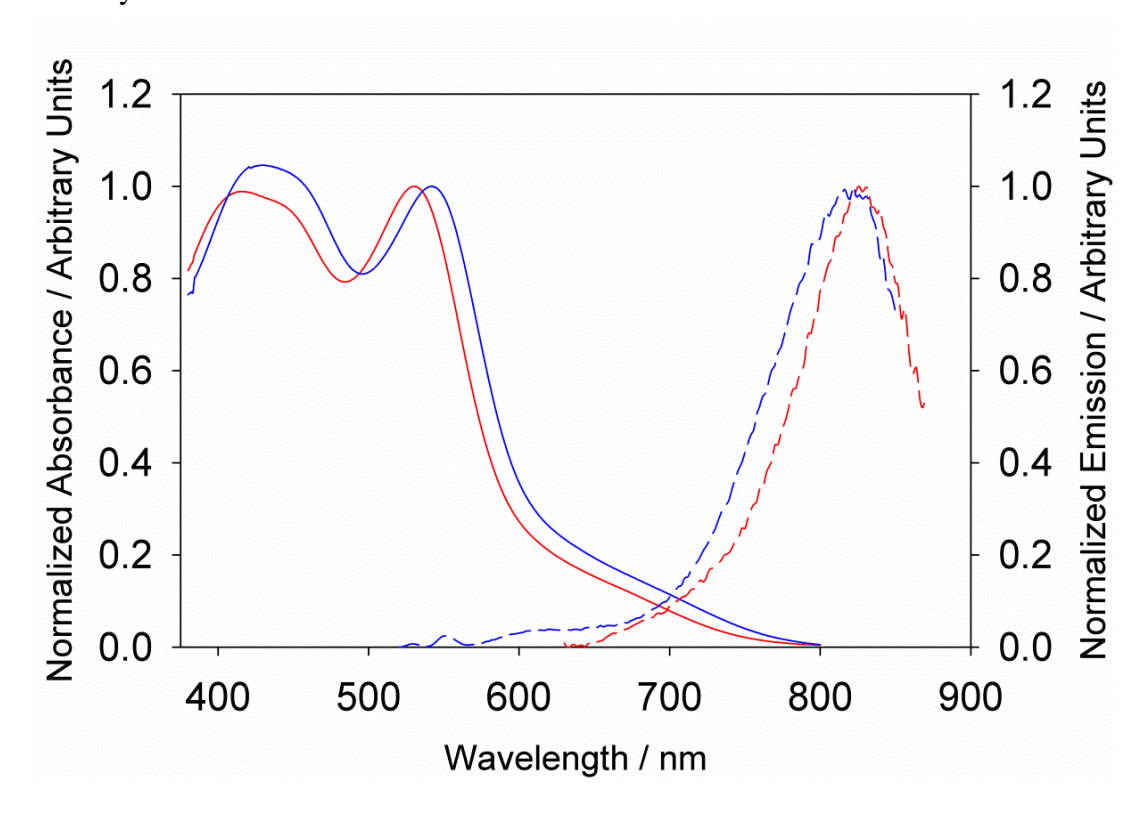


Figure 7.5. Normalized absorbance (solid) and emission (dashed) spectra of Z907 in acetonitrile (blue) and methanol (red).

A summary of the energetic changes of each important DSSC parameter are shown in figure 7.6. The main effects methanol has on DSSC energetics are the negative shift in the TiO_2 conduction band and a slight positive shift of the dye's E° and $E^{\circ*}$. These energetic changes result in a decreased driving force for injection by ~250 meV. DSSC's using Z907 in methanol will thus be predicted to suffer from low injection yields.

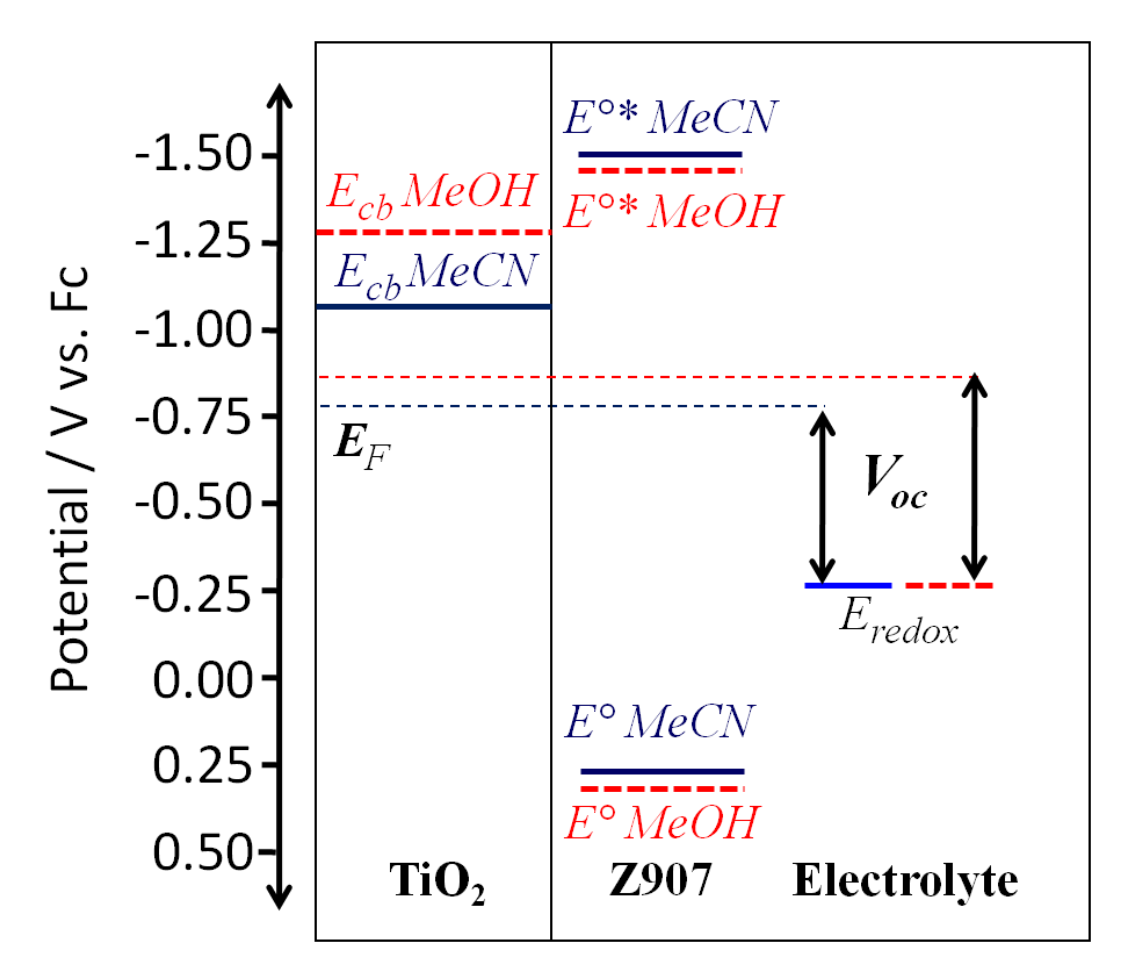


Figure 7.6. Energy diagram showing changes in energetics in a dye-sensitized solar cell when the solvent is changed from acetonitrile to methanol.

7.4 Increased Concentration of [Co(t-Bu₂bpy)₃]³⁺ in Methanol

Typical cobalt tris-bipyridyl based DSSCs use a concentration of Co(III) near 20 mM which is near the solubility limit for many of these complexes in acetonitrile. To investigate the

possible effect on Jlim by increasing the concentration of oxidized shuttle, a series of methanol based DSSCs were constructed with concentrations of 20, 40, and 80 mM $[Co(t-Bu_2bpy)_3]^{3+}$. Since injection was determined to be a limiting process as discussed above, higher light intensities were used to simulate currents that may result from DSSCs with increased injection efficiency. The mass transport limiting current density results for DSSCs with varying concentrations of $[Co(t-Bu_2bpy)_3]^{3+}$ and varying light intensities are shown in figure 7.7. As shown, increasing the concentration of $[Co(t-Bu_2bpy)_3]^{3+}$ above the typically used 20 mM does result in increased J_{lim} . DSSCs with 40 mM $[Co(t-Bu_2bpy)_3]^{3+}$ display the highest current over most light intensity ranges; at very high light intensity ranges however 80 mM $[Co(t-Bu_2bpy)_3]^{3+}$ displays the highest current.

Since recombination increases linearly with the concentration of $[Co(t-Bu_2bpy)_3]^{3+}$ as shown in equation 7.3, the DSSC with the highest concentration of 80 mM $[Co(t-Bu_2bpy)_3]^{3+}$ has a lower current under most light intensities than that with 40 mM $[Co(t-Bu_2bpy)_3]^{3+}$. This trend ends when the light is increased to high intensities and the DSSC with 40 mM $[Co(t-Bu_2bpy)_3]^{3+}$ becomes mass transport limited and the electron injection rates are high enough to make recombination negligible.

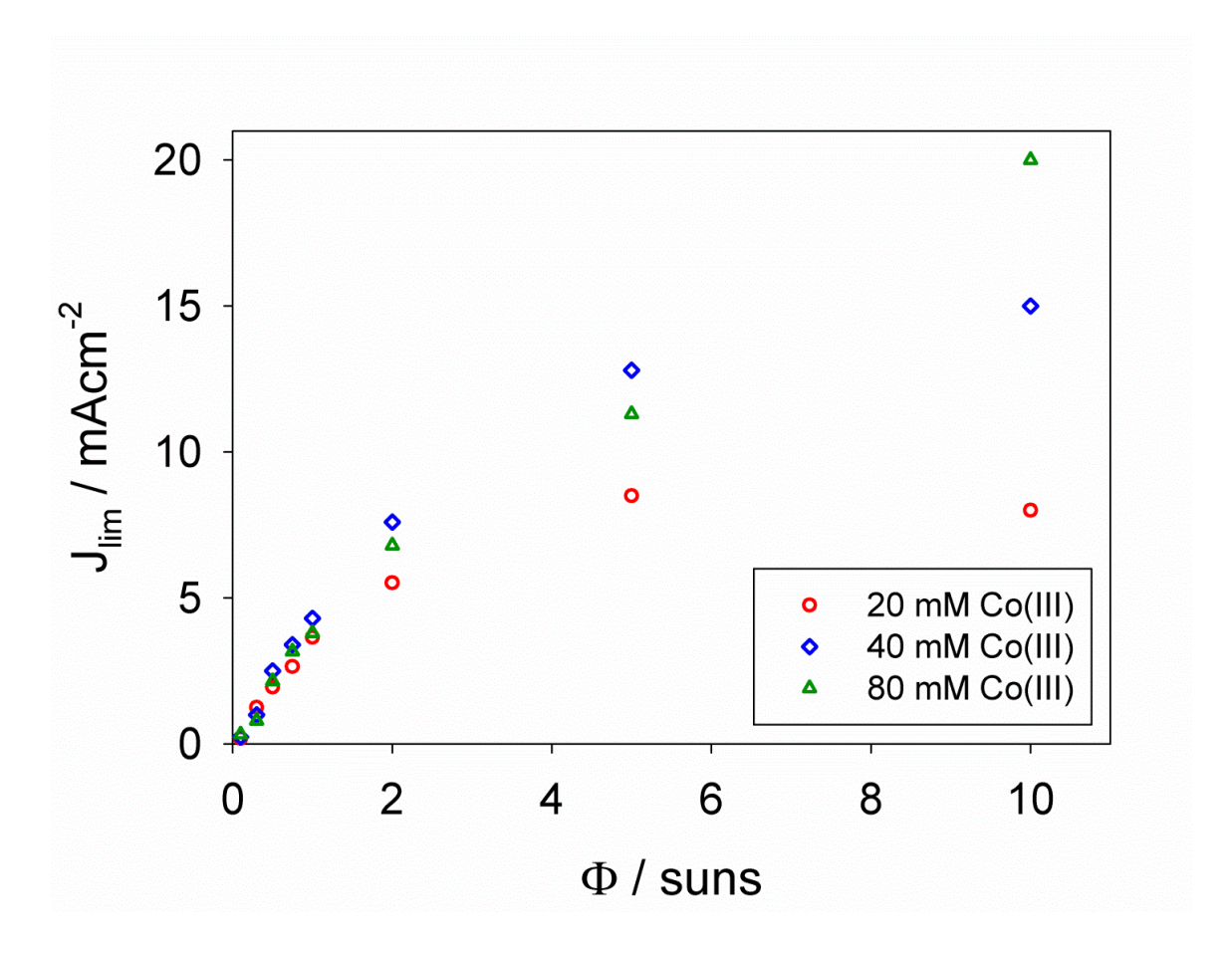


Figure 7.7. Mass transport limiting current density, J_{lim} , in methanol with varying concentration of $[\text{Co}(t\text{-Bu}_2\text{bpy})_3]^{3+}$ and light intensity. Light intensities used were 0.1, 0.25, 0.5, 0.75, 1.0, 2.0, 5.0, 10 suns, with 1 sun representing 100 mWcm⁻² illumination with the AM1.5G spectrum.

7.5 Conclusion

Although using methanol as a solvent in DSSCs allows an increased concentrations of $[\text{Co}(t-\text{Bu}_2\text{bpy})_3]^{3+/2+}$ to remove mass transport limitations; the DSSCs demonstrated lower efficiency. The cause of the lower performance was indicated to be a decreased electron injection efficiency brought about by a decreased driving force for injection as \mathbf{E}_{cb} increased approximately 200 meV while the excited state of Z907 decreased by ~50 meV. Before efficient DSSCs can be produced using methanol as a solvent to take advantage of the increased solubility and decreased toxicity this problem of injection driving force must be overcome. There are two

ways in which this could be accomplished: either developing new dyes with higher excited states or using a semiconductor with a lower \mathbf{E}_{cb} in methanol.

Dyes designed to work well in methanol with TiO₂ must contain both a higher energy excited state and ligands designed to decrease recombination resulting from high concentrations of electron acceptor in solution. Such dyes, when used to make methanol based DSSCs, would be predicted to achieve higher currents than what have been obtained in acetonitrile based DSSCs as the mass transport limitation can be overcome.

7.6 Experimental

Lithium Chloride (ultra dry, 99.9% metals basis, Alfa Aesar) and methanol (anhydrous, Sigma Aldrich) were stored under inert atmosphere and used as received. Lithium perchlorate (battery grade, Sigma Aldrich) and cis-Bis(isothiocyanato)(2,2'-bipyridyl-4,4'-dicarboxylato)(4,4'-di-nonyl-2'-bipyridyl)ruthenium(II) (Z907, Sigma Aldrich) were used as received. The cobalt redox couple, cobalt(II) tris(4,4'-di-tert-butyl-2,2'-bipyridyl) hexafluorophosphate, [Co(t-Bu₂bpy)₃](PF₆)₂, was prepared as described in chapter 2.

Cobalt(III) tris(4,4'-di-*tert*-butyl-2,2'-bipyridyl) hexafluorophosphate, [Co(*t*-Bu₂bpy)₃](PF₆)₃, was prepared as follows. To a stirring solution of [Co(*t*-Bu₂bpy)₃](PF₆)₂ in minimal acetonitrile, 1.2 equivalents of NOPF₆ dissolved in minimal acetonitrile was added slowly. The solution was allowed to stir for 30 minutes before being rotary evaporated dry. The solid was re-dissolved in minimal acetonitrile, precipitated with diethyl ether, collected via vacuum filtration and washed with methanol, water, and diethyl ether. The resulting [Co(*t*-Bu₂bpy)₃](PF₆)₃ was used after re-crystallizing from acetonitrile using diethyl ether and drying under vacuum. Elemental analysis calculated for [Co(*t*-Bu₂bpy)₃](PF₆)₃: C, 49.91; H, 5.59; N, 6.47. Found: C, 49.66; H, 5.68; N, 6.42.

Cobalt(II) tris(4,4'-di-*tert*-butyl-2,2'-bipyridyl) chloride, [Co(*t*-Bu₂bpy)₃]Cl₂, was prepared as follows. CoCl₂•6H₂O was dissolved in minimal methanol; to this a solution of 3.1 equivalents 4,4'-di-*tert*-butyl-2,2'-bipyridyl in a 1:1 mixture of methanol:isopropanol was added and the solution was allowed to stir for 2 hours. The reaction mixture was rotary evaporated dry and dissolved into minimal methanol. An equivalent amount of diethyl ether was added dropwise to form a precipitant. The precipitant was collected via vacuum filtration and washed with diethyl ether. Elemental analysis calculated for 4•H₂O[Co(*t*-Bu₂bpy)₃]Cl₂: C, 64.38; H, 8.01; N, 8.35%. Found: C, 64.20; H, 7.74; N, 8.29%.

Cobalt(III) tris(4,4'-di-*tert*-butyl-2,2'-bipyridyl) chloride, [Co(*t*-Bu₂bpy)₃]Cl₃, was prepared as follows. [CoCl(NH₃)₅](Cl)₂ was dissolved in water, to which an equal volume of a solution of 3.1 mol eq. 4,4'-di-*tert*-butyl-2,2'-bipyridyl in isopropanol. The reaction mixture was brought to reflux for 12 hours during which time the mixture turned brown. The reaction mixture was rotary evaporated dry and dissolved in methanol. A small amount of gray precipitant remained and was removed by vacuum filtration. The filtrate was dried by rotary evaporation and recrystallized in methanol revealing a yellow powder. Elemental analysis: Calculated for 2•H₂O[Co(*t*-Bu₂bpy)₃]Cl₃: C, 64.42; H, 7.61; N, 8.35. Found: C, 64.33; H, 8.19; N, 8.45.

DSSC Fabrication

Cleaned fluorine-doped tin oxide (FTO) coated glass was coated with a blocking layer of TiO₂ via atomic layer deposition using 500 cycles of titanium isopropxide (99.999% trace metals basis, Sigma-Aldrich) and water with a Savannah 200 instrument (Cambridge Nanotech Inc) were prepared as described in chapter 2. A transparent TiO₂ nanoparticle layer was prepared by doctor blading a paste of ~10-20 nm TiO₂ nanoparticles (Ti-Nanoxide T/SP, Solaronix) one scotch tape thickness on the TiO₂ coated FTO-glass substrate. This layer was allowed to relax

for 10 min at room temperature and 15 minutes at 90 °C before overlaying a scattering TiO_2 nanoparticle layer prepared by doctor blading a paste of > 100 nm TiO_2 nanoparticles (Ti-Nanoxide D20/SP, Solaronix). The electrodes where then annealed by heating in air to 325 °C for 5 min, 375 °C for 5 min, 450 °C for 5 min and 500 °C for 15 min. A blocking layer of Al_2O_3 was applied via atomic layer deposition as described in chapter 2 and the resulting electrodes were annealed again in air to 500 °C for 30 min. The electrodes where allowed to cool to a temperature of 90 °C before being immersed in an ethanolic solution of 0.3 mM Z907 and soaked overnight at 2-3 °C. The TiO_2 film thickness was measured using a Dektak3 Surface Profiler to be 8 μ m of transparent TiO_2 and 4 μ m of scattering TiO_2 .

Due to slow electron transfer kinetics observed for the standard platinum based counter electrode with cobalt tris-bipyridyl complexes, poly(3,4-ethylenedioxythiophene) (PEDOT) counter electrodes were used.(9) PEDOT based counter electrodes were fabricated according to literature techniques.(20) Fluorine-doped tin oxide coated glass (FTO, Tec-9, Pilkington) was cleaned by sequential sonication in Alconox, deionized water, acetone and isopropanol before being heated to 400° C for 20 min. The PEDOT films were then prepared by electropolymerization of the 3,4-ethylenedioxythiophene (EDOT) monomer on FTO using a solution of 0.1 M LiClO4 and 0.02 M EDOT in acetonitrile. The potential of the FTO was scanned at a rate of 50 mV/s over the range -0.6 to 1.4 V vs. Ag/AgCl (0 V \rightarrow 1.4 V \rightarrow -0.6 V \rightarrow 0 V vs. Ag/AgCl) twice while rapidly stirring the solution. The electrodes where then soaked in acetonitrile for 5 min to remove monomers or oligomers from the PEDOT film, rinsed with acetonitrile and allowed to dry.

Sandwich DSSCs were fabricated by sandwiching a $\sim 25~\mu m$ thick Surlyn frame (Solaronix) between the photoanode and the PEDOT coated counter electrode with light pressure

at 140 °C to seal the cell. Electrical contact was achieved using copper wire and conductive silver epoxy after lightly scratching through the blocking layer to expose the FTO substrate. Electrolyte was loaded though two holes in the counter electrode by capillary force to avoid using the typical vacuum filling method and any uncertainty in electrolyte concentration that may result from placing volatile solvents under vacuum.

For DSSCs used in figures 7.1-7.4: Acetonitrile based electrolyte for sandwich cells contained 0.2 M [Co(t-Bu₂bpy)₃](PF₆)₂, 0.02 M [Co(t-Bu₂bpy)₃](PF₆)₃, and 0.1 M LiClO₄. Methanol based electrolyte for sandwich cells contained 0.2 M [Co(t-Bu₂bpy)₃](Cl)₂, 0.02 M [Co(t-Bu₂bpy)₃](Cl)₃, and 0.1 M LiCl. Sandwich cells were aged overnight before use allowing for stable measurements free from time dependent effects observed in the first 12-18 hours after the electrode is placed in contact with the electrolyte.(21) For DSSCs used in figure 7.5: Electrolyte for sandwich cells contained 0.2 M [Co(t-Bu₂bpy)₃](PF₆)₂, 0.1 M LiClO₄, and either 0.02, 0.04, or 0.08 M [Co(t-Bu₂bpy)₃](PF₆)₃.

Electrochemical Measurements

Photoelectrochemical measurements were performed using a Gamry Reference 600 potentiostat interfaced with a Xe Arc Lamp. An AM 1.5 solar filter was used to simulate sunlight at 100 mW cm⁻² or as stated in text. An additional 400 nm long-pass filter was used to prevent direct excitation of the TiO₂ in all light measurements. Electrochemical impedance spectroscopy (EIS) was performed in the light for the measurements displayed in figure 7.1 and in the dark for the remaining measurements. Cyclic voltammetry, CV, performed in methanol and acetonitrile used tetrabutylammonium chloride and tetrabutylammonium hexafluorophosphate as supporting electrolytes respectively. All EIS and CV measurements were made using an Autolab PGSTAT 126N.

REFERENCES

REFERENCES

- 1. B. O'Regan, M. Gratzel, *Nature* **353**, 737 (Oct, 1991).
- 2. A. Yella et al., Science **334**, 629 (2011).
- 3. F. Fabregat-Santiago, J. Bisquert, G. Garcia-Belmonte, G. Boschloo, A. Hagfeldt, *Sol. Energy Mat. Sol. Cells* **87**, 117 (2005).
- 4. M. J. DeVries, M. J. Pellin, J. T. Hupp, *Langmuir* **26**, 9082 (Jun, 2010).
- 5. J. J. Nelson, T. J. Amick, C. M. Elliott, J. Phys. Chem. C 112, 18255 (Nov, 2008).
- 6. C. M. Elliott, S. Caramori, C. A. Bignozzi, *Langmuir* **21**, 3022 (Mar, 2005).
- 7. P. J. Cameron, L. M. Peter, S. M. Zakeeruddin, M. Gratzel, *Coord. Chem. Rev.* **248**, 1447 (Jul, 2004).
- 8. S. A. Sapp, C. M. Elliott, C. Contado, S. Caramori, C. A. Bignozzi, *J. Am. Chem. Soc.* **124**, 11215 (Sep, 2002).
- 9. H. N. Tsao et al., Energy and Environ. Sci. 4, 4921 (2011).
- 10. S. Ahmad *et al.*, *Phys. Chem. Chem. Phys* **14**, 10631 (2012).
- 11. J. W. Ondersma, T. W. Hamann, J. Phys. Chem. C 114, 638 (Jan, 2010).
- 12. B. M. Klahr, T. W. Hamann, *J. Phys. Chem. C* **113**, 14040 (Aug, 2009).
- 13. H. Nusbaumer, S. M. Zakeeruddin, J. E. Moser, M. Gratzel, *Chem.-Eur. J.* **9**, 3756 (Aug, 2003).
- 14. S. A. Haque *et al.*, *J. Phys. Chem. B* **104**, 538 (Jan, 2000).
- 15. I. Noviandri et al., J. Phys. Chem. B 103, 6713 (1999).
- 16. G. Redmond, D. Fitzmaurice, *J. Phys. Chem.* **97**, 1426 (Feb, 1993).
- 17. J. W. Ondersma, T. W. Hamann, J. Am. Chem. Soc. 133, 8264 (2011).
- 18. T. W. Hamann, F. Gstrein, B. S. Brunschwig, N. S. Lewis, *J. Am. Chem. Soc.* **127**, 7815 (Jun 1, 2005).

- 19. T. W. Hamann, F. Gstrein, B. S. Brunschwig, N. S. Lewis, *J. Am. Chem. Soc.* **127**, 13949 (Oct 12, 2005).
- 20. H. Tian, Z. Yu, A. Hagfelt, L. Kloo, L. Sun, J. Am. Chem. Soc. 133, 9413 (2011).
- 21. J. W. Ondersma, T. W. Hamann, J. Phys. Chem. C 114, 638 (2010).

Chapter 8. Future Directions for DSSCs

8.1 Ionic Liquids

Following the rise of dyes with blocking groups to hinder recombination to oxidized redox shuttles in solution, the main obstacle facing dye-sensitized solar cells using outer-sphere redox shuttles is mass transport limitations. This limitation can be overcome with creative solutions. One such possibility was discussed in depth in chapter 7: using an alternative solvent with higher solubility. Using methanol, while overcoming the scientific problem of mass transport, does not overcome the engineering problem of encasing a volatile solvent in a product that must be designed to last for a decade, withstanding large temperature fluctuations.(1) An alternative to volatile solvents are ionic liquids which have been investigated in DSSCs over the past decade.(1-4) Due to the early success of the I_3^-/I^- redox shuttle and the ease in which iodide forms ionic liquids, the ionic liquids that have been used in DSSCs are iodide based. As discussed in detail the I₃-/I- electrolyte has a built in voltage restraint, limiting the maximum obtainable efficiency. To date, to the best of my knowledge, there are no literature reports of electrolytes based on outer sphere redox shuttles incorporated into ionic liquids in DSSCs. In theory ionic liquids could provide a route to very high concentrations of outer sphere redox shuttles and also solve the engineering dilemma of sealing volatile electrolytes in commercial DSSCs.

[Co(bpy)₃]^{3+/2+} when complexed with the bis(trifluoromethylsulfonyl)imide, TFSI, anion can be dissolved in the ionic liquid butyltrimethylammonium bis(trifluoromethylsulfonyl)imide. Using only these components to form an electrolyte, a DSSC with nearly 10 % IPCE can be readily constructed as displayed in figure 8.1. This may seem

low, however early attempts to use cobalt based redox shuttles also had very low device performance.(5)

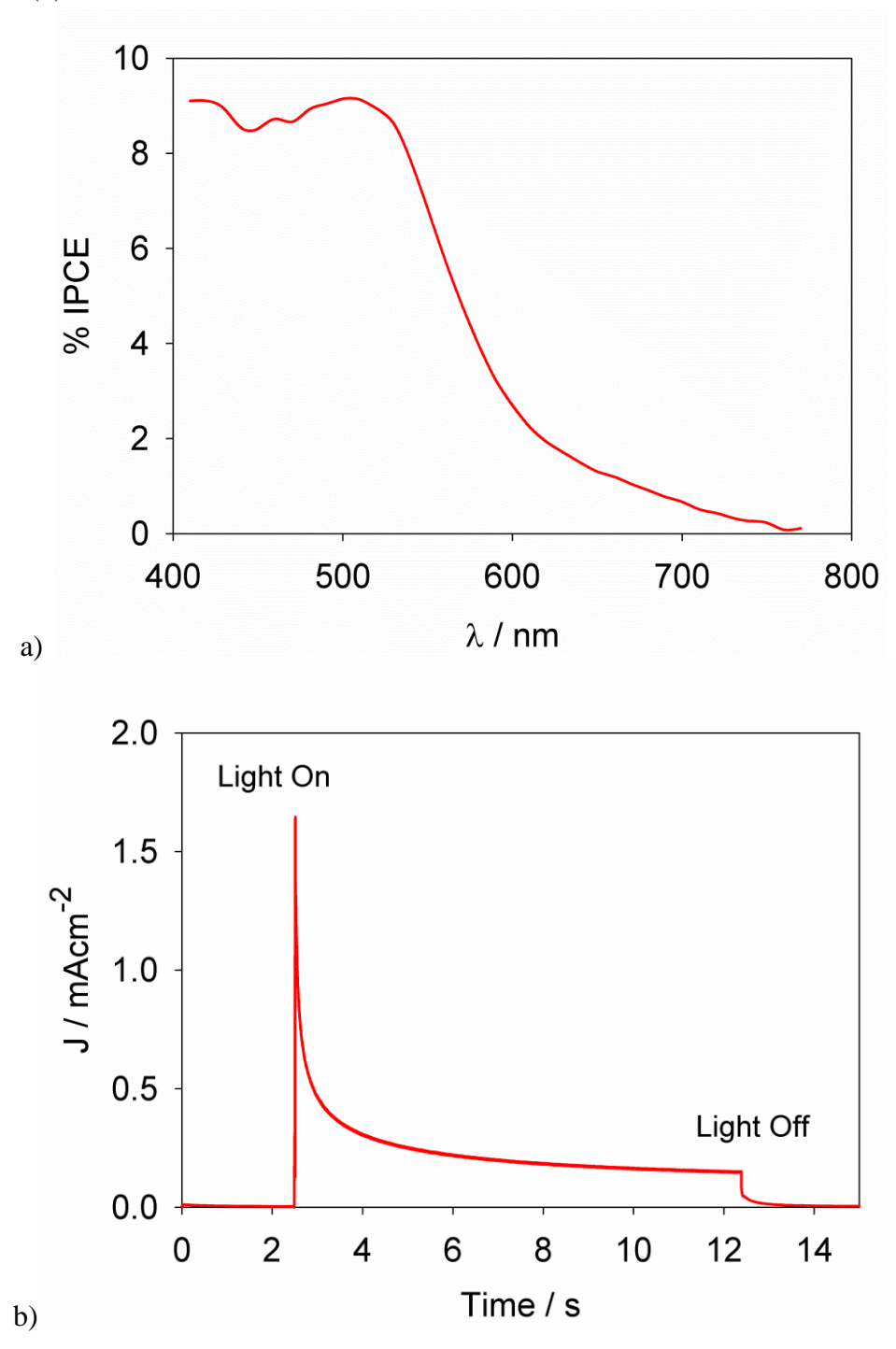


Figure 8.1. a) IPCE and b) current transient of a DSSC utilizing $[Co(bpy)_3]^{3+/2+}$ as part of an ionic liquid system.

The DSSC shown in figure 8.1 suffers terribly from mass transport limitations as shown in figure 8.1b where the initial current decays very quickly when the light is turned on. In this ionic liquid based DSSC the [Co(bpy)₃](TFSI)_{3/2} makes up approximately 35% by mass of the electrolyte. By using a less symmetric redox couple, to prevent crystallization, much higher concentrations should be attainable, even a pure ionic liquid redox shuttle. Once the concentration becomes sufficiently high, charge transport is expected to be mediated by electron hopping rather than mass transport, eliminating the need for fast diffusion. Electron hopping has been demonstrated in "liquid organic semiconductors", however, inorganic single electron outersphere redox shuttles will not suffer from stability problems associated with the formation of organic free radicals in solution.(6, 7) The achievement of an ionic liquid outer-sphere redox shuttle or a liquid organometallic redox shuttle, such as *n*-butylferrocene or *t*-butylferrocene, should allow for charge transport by hopping, alleviating both volatility and mass transport requirements.

8.2 Increasing Voltage in DSSCs with Blocking Dyes and Highly Positive Shuttles

The principle that has allowed outer-sphere redox shuttles to be used in a record breaking DSSC are blocking dyes.(8-12) Blocking dyes contain aliphatic side chains such as nonyl, hexyl, or t-butyl which effectively space the redox shuttle from the semiconductor, slowing recombination. The main limitation with using highly positive redox shuttles is recombination that drastically limits photocurrent and photovoltage in DSSCs, as pointed out in detail in chapter 5. The decrease in recombination that is provided by blocking dyes suggests that the efficiencies predicted in chapter 4 may be obtainable with DSSCs obtaining V_{oc} s well over one volt when paired with an appropriately positive redox shuttle.

The ruthenium redox shuttle used in chapters 2 and 5, $[Ru(bpy)_2(MeIm)_2]^{2+/3+}$, although not a desirable redox shuttle as it strongly absorbs light and is a rare metal, can be used to demonstrate the point of increasing V_{oc} using highly positive redox shuttles. Figure 8.2 displays a J-V curve using $[Ru(bpy)_2(MeIm)_2]^{2+/3+}$ in a DSSC using the dye $Ru(bpy)_2(dcbpy)$, generously donated by the McCusker group. This J-V curve demonstrates that even a very unattractive redox shuttle can produce nearly 1 V V_{oc} even in a cell which produces low photocurrent. Using a blocking dye with an appropriately positive ground state potential, such that it could be regenerated by a redox shuttle such as would increase the $[Ru(bpy)_2(MeIm)_2]^{2+/3+}$ could increase the V_{oc} dramatically, up to an additional 0.5 V, as recombination is prevented.

Additionally, an increased variety of outer-sphere redox shuttles should allow for the successful use of panchromic dyes. Thus far, many panchromic sensitizers have resulted in limited success when employed in DSSCs. Altering the standard high efficiency design of using N719 on TiO₂ with I₃ /I to increase light absorption requires red shifting the absorption of the dye by raising the ground state potential of the dye while maintaining a similar excited state energy. This strategy does not work well with the I_3 /I electrolyte, as discussed in chapter 1, since I_3 /I requires a large driving force for regeneration. Using outer-sphere redox shuttles however allows unlimited variability of E_{redox} , allowing variability of the sensitizer ground state without sacrificing regeneration. The ideal absorption onset predicted in chapter 4 is between 900 and 1000 nm or near 1.3 eV.

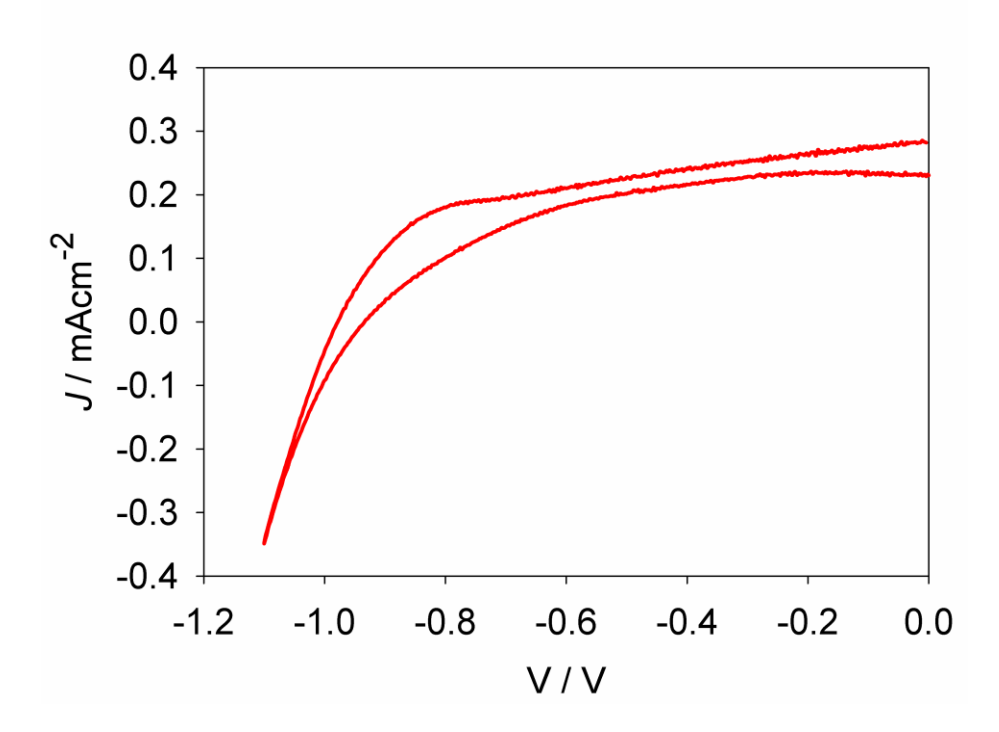


Figure 8.2. *J-V* curve of DSSC using the redox shuttle $[Ru(bpy)_2(MeIm)_2]^{2+/3+}$ in conjunction with the dye $Ru(bpy)_2(dcbpy)$.

To date, only a small number of cobalt complexes, ferrocene derivatives, and copper complexes have been investigated as redox shuttles for use in DSSCs. Outer-sphere redox shuttles contain potential for nearly infinite design through ligand design. The Hamann group is positioned to develop and properly characterize novel interesting outer-sphere redox shuttles containing the required characteristics to satisfy the demands of a high efficiency DSSCs, such as low light absorption, fast regeneration, slow recombination, and rapid diffusion.

8.3 Alternative Semiconducting Materials

The vast majority of DSSC research has focused on using nanoparticle based TiO₂ as photoanodes. This focus was largely based on the initial success with TiO₂ nanoparticles and the resulting ease of their synthesis. There have been no broad investigations that indicate TiO₂ is intrinsically more desirable for DSSC operation than other transparent wide band-gap

semiconductors. Furthermore, the results presented in chapter 5 indicate that the high concentration of surface states found energetically in the band-gap on TiO₂ nanoparticles facilitate electron transfer when electron transfer would otherwise be very slow if restricted to originating from the conduction band. Additional high band-gap semiconducting materials such as SnO₂, Zn₂SnO₄ Nb₂O₅, and ZnO have been utilized in a handful of studies.(*13-17*) These studies ultimately find mediocre efficiencies and an unclear consensus on how to design improved DSSCs using these materials. The direction forward for these materials relies on more fundamental research to clearly define their energetics. One of the main reasons for this is the difficulty in accurately measuring the conduction band edge in porous semiconductors. The variable temperature spectroelectrochemical technique detailed in chapter 6 should allow for the conduction band determination in these and many other important porous semiconducting materials.

Figure 8.3 displays preliminary results of performing spectroelectrochemistry on the transparent wide band-gap semiconductor $SrSnO_3$ electrodes, generously provided by the Poltavets group. Figure 8.3 displays ΔA spectra determined by subtracting the absorbance spectra taken at 0.5 V vs. Ag/AgCl and the indicated potential. This correction removes absorbance contributions from the rest of the cell, including the FTO layer that the $SrSnO_3$ is deposited on.

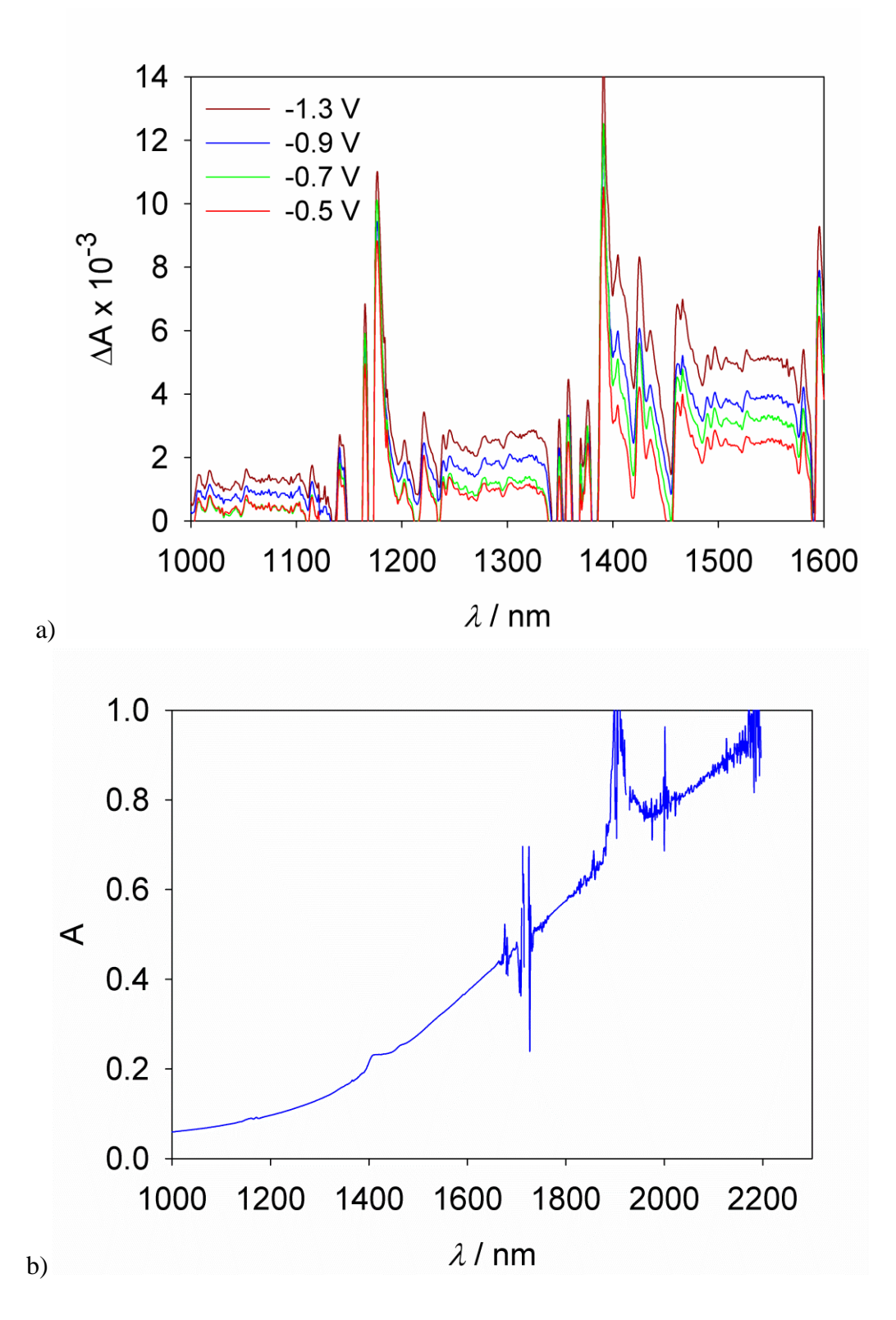


Figure 8.3 a) ΔA of SrSnO₃ between the potential indicated and 0.5 V vs. Ag/AgCl. b) Absorbance of FTO determined by subtracting the absorbance of the electrochemical cell and acetonitrile.

FTO absorbs electrons strongly at wavelengths longer than 1000 nm, shown in figure 8.3b, and consequently must be subtracted when considering spectroelectrochemistry in the near-IR.(18) Conveniently, the absorbance of free electrons in FTO does not significantly change with potential or temperature since the concentration of free electrons is largely determined by the fact that it is degenerately doped and not by applied potential or temperature. The noise in figure 8.3a in the rages of 1150 - 2000 nm and 1350-1450 nm as well as the noise in figure 8.3b near 1700 and 1900 nm results from strong absorbance by acetonitrile. Proper averaging of the absorbance signals should allow for partially reducing this noise. By focusing on the absorbance in the wavelength regions 1000-1100, 1250-1325, and 1500-1575 nm, thus ignoring the noise caused by acetonitrile, there is an increase in absorbance both with increasing wavelength and increasingly negative potential. Both of these trends are intrinsic to absorption of free electrons. Unfortunately, this absorption is relatively weak and acetonitrile prevents monitoring the absorbance much past 1600 nm. Still, these exploratory results suggest spectroelectrochemistry may be able to measure the conduction band edge in SrSnO₃ and other semiconducting materials with observable near-IR absorbance by free electrons; materials which the Hamann group is uniquely poised to investigate.

8.4 Experimental

8.4.1 Ionic Liquid DSSCs

Photoanode was prepared with a 500 cycle ALD blocking layer as described in chapter 2. A transparent TiO₂ nanoparticle film was prepared by doctor blading a paste of nominally 37 nm TiO₂ particles (Solaronix T37/SP) one scotch tape thickness and annealed as described in chapter 2. After the electrode cooled to 100 °C, it was immersed in a solution of 0.3 mM Z907 in

ethanol at 2-3 °C overnight where Z907 is *cis*-Bis(isothiocyanato)(2,2'-bipyridyl-4,4'-dicarboxylato)(4,4'-di-nonyl-2'-bipyridyl)ruthenium(II) (Sigma-Aldrich). A PEDOT counter electrode was prepared as detailed in chapter 7.

The ionic liquid electrolyte was prepared by adding 36.7 mg (34 μ mol) [Co(bpy)₃](TFSI)₂ and 5.5 mg (4.0 μ mol) [Co(bpy)₃](TFSI)₃ to 73.7 mg (0.100 mL) butyltrimethylammonium bis(trifluoromethylsulfonyl)imide (BTMA TFSI, Sigma Aldrich). In order to quickly dissolve the components into the ionic liquid 50 μ L of acetonitrile was added and the solution was sonicated briefly. The electrolyte was then placed in a vacuum desicator for two hours to remove the acetonitrile. The vial of electrolyte was weighed before the addition of acetonitrile and after removal from vacuum to ensure all of the acetonitrile was removed. After the evaporation of the acetonitrile the [Co(bpy)₃]^{3+/2+} did not recrystallize but stayed dissolved in solution. The remaining solution was approximately 340 mM [Co(bpy)₃](TFSI)₂ and 40 mM [Co(bpy)₃](TFSI)₃.

A sandwich cell was created by placing a drop of the ionic liquid electrolyte on the photoanode and clamping a counter electrode with a custom made clamp using a 25 μ m surlyn film as a spacer. Photoelectrochemical measurements were performed with a Gamry Reference 600 potentiostat interfaced with a Xe Arc Lamp.

8.4.2 High Voltage DSSCs

A photoanode was prepared according to chapter 2. The electrolyte was composed of 40 mM Ru(pby)2(MeIm)2](PF6)2, 5 mM NOBF4, 500 mM 4-cyano-2-fluropyridine, and 100 mM LiClO4. Sandwich cells were constructed according to chapter 2. Photoelectrochemical measurements were performed with an Autolab PGSTAT 126N potentiostat interfaced with a Xe Arc Lamp filtered with an AM1.5G filter to simulate sunlight at 100 mWcm⁻².

8.4.3 Spectroelectrochemistry of SrSnO₃

SrSnO $_3$ films were prepared and generously provided by the Poltavets group. These electrodes where assembled into a custom electrochemical cell as described in chapter 6 with an electrolyte composed of 100 mM LiClO $_4$ in acetonitrile. Absorbance data displayed in figure 8.3 were collected on a Perkin Elmer Lambda 1050 with the potential being controlled by a μ AutoLabII potentiostat and referenced to a commercial Ag/AgCl electrode (EDAQ ET072).

REFERENCES

REFERENCES

- 1. M. I. Asghar et al., Energy Environ. Sci. 3, 418 (2010).
- 2. P. Wang, S. M. Zakeeruddin, J. E. Moser, M. Gratzel, *J. Phys. Chem. B* **107**, 13280 (2003).
- 3. N. Papageorgiou et al., J. Electrochem. Soc. **143**, 3099 (1996).
- 4. H. Matsumoto et al., Chem. Lett., 26 (2001).
- 5. S. A. Sapp, C. M. Elliott, C. Contado, S. Caramori, C. A. Bignozzi, *J. Am. Chem. Soc.* **124**, 11215 (Sep, 2002).
- 6. B. A. Kamino, T. P. Bender, R. A. Klenkler, *J. Phys. Chem. Lett.* **3**, 1002 (2012).
- 7. H. J. Snaith, S. M. Zakeeruddin, Q. Wang, P. Pechy, M. Gratzel, *Nano Lett.* **6**, 2000 (2006).
- 8. A. Yella et al., Science **334**, 629 (2011).
- 9. S. M. Feldt *et al.*, *J. Am. Chem. Soc.* **132**, 16714 (Nov, 2010).
- 10. T. Daeneke et al., Nat Chem 3, 211 (2011).
- 11. P. Wang et al., Nature Materials **2**, 402 (Jun, 2003).
- 12. Y. Liu et al., J. Phys. Chem. C 115, 18847 (2011).
- 13. D. A. Gaal, J. T. Hupp, *J. Am. Chem. Soc.* **122**, 10956 (Nov, 2000).
- 14. C. Prasittichai, J. T. Hupp, *J. Phys. Chem. Lett.* **1**, 1611 (2010).
- 15. A. N. M. Green, E. Palomares, S. A. Haque, J. M. Kroon, J. R. Durrant, *Journal of Physical Chemistry B* **109**, 12525 (Jun, 2005).
- 16. F. Lenzmann et al., Journal of Physical Chemistry B 105, 6347 (Jul 12, 2001).
- 17. B. Tan, E. Toman, Y. G. Li, Y. Y. Wu, *J. Am. Chem. Soc.* **129**, 4162 (Apr 11, 2007).
- 18. H. van't Spijker, B. O'Regan, A. Goossens, *J. Phys. Chem. B* **105**, 7220 (2001).